Journal of Nanomaterials

Defect Engineering in Nanomaterials for Photocatalysis and Electrocatalysis

Lead Guest Editor: Yong Hu
Guest Editors: Yu Liu and Changfa Guo

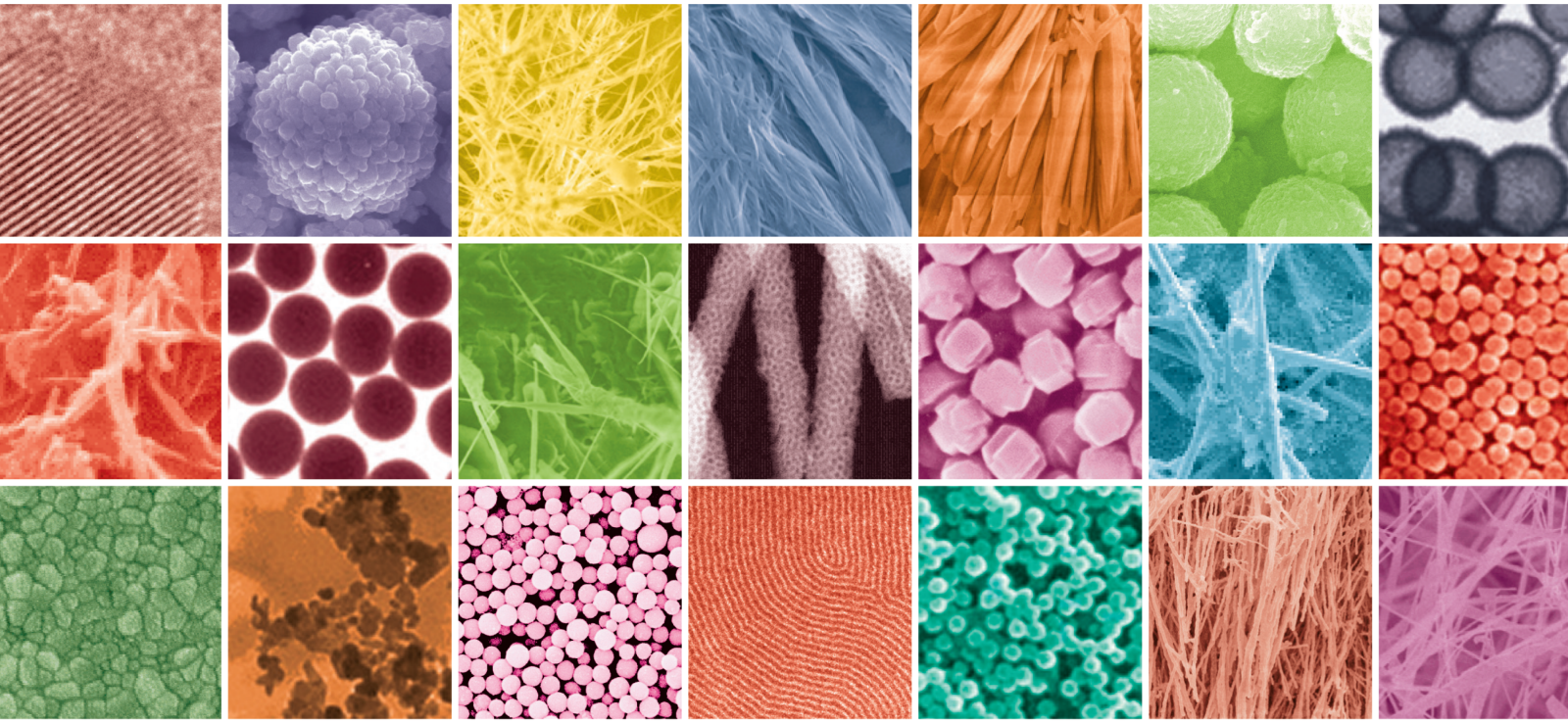

Defect Engineering in Nanomaterials for Photocatalysis and Electrocatalysis

Journal of Nanomaterials

Defect Engineering in Nanomaterials for Photocatalysis and Electrocatalysis

Lead Guest Editor: Yong Hu
Guest Editors: Yu Liu and Changfa Guo

Contents

Hindawi
Journal of Nanomaterials
Volume 2020, Article ID 1768371, 8 pages
https://doi.org/10.1155/2020/1768371

Research Article

Synthesis, Characterization, and Photocatalytic Activity of ZnO Nanomaterials Prepared by a Green, Nonchemical Route

Ngoc Thinh Nguyen [1] **and Van Anh Nguyen** [2]

[1] *School of Chemical Engineering, Hanoi University of Science and Technology, Hanoi 100000, Vietnam*
[2] *Faculty of Natural Sciences and Technology, Hanoi Metropolitan University, Hanoi 100000, Vietnam*

Correspondence should be addressed to Ngoc Thinh Nguyen; thinh.nguyenngoc@hust.edu.vn

Received 18 June 2020; Revised 7 September 2020; Accepted 15 September 2020; Published 1 October 2020

Academic Editor: Changfa Guo

An eco-friendly method for the synthesis of ZnO nanoparticles was studied. Zinc acetate precursor was thermally decomposed without adding any chemical agents. The synthesized materials were thoroughly characterized by various analytical tools. The results indicated that the synthesized ZnO nanomaterials have a wurtzite structure. The estimated crystallite sizes of the materials obtained at 450, 550, 650, and 750°C (named as ZnO-450, ZnO-550, ZnO-650, and ZnO-750) were 33, 36, 38, and 42 nm, respectively. The morphology of the nanomaterials was revealed to be affected by calcination temperature, causing the formation of both nanoparticles and nanorods with different sizes and shapes. The materials were applied as photocatalysts for methylene blue (MB) decomposition under ultraviolet (UV) light. Results showed that the decomposition efficiency strongly depends on UV illumination time, size, and morphology of ZnO nanomaterials. The highest MB decomposition (99.4%) is obtained when using ZnO-750. The photocatalytic decomposition follows the first-order reaction. The reaction rate constants corresponding to the MB decomposition process with the presence of ZnO-450, ZnO-550, ZnO-650, and ZnO-750 are 0.0512, 0.0636, 0.1077, and 0.1286 min^{-1}, respectively.

1. Introduction

Textile industry annually generates a huge amount of organic dyes, resulting in serious impacts on the environment. Therefore, the removal of organic dyes from textile wastewater is considered an essential need. Numerous different technologies have been applied to remove organic dyes in wastewater such as adsorption, coprecipitation, advanced oxidation process (AOP), ozonation, membrane filtration, and biological methods [1, 2]. AOP is noticeable because it could quickly remove various types of dyes. Among AOP techniques, the technique using heterogeneous photocatalytic catalyst is gaining attention as it can remove not only organic dyes but also other organic pollutants [1–5].

It is widely known that ZnO is a semiconductor with broad band gap energy (3.3 eV) and n-type conductivity. In addition, it is very common in nature and environmentally friendly. That is the reason why ZnO is considered a very promising material for different applications such as making solar cells, photocatalysts, electrical equipment, and gas sensors [4]. In the recent years, researchers have focused on synthesizing nano-size ZnO materials for dye removal. ZnO nanomaterials can be synthesized by different methods including the sol-gel method [6], microwave method [7, 8], hydrothermal method [9, 10], precipitation method [11, 12], and thermal decomposition method [13–18]. Among these, thermal decomposition method is considering as an approach to "green method" that does not consume and/or generate toxic chemicals and/or solvents. Moreover, the method allows to prepare a huge amount of sample at one batch [13]. On the attempt to minimize generating toxic wastes, this study synthesized ZnO nanoparticles by thermal decomposition of zinc acetate. The materials were characterized and tested for photocatalytic activity.

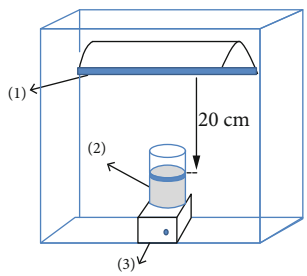

Figure 1: Photoreactor (1): high-pressure mercury lamp; (2): Pyrex glass beaker; (3): magnetic stirring.

2. Materials and Methods

2.1. Synthesis of ZnO Nanomaterials. The analytical grade zinc acetate dihydrate ($Zn(Ac)_2{\cdot}2H_2O$) was purchased from BDH (England) and directly used without further purification. The ZnO nanoparticles were prepared by thermal decomposition method [15, 16], with several modifications. The amount of 3 g zinc acetate dihydrate ($Zn(Ac)_2{\cdot}2H_2O$) was grinded in an agate mortar. The samples were then transferred to closed porcelain crucibles and left in an oven (Nabertherm, Germany) for thermal decomposition at 450°C, 550°C, 650°C, and 750°C within 4 hours with the temperature increasing rate of 10°C/min. The samples were allowed to cool down to room temperature and ground in the agate mortar to obtain final ZnO nanoparticles. Obtained products were named as ZnO-450, ZnO-550, ZnO-650, and ZnO-750 in accordance with the calcination temperatures of the samples.

2.2. Characterization Methods. The X-ray powder diffraction (XRD) patterns of the synthesized nanoparticles were provided using a Bruker D8 advanced X-ray diffractometer equipped with graphite monochromatized Cu Kα radiation ($\lambda = 1.5418$ Å), scanning rate of 0.02 s^{-1} and scanning range of 20–75°. The field emission scanning electron microscopy (FESEM) characterization was performed on Hitachi S-4800 at 15 kV. Transmission electron microscopy (TEM) images were obtained with a JEOL JEM-1010 transmission electron microscope operating at an acceleration voltage of 200 kV. The thermal decomposition of zinc acetate dihydrate was studied by thermal gravimetric analysis (TGA) (DSC131, LABSYS TG/DSC1600, TMA, and Setaram, France) to determine its thermal stability and decomposition temperature. The thermogravimetry (TG) curve of zinc acetate dihydrate was recorded in an air flow at the heating rate of 10°C/min from room temperature to 900°C. The nitrogen adsorption-desorption isotherms of the ZnO nanomaterials were recorded by the TriStar II 3020 nitrogen adsorption apparatus (Micromeritics Instruments, USA) at 77 K. The BET specific surface areas (S_{BET}) of the samples were determined by the Barrett–Joyner–Halenda (BJH) method.

2.3. Photocatalytic Study. The potential application of ZnO nanoparticles towards dye removal from wastewaters was evaluated in heterogeneous photocatalysis route. Methylene blue (MB) was used to test the photocatalytic efficiency of the ZnO nanoparticles. Photocatalytic reaction was carried out in a homemade photoreactor equipped with an Osram 250W, high-pressure mercury lamp as a source for UV radiation (Figure 1). The reactor consists of a Pyrex glass beaker and a magnetic stirring. The lamp is positioned above the beaker. The distance between the lamp and the Pyrex glass beaker is 20 cm. The whole photocatalytic reactor is insulated in a box to prevent harmful radiation. For every batch experiment, 0.1 g of ZnO nanoparticles was dispersed in 100 mL aqueous solution of MB 10 mg/L. Prior to UV light illumination, the suspension was magnetically stirred in the dark for 30 min in order to obtain proper homogeneity of the mixture as well as to reach the absorption equilibrium. At definite time intervals, 4 mL of the mixture was collected and followed by centrifugation (Hettich Mikro 22R Centrifuges), at 5000 rpm for 10 min to remove the ZnO nanoparticles

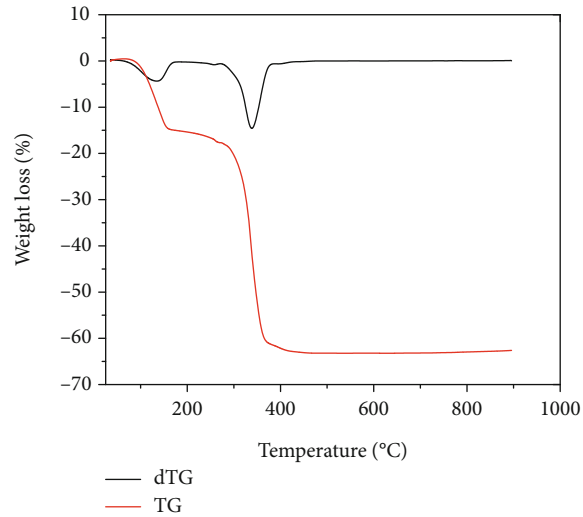

Figure 2: TG-DTG curve of thermal decomposition of zinc acetate dihydrate at heating rate of 10°C in air.

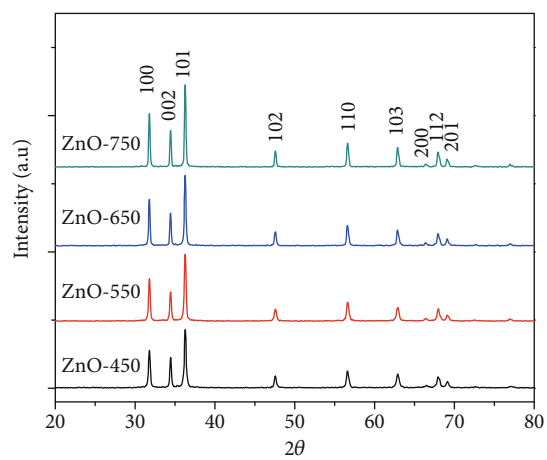

Figure 3: XRD patterns of the nanocrystalline ZnO samples thermally decomposed at 450, 550, 650, and 750°C for 4 h.

Table 1: Comparison between XRD results of ZnO nanoparticles and standard pattern for ZnO powder.

JCPDS (36-1451)			ZnO-450			ZnO-550			ZnO-650			ZnO-750		
hkl	2θ	%I	2θ	%I	FWHM	2θ	%I	FWHM	2θ	%I	FWHM	2θ	%I	FWHM
100	31.76	57	31.79	64	0.236	31.79	63	0.236	31.79	66	0.207	31.79	64	0.207
002	34.42	44	34.46	51	0.207	34.47	43	0.207	34.43	46	0.236	34.43	44	0.207
101	36.25	100	36.28	100	0.266	36.27	100	0.246	36.26	100	0.230	36.26	100	0.207
102	47.53	23	47.56	20	0.266	47.54	17	0.325	47.59	20	0.236	47.59	19	0.236
110	56.60	32	56.58	28	0.236	56.62	28	0.325	56.55	27	0.207	56.55	27	0.295
103	62.86	29	62.87	22	0.354	62.78	16	0.236	62.83	21	0.266	62.83	20	0.207
112	67.96	22	67.94	17	0.413	67.99	18	0.207	67.93	17	0.413	67.91	17	0.354
201	69.09	16	69.14	10	0.360	69.10	9	0.413	69.08	9	0.236	69.05	9	0.207

Table 2: Estimated structure parameters and average crystallite size of ZnO nanoparticles from the XRD data.

Samples	*a* (Å)	*c* (Å)	*c*/*a*	Volume of unit cell (Å^3)	Size of the crystallites (nm)
JCPDS 36-1451	3.249	5.205	1.602	47.58	x
ZnO-450	3.246	5.199	1.602	47.44	33
ZnO-550	3.246	5.198	1.601	47.43	36
ZnO-650	3.246	5.203	1.603	47.48	38
ZnO-750	3.246	5.203	1.603	47.48	42

suspensions from the solution. Samples were finally analyzed by Agilent 8453 UV-vis spectrophotometer at the λ_{max} of 664 nm wavelength. The percentage of photocatalytic degradation was calculated using the following equation:

$$\text{Percentage photodegardation} = \frac{A_0 - A}{A_0} \times 100. \quad (1)$$

The rate constant of the degradation, k, was obtained from the first-order plot according to the equation: $\ln(A_0/A) = kt$, where A_0 is the initial absorbance of dye and A is the absorbance of dye solution after UV light irradiation [19].

3. Results and Discussion

3.1. Characterization of ZnO Nanoparticles. The TG and dTG (differential thermogravimetric) curves are provided in Figure 2. The two-stage weight loss was observed. The first stage with approximately 15.72% of weight loss was presumed to be the thermal dehydration of zinc acetate dihydrate to form anhydrous zinc acetate. The second stage (47.58% of weight loss) within the temperature region from 250 to 350°C is accounted for the decomposition of anhydrous zinc acetate to form ZnO [15]. The weight loss was no longer observed within the temperature ranges from 350 to 900°C. This signaled the complete decomposition of the precursor at 350°C. Therefore, the calcination temperatures of 450°C, 550°C, 650°C, and 750°C were selected.

The XRD patterns of the prepared products are shown in Figure 3. The major XRD peaks locate at angles (2θ) of 31.8°, 34.4°, 36.2°, 47.5°, 56.6°, 62.8°, 66.3°, 68.1°, and 69.3° corresponding to the (100), (002), (101), (102), (110), (103), (200), (112), and (201) planes of ZnO, respectively. The standard diffraction peaks show the hexagonal wurtzite structure of ZnO with P63mc space group [10, 20]. None of the peaks for impurities was observed. Furthermore, strong intensity and narrow width of ZnO diffraction peaks suggest that the dominant phase of the product is hexagonal wurtzite structure [5, 10–12]. The X'Pert High Score was used to further interpret the XRD patterns. The characteristic peaks of the synthesized nanoparticles are completely identical to those from the JCPDS data (Card No. 36-1451) (Table 1) [20]. The crystallite size of the nanoparticles was calculated from the peak broadening of diffraction peaks using the Debye–Scherer formula $D = k\lambda/\beta\cos\theta$, where D is crystallite size, k is constant (0.89), $\lambda = 0.154$ nm represents the wavelength of X-ray radiation, β is the full width at half maximum of diffraction peaks (FWHM) in radian, and θ is Bragg's angle [12]. The size of the crystallites of ZnO nanoparticles was evaluated by measuring the FWHM of the most intense peak (101). Approximately, the average crystallite size of ZnO-450 is 33 nm while those of ZnO-550, ZnO-650, and ZnO-750 are 36, 38, and 42 nm, respectively. The elevated surface energies at higher calcination temperatures may be responsible for the increasing of the crystallite size. Similar phenomenon was also reported in former studies [16].

The lattice cell parameters (ɑ and c) of hexagonal wurtzite structure were calculated as follows [12]:

$$c = \frac{\lambda}{\sin\theta_{(002)}},$$
$$a = \frac{\lambda}{\sqrt{3}\,\sin\theta_{(100)}}, \quad (2)$$
$$\frac{1}{d_{hkl}^2} = \frac{4}{3}\left[\frac{h^2 + hk + k^2}{a^2}\right] + \frac{l^2}{c^2},$$

where d is the interplanar distance; h, k, and l are the Miller indices of the plane; $\lambda = 1.54$ Å is the wavelength of the X-rays; and θ_{100} and θ_{002} are angles of the diffraction in degree corresponding to the planes 100 and 002. The volume (V) of

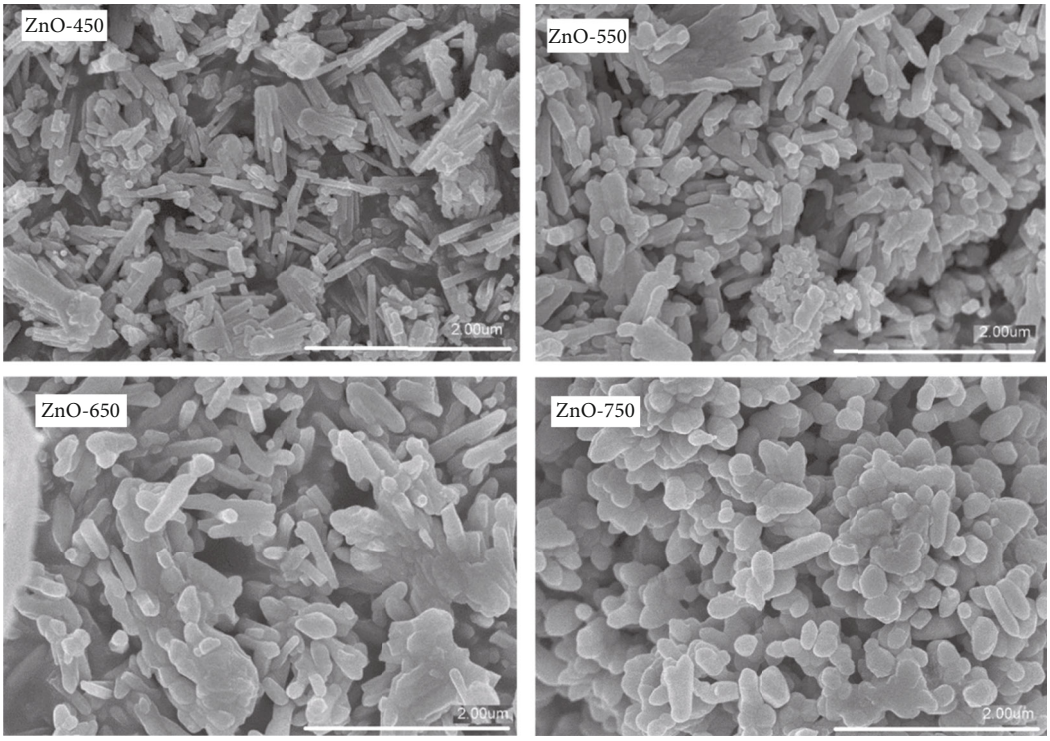

Figure 4: FESEM images of the ZnO nanoparticles thermally decomposed at 450, 550, 650, and 750°C.

the unit cells of hexagonal wurtzite structure was calculated in the following equation:

$$V = 0.866 \times a^2 \times c. \quad (3)$$

Results are listed in Table 2. It was evident that the lattice parameter values of as-synthesized ZnO nanoparticles are similar to the standard values of ZnO.

The surface morphology and size of ZnO nanoparticles were imaged using the FESEM analysis (Figure 4). Both sphere-like (diameters of 40-100 nm) and rod-like (diameters of 50-200 nm and lengths of 200-500 nm) ZnO nanoparticles were observed. Calcination temperatures seem to dramatically affect the morphology of the nanoparticles. At the temperature of 450°C, the rod-like particles are predominant. Nevertheless, more sphere-like particles are formed as increasing the temperatures. This is also confirmed by the transmission electron microscopic (TEM) analysis (Figure 5).

BET surface areas of ZnO-450, ZnO-550, ZnO-650, and ZnO-750 are 6.8, 4.8, 3.3, and 2.4 (m^2/g), respectively (Table 3). The surface area of ZnO nanoparticles decreases when increasing the calcination temperature.

3.2. Photocatalytic Properties. Figure 6 shows the absorption spectra of the degradation of MB under UV light with the presence of ZnO nanoparticles. Decrease in absorbance intensity at 664 nm clearly confirms that ZnO nanoparticles are acting as photocatalyst for the degradation of dye.

The ZnO nanoparticles synthesized at higher temperatures tend to yield higher removal efficiencies. Figure 7 shows that the best degradation efficiency can be achieved with the ZnO-650 and ZnO-750 (approximately 100% within 40 min). It is widely known that morphology, surface area, and crystallinity of a material are mainly responsible for its photocatalytic activity [21, 22]. When enhancing the surface area and crystallinity of the material, the photocatalytic activity will be improved. Nevertheless, while the crystallinity of the material increases, the surface area of the material decreases as raising calcination temperature (Figure 3 and Table 3). Therefore, morphology could act as a potential factor strongly influencing the final degradation efficiency. According to the results sphere-shaped ZnO nanoparticles (ZnO-650 and ZnO-750) show higher removal efficiency compared with the spindle-and rod-shaped ZnO nanoparticles (ZnO-450 and ZnO-550). Similar results were observed in Saravanan et al. [23].

The kinetic study for the degradation of MB was studied using the Langmuir–Hinshelwood kinetic model: $\ln(A_0/A) = kt$, where A_0 is initial absorbance of dye, A is absorbance of dye solution after UV light irradiation, and k is a pseudo-first-order rate constant [19]. A plot of $\ln(A_0/A)$ versus t is shown in Figure 8. Photocatalytic activity occurs because of the interaction of photocatalyst and UV irradiation that yields highly reactive hydroxyl radicals, which are believed to be the main species responsible for the oxidation. Other active species such as holes, free electrons, and superoxide could also act as oxidant species for the degradation of MB. The reaction process was proposed elsewhere in Qi et al. and numerous former studies [4, 19, 24, 25]. The Langmuir–Hinshelwood rate expression has been successfully used for heterogeneous photocatalytic degradation to determine the relationship between the initial degradation rate and the initial concentration of the organic substrate [1, 9].

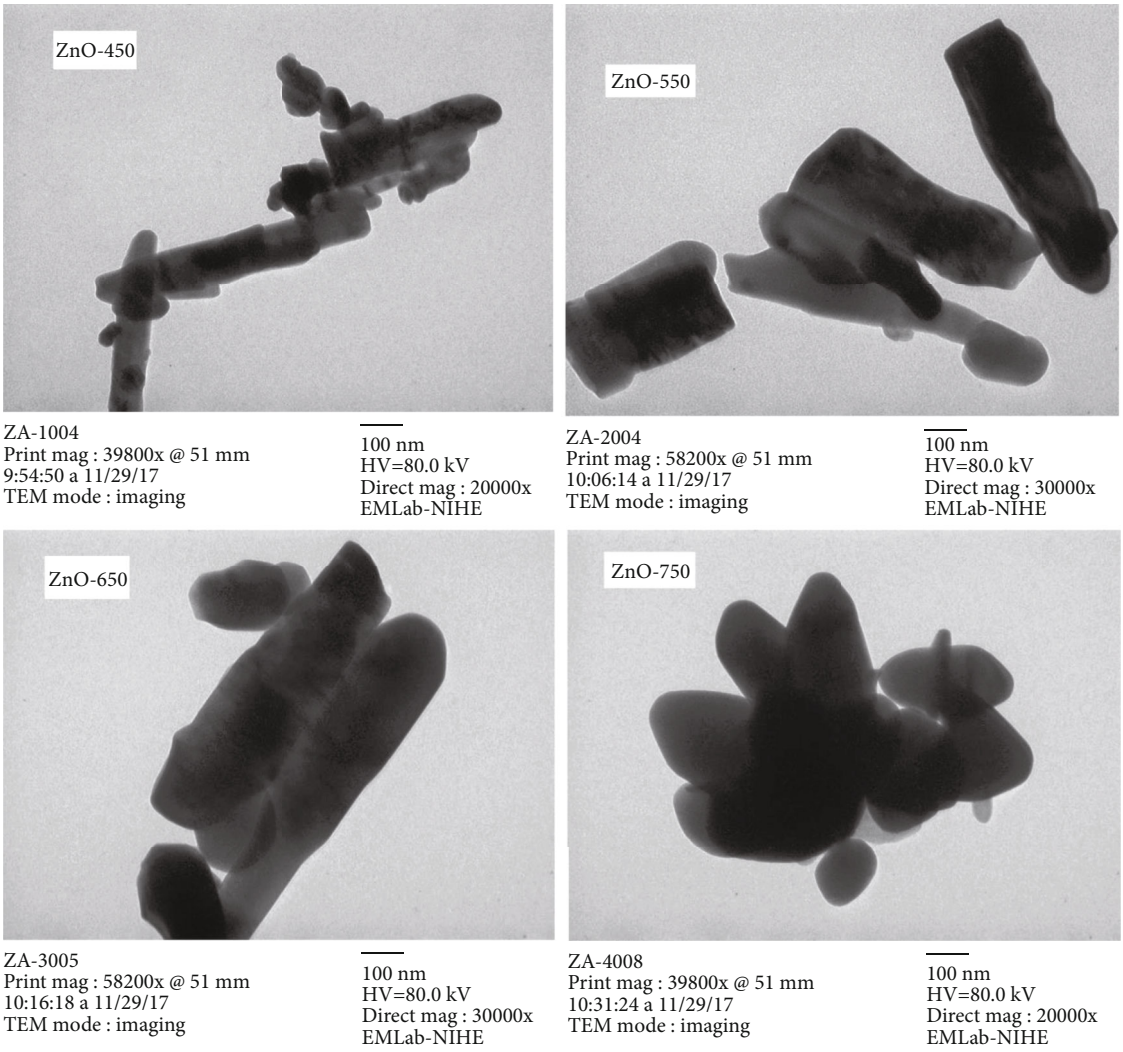

Figure 5: TEM images of the ZnO nanoparticles thermally decomposed at 450, 550, 650, and 750°C.

Table 3: BET surface areas of ZnO nanoparticles thermally decomposed at 450, 550, 650, and 750°C.

Sample	S_{BET} (m^2/g)[a]
ZnO-450	6.8
ZnO-550	4.8
ZnO-650	3.3
ZnO-750	2.4

[a]BET surface area calculated from the linear part of the BET plot.

The linear plots and relatively high R^2 values (Table 4) prove that the degradation of MB obeys the first-order reaction kinetics.

The removal efficiency of the synthesized ZnO nanoparticles was comparable with other materials in former studies (Table 5). It can be concluded that the obtained materials have high potential to be applied for organic dye removal.

Stability and reusability of ZnO-750 were tested. Results show that the removal efficiency negligible decreases from 99.4% to 94.1% at the third cycle (Figure 9). This suggests the good reuse performance of the material [29, 30].

4. Conclusions

ZnO nanomaterials were successfully generated by a green method, thermal decomposition of zinc acetate precursor at 450, 550, 650, and 750°C. Results reveals a wurtzite hexagonal structure of ZnO-450, ZnO-550, ZnO-650, and ZnO-750 with the crystal sizes of 33, 36, 38, and 42 nm, respectively. The material morphology changes from the rod-like shapes to the sphere-like shapes when increasing decomposition temperature.

ZnO nanomaterials were applied as photocatalyst to decompose MB under UV light. The ability to decompose MB depends on the UV illumination time, the size, and morphology of ZnO nanomaterials. The highest MB decomposition is obtained with the ZnO-750. More than 99% of the dye was removed after 40 minutes. Photocatalytic decomposition process of methylene blue follows the first-order reaction. The reaction rate constants corresponding to the removal

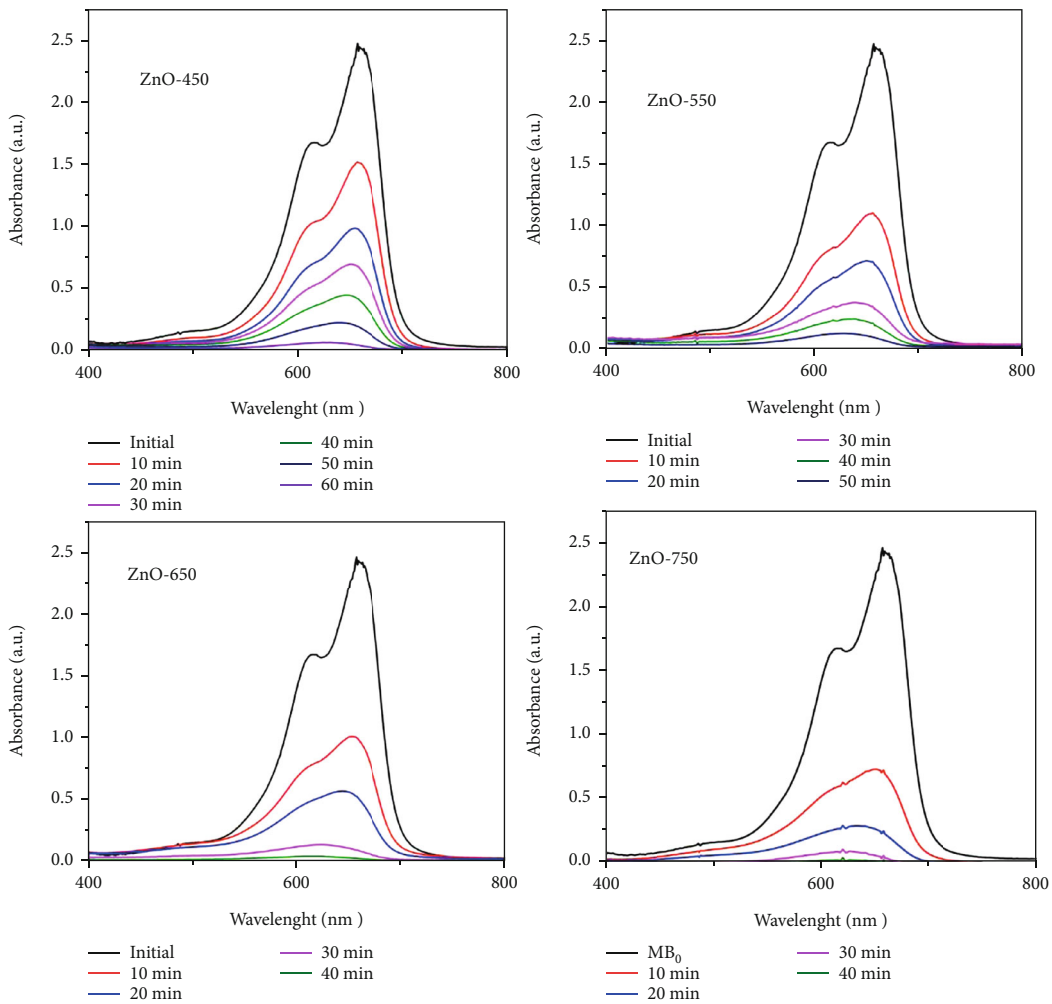

Figure 6: UV-vis absorbance spectra of MB solution exposure to UV light in the presence of the ZnO nanoparticles thermally decomposed at 450, 550, 650, and 750°C.

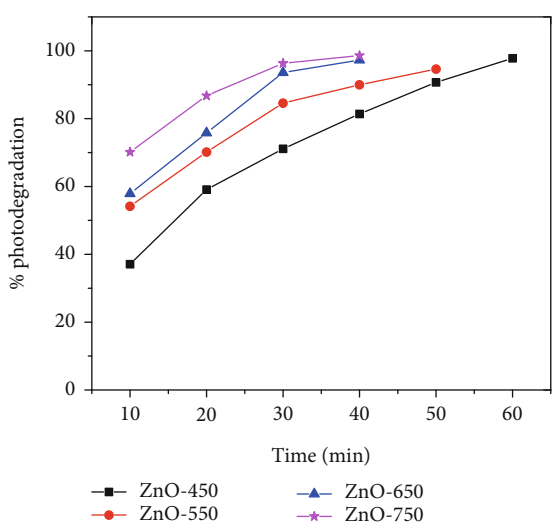

Figure 7: Percentage degradation of methylene blue dye vs. irradiation time in the presence of the ZnO nanoparticles thermally decomposed at 450, 550, 650, and 750°C.

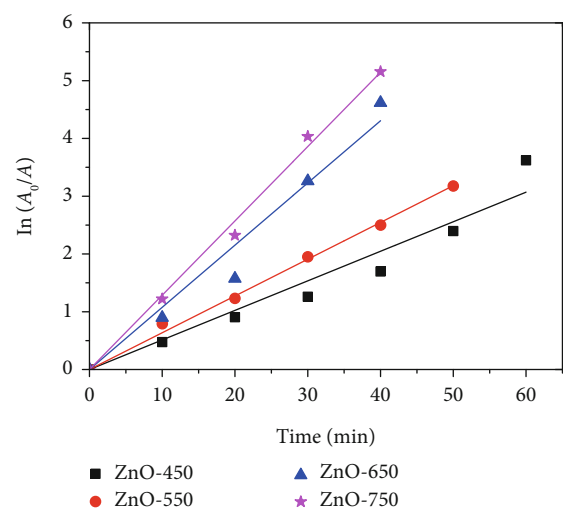

Figure 8: Kinetic plot of ln (A_0/A) vs. irradiation time of the ZnO nanoparticles thermally decomposed at 450, 550, 650, and 750°C.

Table 4: Rate constant for photo degradation of methylene blue dye.

Samples	Rare (min^{-1})	Adj. R^2
ZnO-450	0.0512	0.9740
ZnO-550	0.0636	0.9984
ZnO-650	0.1077	0.9835
ZnO-750	0.1286	0.9990

Table 5: Photocatalytic degradation of methylene blue with different ZnO nanomaterials under UV light catalyst methods.

Catalyst	Methods	%removal	Degradation rate (min^{-1})	Ref
Nanosized ZnO	Sol-gel	99	—	[23]
	Precipitation	98	—	[23]
	Thermal decomposition	85	—	[23]
ZnO nanoparticles	Precipitation	92.5	0.0124	[26]
ZnO nanospheres	Polyol-method	99.1	0.07432	[27]
Nitrogen doped ZnO nanoparticles	Hydrothermal method	99.6	-0.0579	[28]
ZnO nanoparticles	Thermal decomposition	99.4	0.1286	This study

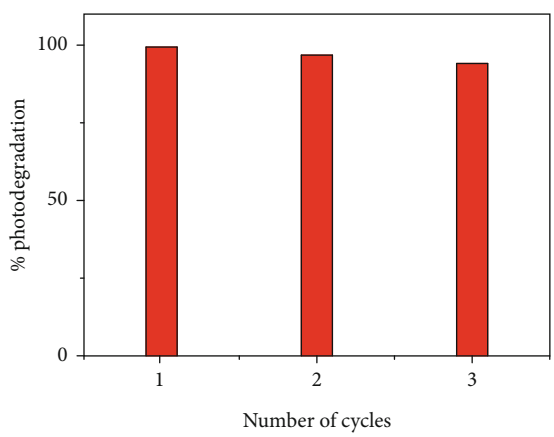

Figure 9: ZnO nanoparticle (ZnO-750) catalyst reusability degradation efficiency vs. cycle numbers under UV light irradiation 0 to 40 minutes.

process of ZnO-450, ZnO-550, ZnO-650, and ZnO-750 are 0.0512, 0.0636, 0.1077, and 0.1286 min^{-1}, respectively.

Data Availability

The data used to support the findings are available from the corresponding author upon request.

Conflicts of Interest

The authors declare that they have no conflicts of interest.

Acknowledgments

This study was supported by the Ministry of Science and Technology in South Korea through the International Environmental Research Institute (IERI) of Gwangju Institute of Science and Technology (GIST) in 2019.

References

[1] L. Bilińska, M. Gmurek, and S. Ledakowicz, "Textile wastewater treatment by AOPs for brine reuse," *Process Safety and Environmental Protection*, vol. 109, pp. 420–428, 2017.

[2] R. M. Christie, *Environmental Aspects of Textile Dyeing*, Woodhead Publishing Limited, 2007.

[3] S. K. Sharma, *Green Chemistry for Dyes Removal from Wastewater: Research Trends and Applications*, Scrivener Publishing, John Wiley & Sons, 2015.

[4] K. Qi, B. Cheng, J. Yu, and W. Ho, "Review on the improvement of the photocatalytic and antibacterial activities of ZnO," *Journal of Alloys and Compounds*, vol. 727, pp. 792–820, 2017.

[5] H. Liu, L. Li, C. Guo, J. Ning, Y. Zhong, and Y. Hu, "Thickness-dependent carrier separation in Bi2Fe4O9 nanoplates with enhanced photocatalytic water oxidation," *Chemical Engineering Journal*, vol. 385, article 123929, 2020.

[6] R. Peña-Garcia, Y. Guerra, B. V. M. Farias, D. M. Buitrago, A. Franco Jr., and E. Padrón-Hernández, "Effects of temperature and atomic disorder on the magnetic phase transitions in ZnO nanoparticles obtained by sol–gel method," *Materials Letters*, vol. 233, pp. 146–148, 2018.

[7] D. Sharma, S. Sharma, B. S. Kaith, J. Rajput, and M. Kaur, "Synthesis of ZnO nanoparticles using surfactant free in-air and microwave method," *Applied Surface Science*, vol. 257, no. 22, pp. 9661–9672, 2011.

[8] R. O. Yathisha, Y. A. Nayaka, and C. C. Vidyasagar, "Microwave combustion synthesis of hexagonal prism shaped ZnO nanoparticles and effect of Cr on structural, optical and electrical properties of ZnO nanoparticles," *Materials Chemistry and Physics*, vol. 181, pp. 167–175, 2016.

[9] M. Y. Nassar, M. M. Moustafa, and M. M. Taha, "Hydrothermal tuning of the morphology and particle size of hydrozincite nanoparticles using different counterions to produce nanosized ZnO as an efficient adsorbent for textile dye removal," *RSC Advances*, vol. 6, no. 48, pp. 42180–42195, 2016.

[10] N. Kumaresan, K. Ramamurthi, R. Ramesh Babu, K. Sethuraman, and S. Moorthy Babu, "Hydrothermally grown ZnO nanoparticles for effective photocatalytic activity," *Applied Surface Science*, vol. 418, pp. 138–146, 2017.

[11] A. P. A. Oliveira, J.-F. Hochepied, F. Grillon, and M.-H. Berger, "Controlled precipitation of zinc oxide particles at room temperature," *Chemistry of Materials*, vol. 15, no. 16, pp. 3202–3207, 2003.

[12] M. Kahouli, A. Barhoumi, A. Bouzid, A. al-Hajry, and S. Guermazi, "Structural and optical properties of ZnO nanoparticles prepared by direct precipitation method," *Superlattices and Microstructures*, vol. 85, pp. 7–23, 2015.

[13] Udayabhanu, G. Nagaraju, H. Nagabhushana et al., "Green, nonchemical route for the synthesis of ZnO superstructures, evaluation of its applications toward photocatalysis, photoluminescence, and biosensing," *Crystal Growth & Design*, vol. 16, no. 12, pp. 6828–6840, 2016.

[14] S. Baskoutas, P. Giabouranis, S. N. Yannopoulos et al., "Preparation of ZnO nanoparticles by thermal decomposition of zinc alginate," *Thin Solid Films*, vol. 515, no. 24, pp. 8461–8464, 2007.

[15] C.-C. Lin and Y.-Y. Li, "Synthesis of ZnO nanowires by thermal decomposition of zinc acetate dihydrate," *Materials Chemistry and Physics*, vol. 113, no. 1, pp. 334–337, 2009.

[16] S. Labuayai, V. Promarak, and S. Maensiri, "Synthesis and optical properties of nanocrystalline ZnO powders prepared by a direct thermal decomposition route," *Applied Physics A*, vol. 94, no. 4, pp. 755–761, 2009.

[17] R. Shankar, R. K. Srivastava, and S. G. Prakash, "ZnO NPs synthesized by thermal decomposition of zinc oxalate at 300°C and its photo response under UV-illumination," in *AIP Conference Proceedings*, p. 239, Bikaner, Rajasthan, India, 2013.

[18] M. I. Khalil, M. M. Al-Qunaibit, A. M. Al-zahem, and J. P. Labis, "Synthesis and characterization of ZnO nanoparticles by thermal decomposition of a curcumin zinc complex," *Arabian Journal of Chemistry*, vol. 7, no. 6, pp. 1178–1184, 2014.

[19] N. N. Kumaran and K. Muraleedharan, "Photocatalytic activity of ZnO and Sr^{2+} doped ZnO nanoparticles," *Journal of Water Process Engineering*, vol. 17, pp. 264–270, 2017.

[20] Joint Committee for Powder Diffraction Society (JCPDS), "Powder Diffraction Database," *Pattern*, 36–1451.

[21] W. Zhou, F. Sun, K. Pan et al., "Well-ordered large-pore mesoporous anatase TiO_2 with remarkably high thermal stability and improved crystallinity: preparation, characterization, and photocatalytic performance," *Advanced Functional Materials*, vol. 21, no. 10, pp. 1922–1930, 2011.

[22] G. Tian, H. Fu, L. Jing, B. Xin, and K. Pan, "Preparation and characterization of stable Biphase TiO2Photocatalyst with high crystallinity, large surface area, and enhanced photoactivity," *Journal of Physical Chemistry C*, vol. 112, no. 8, pp. 3083–3089, 2008.

[23] R. Saravanan, V. K. Gupta, V. Narayanan, and A. Stephen, "Comparative study on photocatalytic activity of ZnO prepared by different methods," *Journal of Molecular Liquids*, vol. 181, pp. 133–141, 2013.

[24] W. Yang, L. Zhang, Y. Hu, Y. Zhong, H. B. Wu, and X. W. D. Lou, "Microwave-assisted synthesis of porous Ag_2S-Ag hybrid nanotubes with high visible-light photocatalytic activity," *Angewandte Chemie International Edition*, vol. 51, no. 46, pp. 11501–11504, 2012.

[25] Y. Wang, W. Yang, L. Zhang, Y. Hu, and X. W. (David) Lou, "Formation of MS-Ag and MS (M = Pb, Cd, Zn) nanotubes via microwave-assisted cation exchange and their enhanced photocatalytic activities," *Nanoscale*, vol. 5, no. 22, pp. 10864–10867, 2013.

[26] A. Balcha, O. P. Yadav, and T. Dey, "Photocatalytic degradation of methylene blue dye by zinc oxide nanoparticles obtained from precipitation and sol-gel methods," *Environmental Science and Pollution Research*, vol. 23, no. 24, pp. 25485–25493, 2016.

[27] C. Yang, Q. Li, L. Tang, A. Bai, H. Song, and Y. Yu, "Monodispersed colloidal zinc oxide nanospheres with various size scales: synthesis, formation mechanism and enhanced photocatalytic activity," *Journal of Materials Science*, vol. 51, no. 11, pp. 5445–5459, 2016.

[28] E. Prabakaran and K. Pillay, "Synthesis of N-doped ZnO nanoparticles with cabbage morphology as a catalyst for the efficient photocatalytic degradation of methylene blue under UV and visible light," *RSC Advances*, vol. 9, no. 13, pp. 7509–7535, 2019.

[29] L. Li, C. Guo, J. Shen, J. Ning, Y. Zhong, and Y. Hu, "Construction of sugar-gourd-shaped CdS/Co1-xS hollow heteronanostructure as an efficient Z-scheme photocatalyst for hydrogen generation," *Chemical Engineering Journal*, vol. 400, article 125925, 2020.

[30] H. Zhang, C. Guo, J. Ren et al., "Beyond CoO_x: a versatile amorphous cobalt species as an efficient cocatalyst for visible-light-driven photocatalytic water oxidation," *Chemical Communications*, vol. 55, no. 93, pp. 14050–14053, 2019.

Hindawi
Journal of Nanomaterials
Volume 2020, Article ID 8461543, 9 pages
https://doi.org/10.1155/2020/8461543

Research Article

Improvement of Photocatalytic Performance for the g-C_3N_4/MoS_2 Composite Used for Hypophosphite Oxidation

Wei Guan,[1,2] Kuang He,[1,2] Jianwei Du,[1,2] Yong Wen,[1,2] Mingshan Li,[1,2] Li Zhuo,[3] Rui Yang,[3] and Kaiming Li[1,2]

[1]*South China Institute of Environmental Sciences, Ministry of Ecological Environment, Guangzhou, China*
[2]*The Key Laboratory of Water and Air Pollution Control of Guangdong Province, South China Institute of Environmental Sciences, MEP, Guangzhou, China*
[3]*Chongqing Solid Waste Management Center, Chongqing, China*

Correspondence should be addressed to Jianwei Du; dujianwei@scies.org

Received 24 July 2020; Revised 21 August 2020; Accepted 26 August 2020; Published 15 September 2020

Academic Editor: Changfa Guo

The synthesized g-C_3N_4/MoS_2 composite was a high-efficiency photocatalytic for hypophosphite oxidation. In this work, a stable and cheap g-C_3N_4 worked as the chelating agent and combined with the MoS_2 materials. The structures of the fabricated g-C_3N_4/MoS_2 photocatalyst were characterized by some methods including X-ray diffraction (XRD), scanning electron microscopy (SEM), and X-ray photoelectron spectra (XPS). Moreover, the photocatalytic performances of various photocatalysts were measured by analyzing the oxidation efficiency of hypophosphite under visible light irradiation and the oxidation efficiency of hypophosphite using the g-C_3N_4/MoS_2 photocatalyst which was 93.45%. According to the results, the g-C_3N_4/MoS_2 composite showed a promising photocatalytic performance for hypophosphite oxidation. The improved photocatalytic performance for hypophosphite oxidation was due to the effective charge separation analyzed by the photoluminescence (PL) emission spectra. The transient photocurrent response measurement indicated that the g-C_3N_4/MoS_2 composites (2.5 μA cm^{-2}) were 10 times improved photocurrent intensity and 2 times improved photocurrent intensity comparing with the pure g-C_3N_4 (0.25 μA cm^{-2}) and MoS_2 (1.25 μA cm^{-2}), respectively. The photocatalytic mechanism of hypophosphite oxidation was analyzed by adding some scavengers, and the recycle experiments indicated that the g-C_3N_4/MoS_2 composite had a good stability.

1. Introduction

Sodium hypophosphite is the most common reducing agent during the electroless plating, generating high concentration of hypophosphite wastewater [1, 2]. The main components of plating wastewater are hypophosphite and phosphite, which should be further treatment before discharging into the river or lake avoiding the problem of eutrophication. Due to the high solubility of hypophosphite and phosphite, it is difficult to remove the contaminants by adding Ca^{2+} and Fe^{3+} ions to generate sediment following by precipitation [3, 4]. Therefore, hypophosphite and phosphite should be oxidized to phosphate, which is easy to recover with the precipitation method. At the same time, the structure of hypophosphite and phosphite is relatively stable, and it is difficult to oxidize them by ordinary oxidation technology [5], so the technology with strong oxidation ability is needed to solve the problem of hypophosphite oxidation.

Semiconductor photocatalytic technology is a new kind of environmental pollutant reduction technology [6]. The photocatalytic oxidation treatment has the characteristics of easy to handle, no secondary pollution, and a broad potential application [7]. In particular, TiO_2, as a photocatalytic material, can effectively catalyze the degradation of pollutants in water. It has the advantages of chemical stability, high catalytic activity, good harmlessness to human body, low reaction conditions, and mild selectivity, which has been widely used in the treatment of pollutants that are difficult to be degraded [8]. However, a large band gap (3.2 eV) of TiO_2 indicates that it can only absorb ultraviolet light (only about 3–5% of total

sunlight), which largely inhabits its wide application [9, 10]. So, it is necessary to synthesize a novel photocatalyst that can be responded under visible light irradiation.

Recently, a two-dimensional (2D) conjugated polymer, metal-free graphitic carbon nitride (g-C_3N_4) has caused much attention due to its suitable band gap of 2.7 eV, which can be responded under visible light irradiation [11, 12]. In addition, the excellent structural stability of g-C_3N_4 is widely used in photocatalytic conversion of solar energy and purification of environmental pollutants [13]. Nevertheless, there are some shortcomings for g-C_3N_4 as a photocatalyst, such as low utilization rate of light and high recombination rate of photon-generated carrier [14, 15]. Some methods such as structure modification [16], semiconductors coupling [17], elements, and molecular doping [18, 19] were used to modify the g-C_3N_4 materials to improve the photocatalytic performance of g-C_3N_4.

Molybdenum disulfide (MoS_2), a 2D metal sulfide material, has the properties of excellent stability and low band gap of 1.2-1.9 eV, which can be easily responded under visible light irradiation and worked as photocatalyst [20, 21]. The valence band electrons can detour into the conduction band under visible light irradiation and leave holes, thus it will generate electron-hole pairs [22]. Due to the small band gap of MoS_2, it can be used as a catalyst and cocatalyst, especially doped on some materials, and its photocatalytic performance has been greatly improved [23], which has been widely used in photocatalytic hydrogen evolution and the degradation of organic pollutants [24–26]. The photogenerated electrons of semiconductors could transfer through these noble metals rapidly, and the lifetime of these electrons and holes was prolonged for the noble metal-semiconductor heterostructure materials. Therefore, the prepared g-C_3N_4/MoS_2 composite photocatalyst is beneficial to achieve relatively large specific surface area with abundant active sites for the oxidation reactions.

Herein, a g-C_3N_4/MoS_2 photocatalyst was prepared and shown an improved photocatalytic performance for hypophosphite oxidation under visible light irradiation. The structures of the g-C_3N_4/MoS_2 photocatalyst was analyzed by X-ray diffraction (XRD), scanning electron microscopy (SEM), and X-ray photoelectron spectra (XPS). Moreover, the separation mechanism of generated electron-hole pairs was investigated by photoluminescence (PL) emission spectra, and the photocurrent intensity was analyzed by photoluminescence emission spectra. The reactive species generated during the oxidation process were proved by the quenching experiment. The g-C_3N_4/MoS_2 composite was stable after recycle experiments.

2. Experimental

2.1. Chemicals. Melamine ($C_3H_6N_6$), absolute methanol (CH_3OH), sodium molybdate ($Na_2MoO_4{\cdot}2H_2O$), thioacetamide (C_2H_5NS), sodium hypophosphite (NaH_2PO_2), sodium hydroxide (NaOH), sulfuric acid (H_2SO_4), sodium sulfate (Na_2SO_4), and isopropanol ($(CH_3)_2CHOH$) were purchased from Sinopharm Chemical Reagent Co., Ltd. (Beijing, China). All the chemical reagents were analytical grade, and the solutions were prepared using Milli-Q water (Millipore, 18.2 MΩ cm).

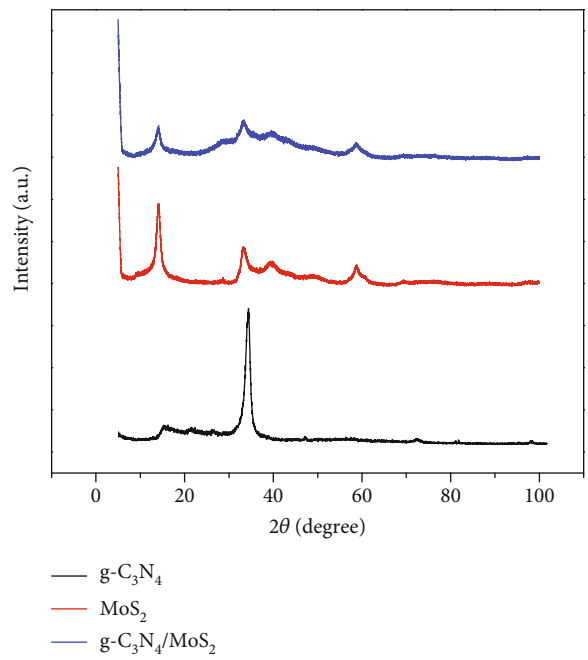

Figure 1: XRD patterns of different materials.

2.2. Preparation of g-C_3N_4. The g-C_3N_4 was prepared as follows: added 5 g melamine into a corundum crucible and then heated at 550°C in a muffle furnace for 2 h to generate a raw g-C_3N_4. Later, the raw g-C_3N_4 was dispersed into 50 mL anhydrous methanol and then stirred return for 3 h under 68~70°C. Later, the mixture was dried at 60°C for 12 h under vacuum drying. Finally, cooled down the mixture and grinded with agate mortars, then the yellow g-C_3N_4 photocatalyst was synthesized [27].

2.3. Synthesis of g-C_3N_4/MoS_2 Composite. The g-C_3N_4/MoS_2 heterojunction was synthesized through the hydrothermal method and shown the following: dissolved 70 mg $Na_2MoO_4{\cdot}2H_2O$ and 140 mg C_2H_5NS into 20 mL deionized water to form a clear solution. Then, added 20 mg g-C_3N_4 into the above solution and ultrasound for 45 minutes to generate suspension solution. After that, added 50 ml suspension solution into the teflon reactor and continuously heated at 220°C for 24 h in the drying oven. When the reaction was finished, washed the product with deionized water and anhydrous ethanol for 3 times and centrifugal separation. Finally, the product was heated at 60°C in a vacuum drying oven for 24 h [28].

2.4. Analysis. The concentration of hypophosphite was analyzed by ion the chromatography method [29]. The surface morphology of the samples was analyzed by scanning electron microscopy (SEM, Quanta FEG 250). The phase structure of the sample was analyzed by X-ray diffraction (XRD, bruker-d8 Advanc type). The surface properties and chemical states of the sample were analyzed by the X-ray

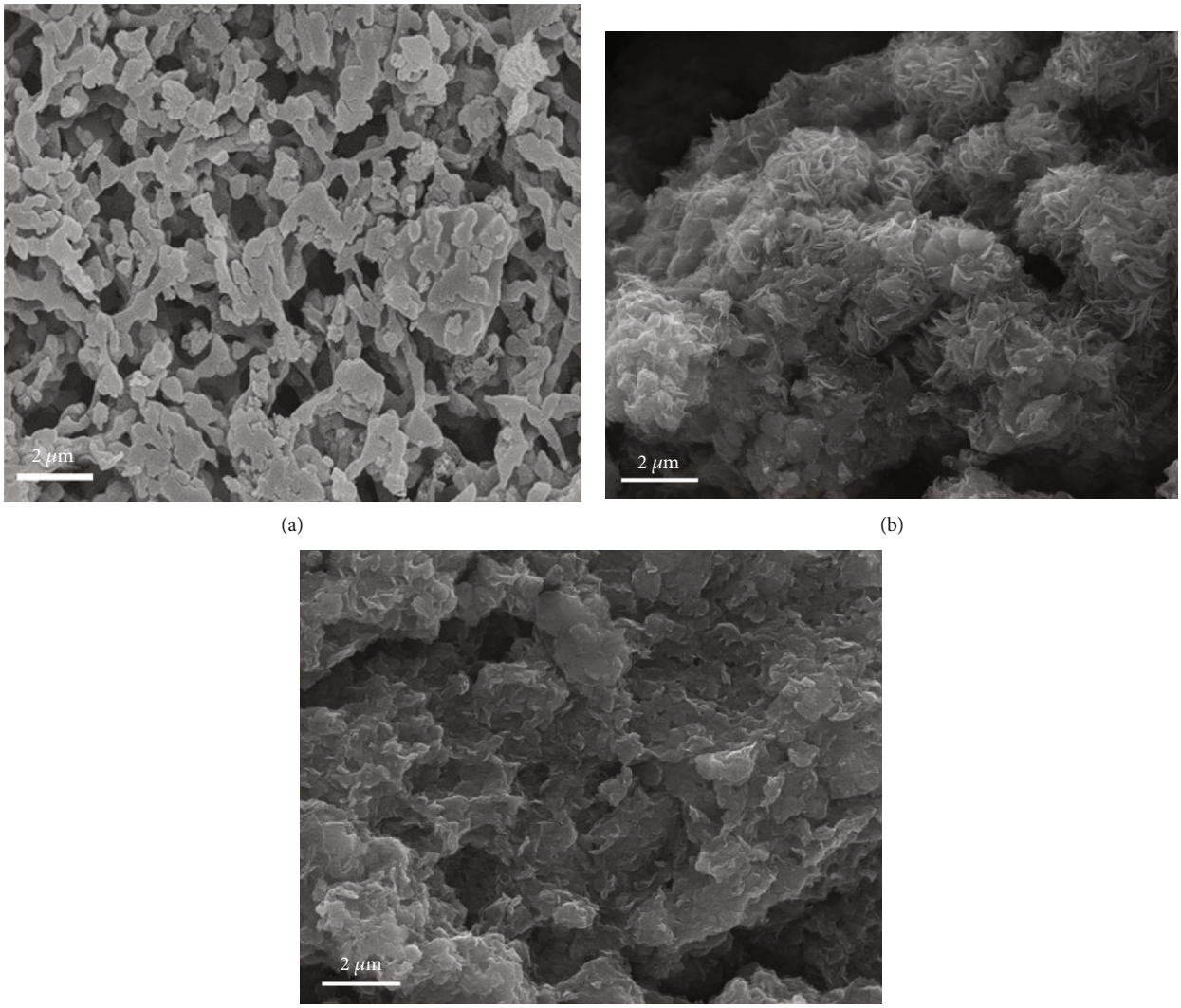

(a) (b) (c)

Figure 2: SEM analysis of different materials: (a) g-C_3N_4, (b) MoS_2, and (c) g-C_3N_4/MoS_2 photocatalyst.

photoelectron spectra (XPS, ULVAC-PHI, INC). The specific surface area and pore size were calculated based on the N_2 physisorption isotherms. At the same time, the photoluminescence spectra were measured with a F-4500 fluorescence (PL) spectrometer, and the photocurrents were measured on a CHI 660B electrochemical system.

2.5. Analysis of Photocatalytic Performance. The photocatalytic performance of the generated photocatalyst was evaluated by the oxidation efficiency of hypophosphite under visible light irradiation. During the oxidation process, the light source (35 W) with a 420 nm UV-cutoff filter was placed 12 cm away from the surface of reaction solution. For each photocatalytic experiment, 5 mg photocatalyst was added into the hypophosphite solution (50 ml, 50 mg L^{-1}). Before irradiation reaction, the solution was continuously stirred in the dark for 2 h until the adsorption saturation was reached. A small amount of hypophosphite solution was measured every 15 min, and the change of the hypophosphite concentration solution was measured to evaluate the photocatalytic performance of the prepared photocatalyst. The oxidation efficiency of hypophosphite was measured as follows:

$$\eta = \frac{C_0 - C_t}{C_0} \times 100\%, \quad (1)$$

where C_0 was the initial concentration of hypophosphite (mg L^{-1}); C_t was the concentration of hypophosphite after irradiation for a certain time t (min).

3. Results and Discussion

3.1. Analysis of Structure and Morphology for Different Materials. XRD patterns of the synthesized photocatalyst were analyzed to characterize the crystalline phases and were shown in Figure 1. Two characteristics peaks were observed at 13.2° and 27.6° for pure g-C_3N_4 photocatalysts. The characteristics peaks observed at 13.2° and 27.6° were indexed as the (110) plane corresponding to the in-plane structure, and the diffraction peak at 27.6° was corresponded to

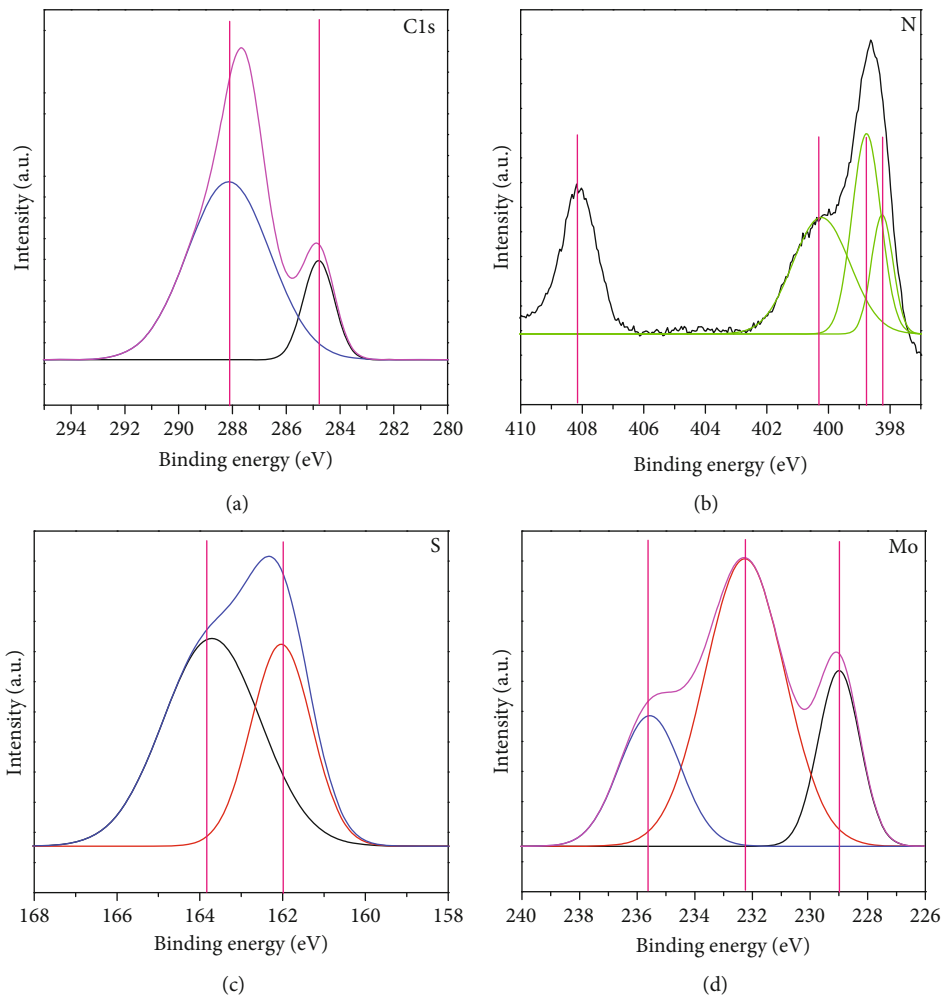

Figure 3: XPS spectra of the g-C_3N_4/MoS_2 photocatalyst: (a) C, (b) N, (c) S, and (d) Mo.

interlayer stacking of the conjugated aromatic systems [30]. In addition, two characteristics peaks at 32.7° and 56.7° were observed, which were contributed to the (100) and (110) crystal planes of MoS_2 (JCPDS No. 37-1492) [31]. According to the results, the formation of g-C_3N_4/MoS_2 photocatalysts was successfully synthesized.

The microstructure of the different materials was shown in Figure 2, layered g-C_3N_4 showed many thin nanosheets with a porous structure (Figure 2(a)), and the pure MoS_2 particles showed a flower-like nanostructure with thin nanosheets avoiding the disordered stacking of MoS_2 layers (Figure 2(b)). Moreover, the g-C_3N_4/MoS_2 photocatalyst was mainly composed of rhabditiform crystals, and the shape of the synthesized g-C_3N_4/MoS_2 photocatalyst was relatively uniform (Figure 2(c)).

To identify the elements and interaction of as-prepared samples, the XPS spectra of g-C_3N_4/MoS_2 were investigated. As shown in Figure 3(a), the high-resolution XPS spectrum of C 1 s exhibited two peaks at 284.8 and 288.2 eV in the g-C_3N_4/MoS_2 photocatalyst assigned to C–C and N=C(–N)$_2$ of g-C_3N_4, respectively [32]. In the N 1s XPS spectrum (Figure 3(b)), peaks at 398.3, 398.9 and 400.4 eV in the g-C_3N_4/MoS_2 photocatalyst were assigned to C–N, tertiary nitrogen N-C_3, and C-N-H groups, respectively [33]. The characteristic peaks of $2p_{1/2}$ and $2p_{3/2}$ orbitals for S^{2-} were observed at 162.9 and 161.9 eV in the g-C_3N_4/MoS_2 photocatalyst, respectively (Figure 3(c)) [34]. The Mo 3d XPS spectrum of the g-C_3N_4/MoS_2 photocatalyst showed that the two peaks centered at 229.4 and 232.6 eV (Figure 3(d)) assigned to Mo $3d_{5/2}$ and Mo $3d_{3/2}$, respectively, demonstrating that Mo was in the +4 valence state [35].

3.1.1. Surface Area and Pore Size Distribution. The nitrogen adsorption-desorption isotherms and pore size distribution of different materials were shown in Figure 4. The specific surface area was calculated to be 114.5, 55.4,, and 147.3 $m^2 g^{-1}$ for MoS_2, g-C_3N_4, and g-C_3N_4/MoS_2 photocatalysts, respectively (Figure 4(a)). Generally, a catalyst with larger surface area could provide many active sites for adsorption and photodegradation towards organic pollutants, resulting in improving the photodecomposition performance. As a result, g-C_3N_4/MoS_2 photocatalysts with higher specific surface area were benefit for improving the photocatalytic oxidation of hypophosphite. Moreover, the pore size distribution of g-C_3N_4/MoS_2 was between 5 and 15 nm, and that of pure MoS_2 was mainly in the range of 10–25 nm, while no obvious mesopore structure was observed for g-C_3N_4 (Figure 4(b)).

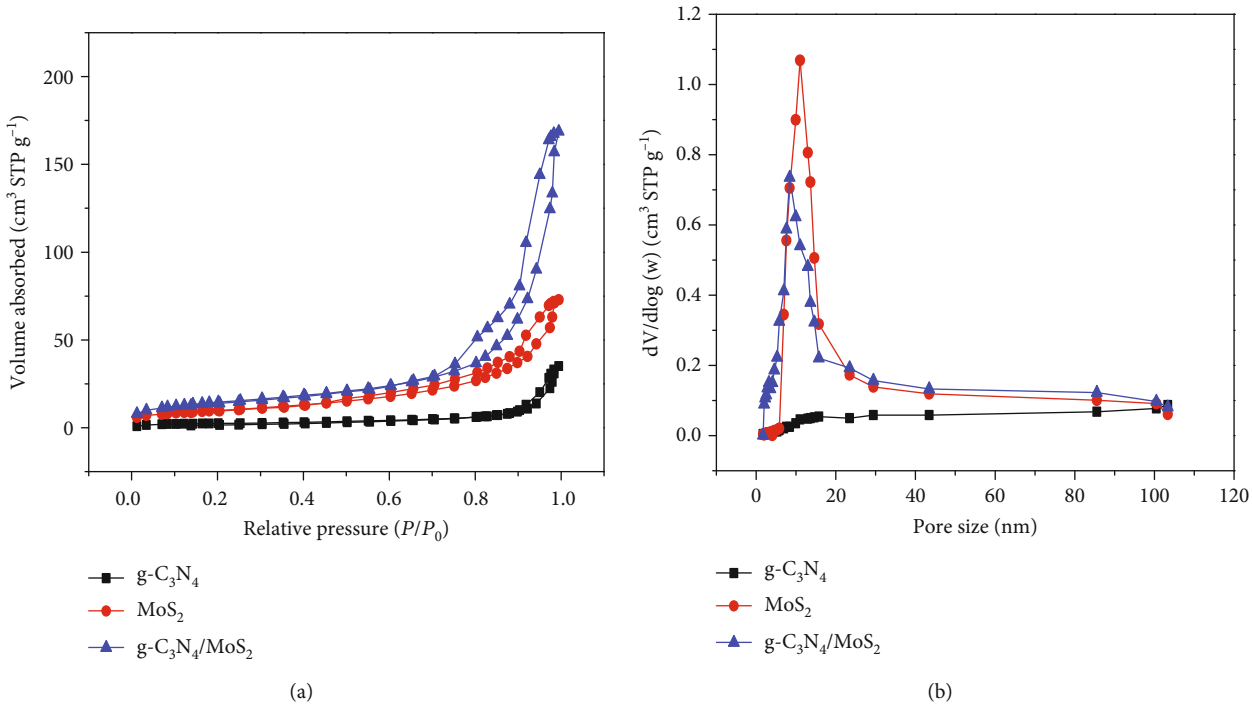

Figure 4: (a) Isotherms of nitrogen adsorption and desorption and (b) BJH adsorption pore size distribution of g-C_3N_4, MoS_2, and g-C_3N_4/MoS_2.

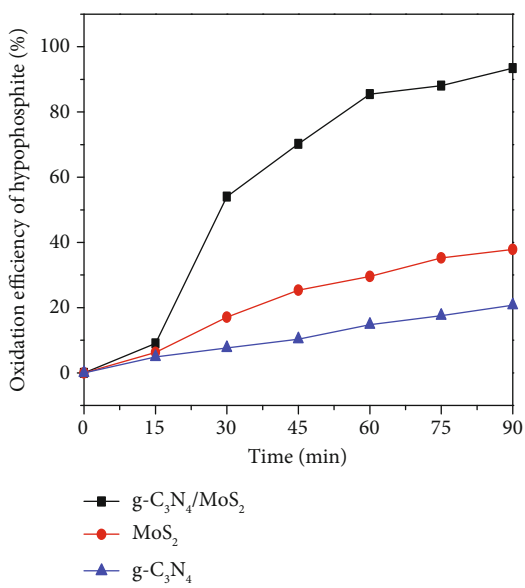

Figure 5: The comparison of oxidation efficiency of hypophosphite for different photocatalysts.

3.2. Analysis of Photocatalytic Activity for Different Photocatalysts. The oxidation efficiency of hypophosphite for different photocatalysts was shown in Figure 5. The oxidation efficiency of hypophosphite for pure g-C_3N_4 indicated the lowest photocatalytic performance (20.87%) due to the fast recombination of photo-generated electrons and holes, and the oxidation efficiency of hypophosphite for g-C_3N_4/MoS_2 photocatalyst was the highest (93.45%). The photogenerated electrons were transferred from g-C_3N_4 to MoS_2, which could efficiently improve the separate rate of photogenerated electrons and holes. The existence of heterostructure for g-C3N4/MoS2compositelimited the recombination of photogenerated electrons and holes. Therefore, the photocatalytic performance of the g-C_3N_4/MoS_2 photocatalyst was improved compared with the pure g-C_3N_4 and MoS_2 photocatalyst.

3.3. Analysis of Photoluminescence Emission Spectra and Electrochemical Properties. Enhanced photoactivity performance was ascribed to the fast separation of photogenerated electrons and holes, as confirmed by the photoluminescence technique and transient photocurrent response measurement [36]. According to PL results, the PL spectrum could directly reflect the separation efficiency of photogenerated electron-hole pairs, i.e., the higher intensity of the PL spectrum and the higher recombination rate of photogenerated electron-hole pairs [37, 38]. The PL spectrum of the photocatalyst was shown in Figure 6(a), and all the photocatalysts exhibited a broad emission peak centered at around 460 nm. The PL intensity exhibited the highest value for pure g-C_3N_4 photocatalyst, while the intensity had become weaker for the g-C_3N_4/MoS_2 composite photocatalyst, which was attributed to the improvement of the electron transport induced by quantum confinement effect. Moreover, for the g-C_3N_4/MoS_2 photocatalyst, the interaction for g-C_3N_4 and MoS_2 in the redox potential, it caused the photogenerated electrons transfer from g-C_3N_4 to MoS_2, thus reducing the probability of its recombination with holes. In addition, comparing the pure MoS_2, a distinct red shift was shown, indicating that the g-C_3N_4/MoS_2 photocatalysts were more efficient in light harvesting under visible light irradiation.

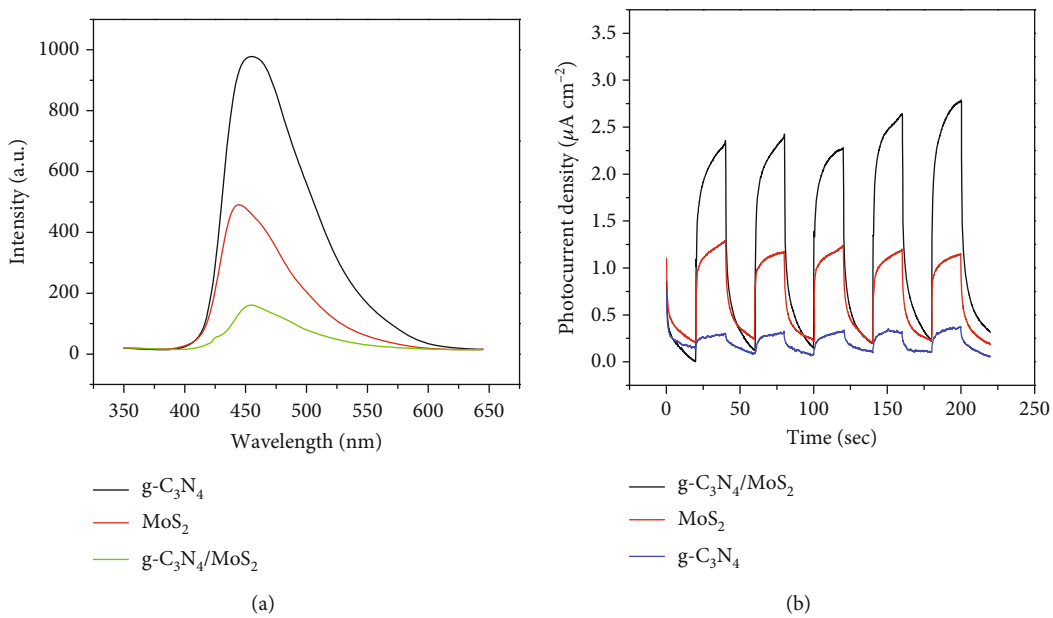

Figure 6: The PL spectra and photocurrent density for different photocatalyst.

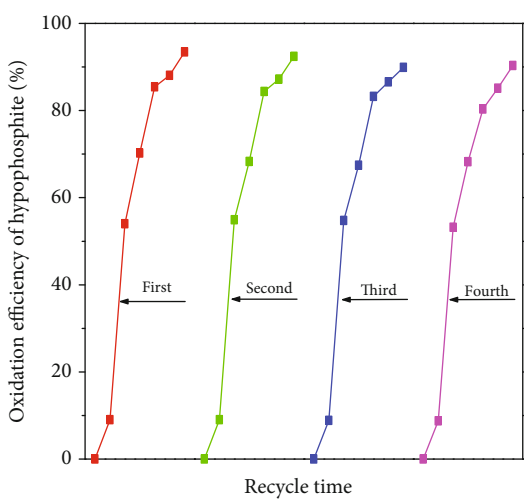

Figure 7: The stability analysis of the g-C_3N_4/MoS_2 photocatalyst after recycling experiments.

In addition, the separation of photoinduced carriers of the composites was clarified by the transient photocurrent response measurement [39]. To confirm superior photoinduced carriers in the composites of the g-C_3N_4/MoS_2 photocatalyst, the photocurrent response was evaluated in Na_2SO_4 electrolyte [40]. As shown in Figure 6(b), when the g-C_3N_4/MoS_2 electrodes were irradiated under visible light, it showed rapid responsive photocurrents. Moreover, comparing with the pure g-C_3N_4 (0.25 μA cm^{-2}) and MoS_2 (1.25 μA cm^{-2}), the g-C_3N_4/MoS_2 composites showed 10 times improved photocurrent intensity and 2 times improved photocurrent intensity, respectively. The photocurrent responses were repeatable during on/off cycles under visible light irradiation.

3.4. Analysis of Stability Performance for the Prepared g-C_3N_4/MoS_2 Photocatalysts. The stability of the prepared g-C_3N_4/MoS_2 photocatalysts was an important consideration to evaluate the practical applications through four recycling experiments [41]. After each cycle, all the used photocatalysts were collected together, centrifuged, and washed with distilled water, then dried at 60°C overnight. As shown in Figure 7, the oxidation efficiency of hypophosphite in the recycling experiments was 93.45%, 92.43%, 89.89%, and 90.32%, respectively, which indicated that the structure of photocatalyst was stable during the oxidation of hypophosphite. The results of recycling experiments indicated that the prepared g-C_3N_4/MoS_2 photocatalyst had a strong binding force, which effectively reduced the dissolution of the bulk g-C_3N_4 material during the photocatalytic process. Therefore, the g-C_3N_4/MoS_2 photocatalyst had a good stability in the oxidation of hypophosphite.

3.5. Photocatalytic Mechanism of Hypophosphite Oxidation. To analyze the mechanism of photocatalytic oxidation of hypophosphite, the active oxygen species produced under the visible light irradiation were analyzed through the quenching experiment. According to some literature, isopropanol (IPA) worked as the radical quencher for ·OH radical, while the N_2 purging was used to reduce the superoxide $O_2\cdot^-$ radicals [42, 43]. By the ways of adding different scavengers into reaction solutions to remove the corresponding reactive species, the functions of the corresponding reactive species generated in the photocatalytic process was related to the change of the photocatalytic oxidation efficiency of hypophosphite. As shown in Figure 8, the photocatalytic oxidation efficiency of hypophosphite was 93.45% without scavengers. When the IPA was added into reaction solution, and the photocatalytic oxidation efficiency of hypophosphite was decreased to 63%. When N_2 was blowing into reaction

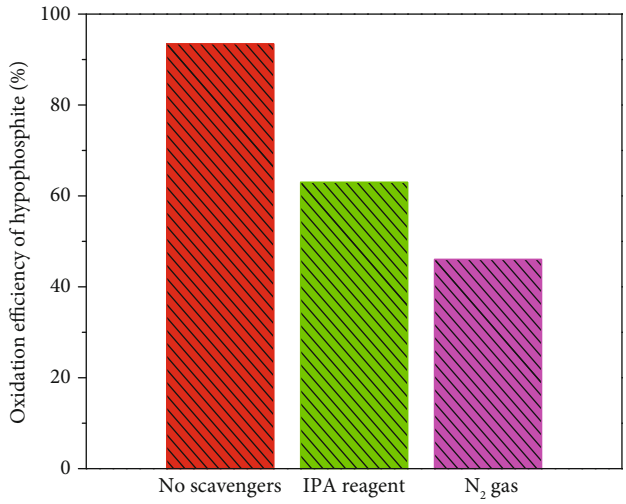

Figure 8: Effect of a series of scavengers on the photocatalytic oxidation of hypophosphite.

solution, the photocatalytic oxidation efficiency of hypophosphite was decreased to 46%. According to the results, it was clear that both ·OH and $O_2\cdot^-$ radicals were the major reactive species in the photocatalytic reaction system for hypophosphite oxidation. Accordingly, the ·OH and $O_2\cdot^-$ radials had a strong oxidation ability during the photocatalytic oxidation of hypophosphite.

The mechanism of the photocatalytic oxidation of hypophosphite was shown as follows: Firstly, the semiconductor materials (g-C_3N_4/MoS_2) absorbed the visible light, and the electron-hole pairs were generated on the surface of photocatalyst. Then, hydroxyl radical was generated through the oxidation of hydroxyl ions (OH^-) with holes. In addition, the superoxide anions were also generated by the molecular reduction of O_2, which may attribute to the presence of electrons on the surface of the photocatalyst. The reactive species generated in the photocatalytic system were responsible for hypophosphite oxidation. Furthermore, the photogenerated holes were also responsible for the direct oxidation of the hypophosphite.

4. Conclusion

In the photocatalyst system, the composite g-C_3N_4/MoS_2 indicated higher photocatalytic performance comparing with the pure g-C_3N_4 and MoS_2 photocatalyst. The oxidation efficiency of hypophosphite for the g-C_3N_4/MoS_2 photocatalyst was 93.45%, while the oxidation efficiency of hypophosphite for g-C_3N_4 and MoS_2 were 20.78% and 37.87%, respectively. The mechanism of the improved photocatalytic performance of the g-C_3N_4/MoS_2 photocatalyst for hypophosphite oxidation was analyzed by the photoluminescence technique and transient photocurrent response measurement. The recombination rate of photogenerated electron-hole pairs was reduced, which improved the photocatalytic activity. Moreover, the generated active species were responsible for hypophosphite oxidation analyzed by the quenching experiment. OH and $O_2\cdot^-$ radials were responsible for the oxidation of hypophosphite. The results of recycling experiments indicated that the g-C_3N_4/MoS_2 photocatalyst had a good stability for hypophosphite oxidation. Therefore, the g-C_3N_4/MoS_2 photocatalyst was an efficient and promising materials for the application of hypophosphite oxidation under visible light irradiation.

Data Availability

The data used to support the findings of this study are available from the corresponding author upon request.

Conflicts of Interest

There are no conflicts to declare.

Acknowledgments

This work was supported by the Ecological Environment Bureau Project of Chongqing (PM-zx555-201911-361); South China Institute of Environmental Sciences, Ministry of Ecological Environment (MEE) Project of Guangzhou (PM-zx703-201904-135); Science and Technology Planning Project of Guangzhou (2017A0103002).

References

[1] A. Stankiewicz, Z. Kefallinou, G. Mordarski, Z. Jagoda, and B. Spencer, "Surface functionalisation by the introduction of self-healing properties into electroless Ni-P coatings," *Electrochimica Acta*, vol. 297, pp. 427–434, 2019.

[2] S. Li, G. Song, Q. Fu, and C. Pan, "Preparation of Cu- graphene coating via electroless plating for high mechanical property and corrosive resistance," *Journal of Alloys and Compounds*, vol. 777, pp. 877–885, 2019.

[3] W. Guan, Z. Zhang, S. Tian, and J. Du, "Ti4O7/g-C3N4 for Visible Light Photocatalytic Oxidation of Hypophosphite: Effect of Mass Ratio of Ti4O7/g-C3N4," *Front. Chem*, vol. 6, 2018.

[4] W. Guan, S. Tian, N. Ma, and X. Zhao, "An electrochemical method through hydroxyl radicals oxidation and deposition of ferric phosphate for hypophosphite recovery," *Journal of Colloid and Interface Science*, vol. 516, pp. 529–536, 2018.

[5] S. Tian and Z. Zhang, "Photo-electrochemical oxidation of hypophosphite and phosphorous recovery by UV/Fe^{2+}/-peroxydisulfate with electrochemical process," *Chemical Engineering Journal*, vol. 359, pp. 1075–1085, 2019.

[6] T. S. Natarajan, K. R. Thampi, and R. J. Tayade, "Visible light driven redox-mediator-free dual semiconductor photocatalytic systems for pollutant degradation and the ambiguity in applying Z-scheme concept," *Applied Catalysis B: Environmental*, vol. 227, pp. 296–311, 2018.

[7] M. Martin-Somer, C. Pablos, A. de Diego et al., "Novel macroporous 3D photocatalytic foams for simultaneous wastewater disinfection and removal of contaminants of emerging concern," *Chemical Engineering Journal*, vol. 366, pp. 449–459, 2019.

[8] Y. Ye, H. Bruning, X. Li, D. Yntema, and H. H. M. Rijnaarts, "Significant enhancement of micropollutant photocatalytic degradation using a TiO_2 nanotube array photoanode based photocatalytic fuel cell," *Chemical Engineering Journal*, vol. 354, pp. 553–562, 2018.

[9] X. Hu, Z. Sun, J. Song, G. Zhang, C. Li, and S. Zheng, "Synthesis of novel ternary heterogeneous BiOCl/TiO_2/sepiolite composite with enhanced visible-light-induced photocatalytic activity towards tetracycline," *Journal of Colloid and Interface Science*, vol. 533, pp. 238–250, 2019.

[10] G. Wang, Q. Zhang, Q. Chen et al., "Photocatalytic degradation performance and mechanism of dibutyl phthalate by graphene/TiO_2 nanotube array photoelectrodes," *Chemical Engineering Journal*, vol. 358, pp. 1083–1090, 2019.

[11] W. Guan and S. Tian, "An effect of crucible volume on the microstructure and Photocatalytic activity of the prepared g-C_3N_4," *Journal of Nanoelectronics and Optoelectronics*, vol. 12, no. 8, pp. 781–785, 2017.

[12] S. Wu, H.-J. Zhao, C.-F. Li et al., "Type II heterojunction in hierarchically porous zinc oxide/graphitic carbon nitride microspheres promoting photocatalytic activity," *Journal of Colloid and Interface Science*, vol. 538, pp. 99–107, 2019.

[13] G. Zhao, H. Yang, M. Liu, and X. Xu, "Metal-Free Graphitic Carbon Nitride Photocatalyst Goes into Two-Dimensional Time," *Frontiers in Chemistry*, vol. 6, 2018.

[14] W. Guan, G. Sun, L. Yin, Z. Zhang, and S. Tian, "Ti4O7/g-C3N4 Visible Light Photocatalytic Performance on Hypophosphite Oxidation: Effect of Annealing Temperature," *Frontiers in Chemistry*, vol. 6, 2018.

[15] W. Kong, X. Zhang, B. Chang et al., "Fabrication of B doped g-C3N4/TiO2 heterojunction for efficient photoelectrochemical water oxidation," *Electrochim. Acta*, vol. 282, pp. 767–774, 2018.

[16] W. Liu, Y. Li, F. Liu, W. Jiang, D. Zhang, and J. Liang, "Visible-light-driven photocatalytic degradation of diclofenac by carbon quantum dots modified porous g-C_3N_4: mechanisms, degradation pathway and DFT calculation," *Water Research*, vol. 151, pp. 8–19, 2019.

[17] J. Dong, Y. Shi, C. Huang, Q. Wu, T. Zeng, and W. Yao, "A new and stable Mo-Mo_2C modified g-C_3N_4 photocatalyst for efficient visible light photocatalytic H_2 production," *Applied Catalysis B: Environmental*, vol. 243, pp. 27–35, 2019.

[18] J. Jing, Z. Chen, and C. Feng, "Dramatically enhanced photoelectrochemical properties and transformed p/n type of g-C_3N_4 caused by K and I co-doping," *Electrochimica Acta*, vol. 297, pp. 488–496, 2019.

[19] S. Mao, R. Bao, D. Fang, and J. Yi, "Fabrication of sliver/graphitic carbon nitride photocatalyst with enhanced visible-light photocatalytic efficiency through ultrasonic spray atomization," *Journal of Colloid and Interface Science*, vol. 538, pp. 15–24, 2019.

[20] Y. Liu, Y. Li, F. Peng et al., "2H- and 1T- mixed phase few-layer MoS_2 as a superior to Pt co-catalyst coated on TiO_2 nanorod arrays for photocatalytic hydrogen evolution," *Applied Catalysis B: Environmental*, vol. 241, pp. 236–245, 2019.

[21] K. Roy, M. Padmanabhan, S. Goswami, T. P. Sai, S. Kaushal, and A. Ghosh, "Optically active heterostructures of graphene and ultrathin MoS_2," *Solid State Communications*, vol. 175-176, pp. 35–42, 2013.

[22] N. Ekthammathat, S. Thongtem, T. Thongtem, and A. Phuruangrat, "Characterization and antibacterial activity of nanostructured ZnO thin films synthesized through a hydrothermal method," *Powder Technology*, vol. 254, pp. 199–205, 2014.

[23] H. Li, H. Shen, L. Duan et al., "Enhanced photocatalytic activity and synthesis of ZnO nanorods/MoS_2 composites," *Superlattices and Microstructures*, vol. 117, pp. 336–341, 2018.

[24] O. Yayapao, T. Thongtem, A. Phuruangrat, and S. Thongtem, "Synthesis and characterization of highly efficient Gd doped ZnO photocatalyst irradiated with ultraviolet and visible radiations," *Materials Science in Semiconductor Processing*, vol. 39, pp. 786–792, 2015.

[25] X. Bai, Y. Du, X. Hu et al., "Synergy removal of Cr (VI) and organic pollutants over RP-MoS_2/rGO photocatalyst," *Applied Catalysis B: Environmental*, vol. 239, pp. 204–213, 2018.

[26] J. Akhtar, M. B. Tahir, M. Sagir, and H. S. Bamufleh, "Improved photocatalytic performance of Gd and Nd co-doped ZnO nanorods for the degradation of methylene blue," *Ceramics International*, vol. 46, no. 8, pp. 11955–11961, 2020.

[27] C. Liang, L. Zhang, H. Guo et al., "Photo-removal of 2,2′4,4′-tetrabromodiphenyl ether in liquid medium by reduced graphene oxide bridged artificial Z-scheme system of Ag@Ag_3PO_4/g-C_3N_4," *Chemical Engineering Journal*, vol. 361, pp. 373–386, 2019.

[28] D. Lu, H. Fan, K. K. Kondamareddy et al., "Highly efficient visible-light-induced Photocatalytic production of hydrogen for magnetically retrievable Fe3O4@SiO2@MoS2/g-C3N4Hierarchical microspheres," *ACS Sustainable Chemistry & Engineering*, vol. 6, no. 8, pp. 9903–9911, 2018.

[29] M. M. McDowell, M. M. Ivey, M. E. Lee et al., "Detection of hypophosphite, phosphite, and orthophosphate in natural geothermal water by ion chromatography," *Journal of Chromatography. A*, vol. 1039, no. 1-2, pp. 105–111, 2004.

[30] X. Yang, L. Tian, X. Zhao, H. Tang, Q. Liu, and G. Li, "Interfacial optimization of g-C_3N_4-based Z-scheme heterojunction toward synergistic enhancement of solar-driven photocatalytic oxygen evolution," *Applied Catalysis B: Environmental*, vol. 244, pp. 240–249, 2019.

[31] J. Liu, X. Mu, Y. Yang et al., "Construct 3D Pd@MoS_2-conjugated polypyrrole framworks Heterojunction with unprecedented photocatalytic activity for Tsuji-Trost reaction under visible light," *Applied Catalysis B: Environmental*, vol. 244, pp. 356–366, 2019.

[32] X. Shi, M. Fujitsuka, S. Kim, and T. Majima, "Faster Electron injection and more active sites for efficient Photocatalytic H2Evolution in g-C3N4/MoS2Hybrid," *Small*, vol. 14, no. 11, pp. 1703277–1703286, 2018.

[33] V. R. Battula, S. Kumar, D. K. Chauhan, S. Samanta, and K. Kailasam, "A true oxygen-linked heptazine based polymer for efficient hydrogen evolution," *Applied Catalysis B: Environmental*, vol. 244, pp. 313–319, 2019.

[34] X. Fan, Y. Zhou, G. Zhang, T. Liu, and W. Dong, "In situ photoelectrochemical activation of sulfite by MoS_2 photoanode for enhanced removal of ammonium nitrogen from wastewater," *Applied Catalysis B: Environmental*, vol. 244, pp. 396–406, 2019.

[35] Y. Dong, C. Huang, and X.-Y. Yang, "Underwater superoleophobic and underoil superhydrophobic surface made by liquid-exfoliated MoS_2 for on-demand oil-water separation," *Chemical Engineering Journal*, vol. 361, pp. 322–328, 2019.

[36] H. Liu, L. Li, C. Guo, J. Ning, Y. Zhong, and Y. Hu, "Thickness-dependent carrier separation in $Bi_2Fe_4O_9$ nanoplates with enhanced photocatalytic water oxidation," *Chemical Engineering Journal*, vol. 385, p. 123929, 2020.

[37] L. Li, C. Guo, J. Shen, J. Ning, Y. Zhong, and Y. Hu, "Construction of sugar-gourd-shaped CdS/Co1-xS hollow heteronanostructure as an efficient Z-scheme photocatalyst for hydrogen generation," *Chemical Engineering Journal*, vol. 400, p. 125925, 2020.

[38] H. Zhang, C. Guo, J. Ren et al., "Beyond CoO_x: a versatile amorphous cobalt species as an efficient cocatalyst for visible-light-driven photocatalytic water oxidation," *Chemical Communications*, vol. 55, no. 93, pp. 14050–14053, 2019.

[39] X. Jin, F. Chen, D. Jia et al., "Influences of synthetic conditions on the photocatalytic performance of ZnS/graphene composites," *Journal of Alloys and Compounds*, vol. 780, pp. 299–305, 2019.

[40] C. Zhai, M. Sun, L. Zeng et al., "Construction of Pt/graphitic C_3N_4/MoS_2 heterostructures on photo-enhanced electrocatalytic oxidation of small organic molecules," *Applied Catalysis B: Environmental*, vol. 243, pp. 283–293, 2019.

[41] S. Tian, C. Dang, R. Mao, and X. Zhao, "Enhancement of Photoelectrocatalytic oxidation of cu–cyanide complexes and Cathodic recovery of cu in a metal-free system," *ACS Sustainable Chemistry & Engineering*, vol. 6, no. 8, pp. 10273–10281, 2018.

[42] N. Seriani, C. Pinilla, and Y. Crespo, "Presence of gap states at Cu/TiO2Anatase surfaces: consequences for the Photocatalytic activity," *Journal of Physical Chemistry C*, vol. 119, no. 12, pp. 6696–6702, 2015.

[43] S. Tian, Y. Li, and X. Zhao, "Cyanide removal with a copper/-active carbon fiber cathode via a combined oxidation of a Fenton-like reaction and in situ generated copper oxides at anode," *Electrochimica Acta*, vol. 180, pp. 746–755, 2015.

Hindawi
Journal of Nanomaterials
Volume 2020, Article ID 9797509, 15 pages
https://doi.org/10.1155/2020/9797509

Research Article

Simultaneous Voltammetric Determination of Uric Acid, Xanthine, and Hypoxanthine Using $CoFe_2O_4$/Reduced Graphene Oxide-Modified Electrode

Nguyen Thi Vuong Hoan,[1] Nguyen Ngoc Minh,[1] Nguyen Thi Hong Trang,[1] Le Thi Thanh Thuy,[1] Cao Van Hoang,[1] Tran Xuan Mau,[2] Ho Xuan Anh Vu,[3] Phan Thi Kim Thu,[3,4] Nguyen Hai Phong,[3] and Dinh Quang Khieu[3]

[1]*Quy Nhon University, 55000, Vietnam*
[2]*Hue University, 49000, Vietnam*
[3]*University of Sciences, Hue University, 49000, Vietnam*
[4]*Daklak Junior College of Education, 63000, Vietnam*

Correspondence should be addressed to Nguyen Thi Vuong Hoan; nguyenthivuonghoan@qnu.edu.vn, Phan Thi Kim Thu; kimthu1912@gmail.com, Nguyen Hai Phong; nhphong@hueuni.edu.vn, and Dinh Quang Khieu; dqkhieu@hueuni.edu.vn

Received 10 March 2020; Revised 5 June 2020; Accepted 22 June 2020; Published 10 July 2020

Guest Editor: Changfa Guo

In the present paper, the synthesis of cobalt ferrite/reduced graphene oxide ($Co_2Fe_2O_4$/rGO) composite and its use for the simultaneous determination of uric acid (UA), xanthine (XA), and hypoxanthine (HX) is demonstrated. Cobalt ferrite hollow spheres were synthesized by using the carbonaceous polysaccharide microspheres prepared from a *D*-glucose solution as templates, followed by calcination. The $CoFe_2O_4$/rGO composite was prepared with the ultrasound-assisted method. The obtained material was characterized by using X-ray diffraction, scanning electron microscopy, X-ray photoelectron spectroscopy, EDX elemental mapping, and nitrogen adsorption/desorption isotherms. The electrochemical behavior of UA, XA, and HX on the $CoFe_2O_4$/rGO-modified electrode was studied with cyclic voltammetry and differential pulse voltammetry (DPV). The modified electrode exhibits excellent electrocatalytic activity towards the oxidation of the three compounds. The calibration curves for UA, XA, and HX were obtained over the range of 2.0–10.0 μM from DPV. The limits of detection for UA, XA, and HX are 0.767, 0.650, and 0.506 μM, respectively. The modified electrode was applied to the simultaneous detection of UA, XA, and HX in human urine, and the results are consistent with those obtained from the high-performance liquid chromatography technique.

1. Introduction

Uric acid (UA: 7,9-dihydro-1*H*-purine-2,6,8(3*H*)-trione), xanthine (XA: 3,7-dihydropurine-2,6-dione), and hypoxanthine (HX: 1*H*-purin-6(9*H*)-one) are oxidation products of purine nucleotide and deoxynucleotide metabolisms in human beings. The concentration of these products in human serum and urine is of great importance for clinical diagnoses, such as gout, hyperuricemia, leukemia, and pneumonia [1]. The purine oxidation products are simultaneously determined with different techniques, such as capillary electrophoresis [2], enzymatic spectrophotometry [3], and high-performance liquid chromatography [4, 5]. However, these methods require complicated sample preparation, expensive material, and considerable time. As a result, they have limited applications. One of the alternatives to this challenge is electrochemical approaches that have attracted great interest owing to their inherent advantages, such as simplicity, high sensitivity, and low cost. The development of electrochemical analysis based on chemically modified

electrodes is a major interest in current research [6, 7]. Several electrode modifiers, such as Ru $(DMSO)_4Cl_2$ nanoaggregated Nafion [7], poly(bromocresol purple) [8], and poly-(L-arginine)/graphene composite [9], have been used for the simultaneous determination of UA, XA, and HX.

The synthesis and design of new electrode modifiers with numerous electrochemical sensing properties have been a great concern to many scientists. One of these modifiers is cobalt ferrite ($CoFe_2O_4$). Although cobalt ferrite has excellent magnetic properties, high coactivity and hardness, and moderate saturation magnetization and is used in magnetic devices, gas sensor application [10, 11], and surface-active Co(II), it has not attracted much attention in the electrochemical analysis [12]. Cobalt ferrite has a low surface area because aggregation usually occurs owing to the high surface energy of the nanoparticles, deteriorating the electrochemical activity of the material. To limit its aggregation, two approaches have usually been employed: (i) the synthesis of $CoFe_2O_4$ in hierarchical structures (e.g., rods, urchins, and flower-like structures) and (ii) dispersion of $CoFe_2O_4$ nanoparticles in carriers with a large surface area. Related to the latter, cobalt ferrite has usually been dispersed in organic or inorganic substrates. The cobalt ferrite-based materials have been employed to develop the novel electrodes for voltammetric determination of some compounds. Han et al. reported the synthesis of β-cyclodextrin-cobalt-ferrite nanocomposite to modify an electrode for catechol determination [13], Yardımcı et al. used cobalt ferrite/chitosan nanocomposite for H_2O_2 sensing [14], and Ensafi et al. determined H_2O_2 and nicotinamide adenine dinucleotide by using a cobalt ferrite/graphene oxide-modified electrode [15].

Besides graphene oxide, a derivative of this material—reduced graphene oxide (rGO)—is also an excellent substrate to disperse cobalt ferrite. The rGO with smaller oxygen content is produced from graphene oxide via chemical, thermal, or other approaches. The rGO possesses good conductivity and thermal and chemical stability [16, 17] that makes it to be used as a novel material to develop the electrodes for electrochemical sensing biomolecules [18, 19], metal ions [20], and toxic chemicals [21]. Therefore, a combination of $CoFe_2O_4$ with rGO is expected to result in a composite with a high surface area and electrical conductivity and a possibility of application in electrochemistry. To the best of our knowledge, the use of the $CoFe_2O_4$/rGO composite as an electrode modifier for the determination of UA, XA, and HA by using the voltammetry method is very limited in the literature.

In the present work, we prepared cobalt ferrite hollow spheres to fabricate a $CoFe_2O_4$/rGO-modified electrode. Then, we used this electrode to study the electrochemical behaviors on UA, XA, and HA oxidations by using cyclic and differential pulse voltammetry. We also addressed the analysis of real samples.

2. Experimental

2.1. Materials and Synthesis

2.1.1. Materials. All reagents are of analytical grade. Graphite (C), cobalt nitrate hexahydrate ($Co(NO_3)\cdot 6H_2O$), ferrous sulfate heptahydrate ($FeSO_4\cdot 7H_2O$), uric acid ($C_5H_4N_4O_3$), xanthine ($C_{19}H_{16}N_4O_2$) and hypoxanthine ($C_5H_4N_4O$), and hydrochloric acid (HCl) are from Sigma-Aldrich. Acetic acid (CH_3COOH), phosphoric acid (H_3PO_4), boric acid (H_3BO_3), ammonia solution (NH_3, 25%), ethanol (C_2H_5OH), hydroperoxide (H_2O_2, 30%), and potassium hydroxide (KOH) were purchased from Daejung (Korea). The Britton–Robinson buffer solution (B–RBS) in the range of pH 2.0–10.0 was prepared from 1.0 M H_3BO_3, 1.0 M H_3PO_4, and 1.0 M CH_3COOH and was adjusted with 1 M KOH. The phosphate buffer solution (PBS) with pH 7 was prepared from 0.5 M Na_2HPO_4, 0.5 M KH_2PO_4, 0.5 M NaCl, and 0.5 M KCl. The UA, XA, and HX 2.0×10^{-5} mol · L^{-1} standard aqueous solutions were prepared in a 0.2 mol·L^{-1} phosphate buffer solution (pH 5) or Britton–Robinson buffer solution. Double distilled water was used to prepare all the solutions.

2.1.2. Synthesis of Cobalt Ferrite. The synthesis of $CoFe_2O_4$ hollow spheres was performed by adding 4 g of glucose, 1.477 g of $Co(NO_3)_2\cdot 6H_2O$, and 2.808 g of $FeSO_4\cdot 7H_2O$ to 40 mL of distilled water to give a homogeneous solution. This mixture was then transferred to a Teflon-lined autoclave (100 mL) for treatment at 185°C for 8 h. The black solid was separated via centrifugation and dried in an oven at 80°C for 5 h and calcined at 500°C for 5 h. The resulting product is cobalt ferrite ($Co_2Fe_2O_4$).

2.1.3. Synthesis of Reduced Graphene Oxide. Graphite oxide (GrO) was prepared by using Hummers' process [22]. A mixture of 2 g of GrO and 500 mL of double distilled water was stirred under ultrasonication for 5 h to get a graphene oxide suspension (GO) (4 mg/mL GO). The GO suspension (12.5 mL GO in 250 mL distilled water) was adjusted to pH 9–10 with a 25% NH_3 aqueous solution. Then, add 0.012 g of $N_2H_4\cdot H_2O$ to the GO suspension and keep the mixture at 90°C for 60 min. To remove the residual $N_2H_4\cdot H_2O$, the mixture was washed with a 30% H_2O_2 aqueous solution several times. The resulting mixture was neutralized until pH 7, with a 5% HCl solution. The mixture was rinsed with distilled water five times (30 mL each time). The solid, which is a graphene oxide (rGO), was collected by centrifugation and dried at 60°C for 24 h.

2.1.4. Synthesis of $CoFe_2O_4$/rGO. Add 10 mg of $CoFe_2O_4$ to 10 mL of pure ethanol and stir under the ultrasonic condition for 60 min to get a $CoFe_2O_4$ suspension (1 mg/mL). The rGO suspension was prepared in the same way as the $CoFe_2O_4$ suspension. The $CoFe_2O_4$/rGO suspension was obtained by mixing 10 mL of $CoFe_2O_4$ suspension (1 mg/mL) and 10 mL of rGO suspension (1 mg/mL) under ultrasonication for 5 h.

2.2. Apparatus. The crystal structure of the material was identified by using X-ray powder diffraction (XRD) on a Bruker D8 equipped with Cu Kα radiation ($\lambda = 1.5406$ Å). Infrared spectra were recorded on a Fourier mid-IR InfraLUM FT-08 between 4000 and 150 cm^{-1}. Scanning electron microscopy (SEM) images were recorded on an SEM JMS-5300LV (Japan), equipped with energy-dispersive X-ray microanalysis Nova Nano SEM 450. TEM images were obtained on an FEI

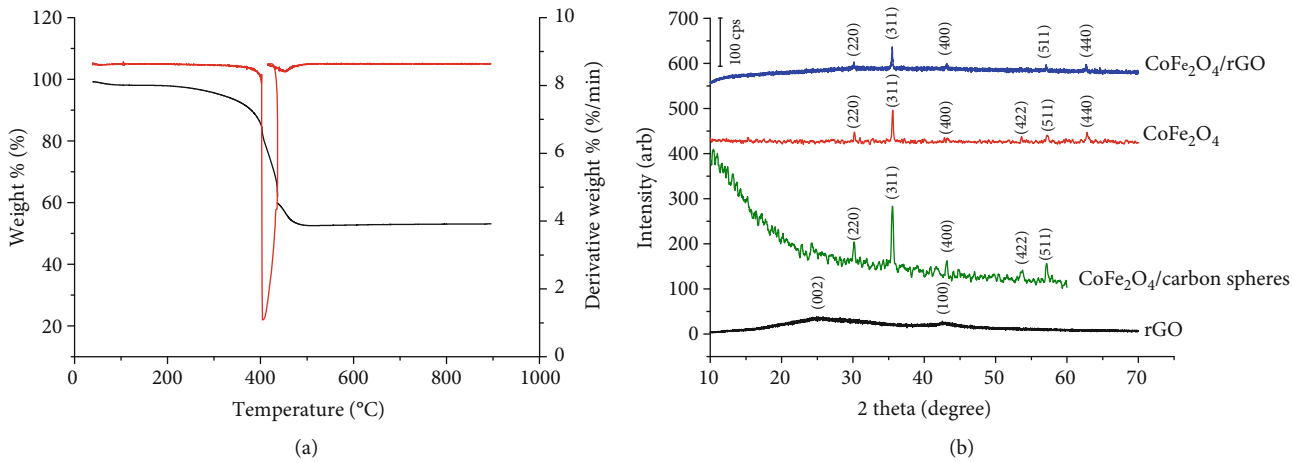

Figure 1: (a) TG/dTG diagram of $CoFe_2O_4$/carbon spheres. (b) XRD patterns of rGO, $CoFe_2O_4$/carbon spheres, $CoFe_2O_4$, and $CoFe_2O_4$/rGO.

spirit instrument (120 kV) electron microscope. The thermal properties were measured on a Micromeritics Tristar 3000 (USA). Magnetic hysteresis loops were measured on a Vibrating Sample Magnetometer (Micro Sence Easy VSM 20130321-02) at room temperature. Energy-dispersive X-ray elemental mapping (EDX-elemental mapping) was conducted on a Horiba, Japan. Ultrasonic treatment was performed in a Cole-Parmer 8890. Electrochemistry was studied by using a CPA-HH5 in which the three-electrode system consisted of a glassy carbon electrode (GCE, a working electrode), an Ag/AgCl reference electrode (Model RE-5, BAS), and a platinum wire auxiliary electrode. The UA, XA, and HX determinations with high-performance liquid chromatography (HPLC) were performed on a Shimadzu 2030 HPLC system, with a UV-Vis detector set at 273 nm. An AC18 (6.0 mm × 150 mm, 5 μm) chromatographic column was employed. The mobile phase is an acetonitrile/water mixture (25/75, v/v) at a flow rate of 1.5 mL·min^{-1}, while the injection volume was 5 mL·min^{-1}.

2.3. Analytical Procedures. The cyclic voltammetry (CV) technique was used for the preliminary studies on the electrochemical behavior of UA, XA, and HX. The differential pulse voltammetry (DPV) method was employed for the development of the electroanalytical method for the simultaneous determination of UA, XA, and HX in real samples.

Before modification, the GCE was polished with 0.05 μm alumina powder on a polishing pad, followed by sonication treatment for about two minutes in double distilled water and dried at room temperature and immediately used for modification. Two milligrams of $CoFe_2O_4$/rGO was added to 1 mL of methanol under ultrasonic agitation for 60 min, resulting in a homogeneous black suspension. Five microlitres of $CoFe_2O_4$/rGO suspension was dropped on the electrode surface. Then, the modified electrode was dried at ambient temperature to obtain a $CoFe_2O_4$/rGO glassy carbon electrode.

2.4. Real Sample Analysis. Three samples of human urine, provided by a clinical laboratory, were employed to test the method. In detail, 1.0 mL of the urine sample was spiked with UA, XA, and HX and mixed with 2 mL of the B–RBS buffer solution to make a 10.0 mL test solution. The proposed different pulse voltammetry method was used to detect UA, XA, and HX in the spiked solution.

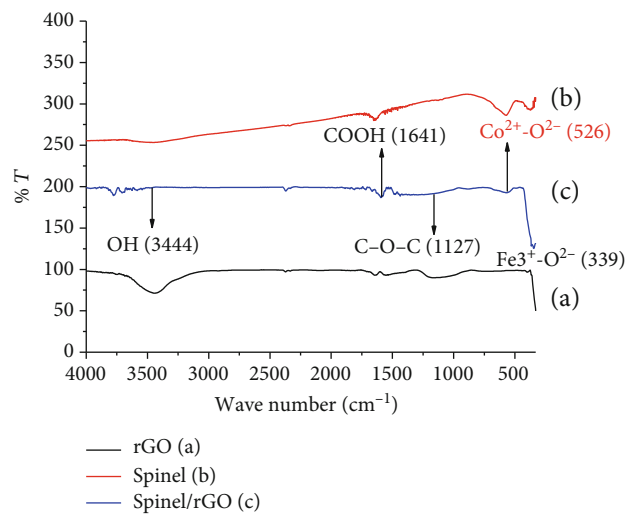

Figure 2: IR spectra of (a) rGO, (b) $CoFe_2O_4$, and (c) $CoFe_2O_4$/rGO.

3. Results and Discussion

3.1. Characterization of $CoFe_2O_4$/rGO. Figure 1(a) shows the TG/dTG curves of $CoFe_2O_4$/carbon hollow spheres recorded in airflow from 40 to 800°C. Clearly, a weight decrease of about 2 wt.% is observed from 30 to 120°C, which is ascribed to the desorption of physically adsorbed water in the precursor. Another weight loss of about 50 wt.% at around 400°C is assigned to the combustion of rGO in the $CoFe_2O_4$/rGO nanohybrid. This weight loss is close to the initial $CoFe_2O_4$/rGO ratio of 1 : 1. The carbon residues are completely removed at temperatures higher than 400°C.

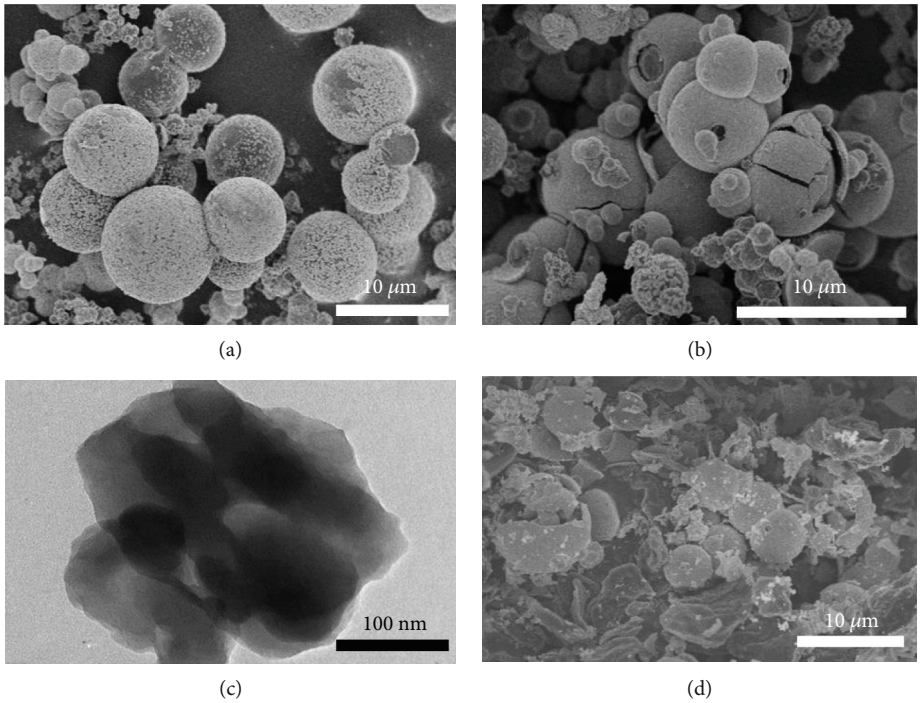

Figure 3: SEM images of (a) $CoFe_2O_4$/carbon spheres and (b) $CoFe_2O_4$. (c) TEM image of rGO. (d) SEM image of $CoFe_2O_4$/rGO.

The XRD pattern of rGO in Figure 1(b) presents a broad (002) diffraction peak between 20 and 35°, which corresponds to a short-range order in the stacked graphene sheets. The largely reduced interlayer spacing of about 0.342 nm (at 2 theta of 26°), compared with 0.780 nm (at 2 theta of 11.3°) for graphene oxide [23], indicates the formation of reduced graphene oxide, in which the oxygen functional groups are removed significantly during the reduction process. It is worth noting that the characteristic X-ray diffraction indexed as a spinel type according to JCPDS No. 00-002-1045 in $CoFe_2O_4$/carbon spheres is observed. This means that the cobalt ferrite phase is formed during the hydrothermal treatment. Cobalt ferrite with high crystallinity is formed after the removal of the carbon template through calcination at 500°C (Figure 1(b)). The characteristic peaks of the cobalt ferrite phase in $CoFe_2O_4$/rGO are observed in Figure 1(b). However, the large background indicates a large amorphous phase resulting from reduced graphene oxide. These results confirm the successful synthesis of the $CoFe_2O_4$/rGO composite.

The EDX analysis shows that the molar composition of Co, Fe, O, and C in $CoFe_2O_4$ is 13.56, 26.81, 47.18, and 12.03%, respectively, and in $CoFe_2O_4$/rGO is 4.81, 9.21, 34.52, and 51.46%, respectively. Correspondingly, the Co/Fe molar ratio is 1 : 2, which is very close to the stoichiometric ratio in the two samples. In contrast, the excessive carbon content and low Co and Fe content in $CoFe_2O_4$/rGO indicate the presence of rGO. These results further confirm the presence of stoichiometric cobalt ferrite ($CoFe_2O_4$), and this is probably assigned to the high dispersion of $CoFe_2O_4$ on the rGO surface.

The formation of the $CoFe_2O_4$/rGO composite was also studied by using FT-IR spectroscopy (Figure 2). On the FT-IR spectrum of rGO (Figure 2(a)), we can see vibration at 3444 cm^{-1} characteristic to OH groups and at 1641–1127 cm^{-1}, attributed to carbonyl (C=O) and epoxy (C–O–C) groups in rGO [24]. However, these peaks have very low intensities, implying that they are removed significantly during the reduction. The typical inverse spinel ferrite structure includes two adsorption bands: one at around 339 cm^{-1}, representing the stretching vibration of the tetragonal group Fe^{3+}–O^{2-}, and the other at around 526 cm^{-1}, attributed to the stretching vibration of the octahedral group complex Co^{2+}–O^{2-} [24] (Figure 2(b)). The characteristic vibration bands of both $CoFe_2O_4$ and rGO are observed in Figure 2(c), indicating successful synthesis of the $CoFe_2O_4$/rGO composite.

The material is formed in a hollow spherical shape (Figure 3). Figure 3(a) shows the hollow spheres (2–10 μm) with flocculent substances ($CoFe_2O_4 \cdot nH_2O$) on the carbon surface. These particles remain unaltered after removing the carbon template (Figure 3(b)). The TEM image of rGO shows a stacked and crumpled morphology due to the exfoliation and restacking process [25] (Figure 3(c)). The $CoFe_2O_4$/rGO composite consists of $CoFe_2O_4$ hollow spheres embroiled homogeneously with rGO sheets to form a hierarchical structure that favors the diffusion and adsorption of the analytes (Figure 3(d)).

The EDX elemental mapping in Figure 4(a) shows the SEM bright field image of the $CoFe_2O_4$/rGO composite. The images in Figure 4 reveal that $CoFe_2O_4$ clusters of around 500 nm in size are embedded in the rGO matrix.

The XPS survey curve presents the existence of Co, Fe, O, and C in $CoFe_2O_4$/rGO at 793.28, 721.48, 536.78, and 288.78 eV, respectively (Figure 5(a)). The XPS spectrum Co2p possesses two main peaks at 780.67 and 796.28 eV, which are assigned to Co2p3/2 and Co2p1/2, respectively (Figure 5(b)). The energy gap between the Co2p main peak

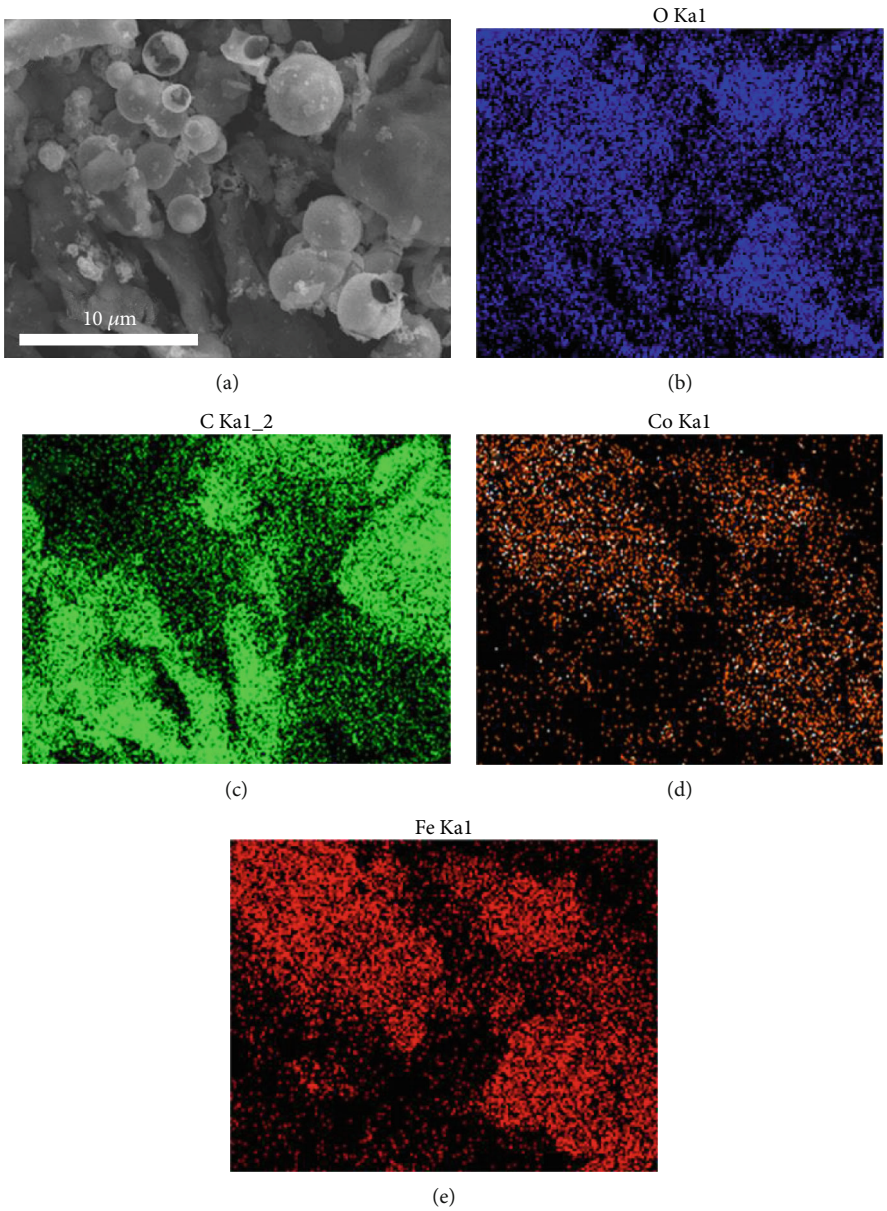

Figure 4: Elemental mapping of the $CoFe_2O_4$/rGO (a) bright field image, (b) mapping of oxygen, (c) mapping of carbon, (d) mapping of cobalt, and (e) mapping of iron.

and the satellite peak can be employed to decide whether cobalt exists as Co(II) or Co(III). If the gap is *ca.* 6.0 eV, cobalt exists as Co(II), and while the gap is 9–10 eV, the cation is Co(III) [26, 27]. In our case, the energy gap of the cobalt cation is 6.62 eV for $Co2p_{1/2}$ and 5.96 eV for $Co2p_{3/2}$, and as a result, Co(II) is the main form in $CoFe_2O_4$. The Fe2p spectrum could be deconvoluted into two main peaks at 724.35 eV for $Fe2p_{1/2}$ and 711.13 eV for $Fe2p_{3/2}$. This spectrum has two satellite peaks with a binding energy of 733.02 and 718.83 eV (Figure 5(c)), indicating the presence of Fe(III) in the sample, which is consistent with the valence of Fe in $CoFe_2O_4$ [28–30]. In Figure 5(d), the O1s peak is deconvoluted into two shoulder peaks at 532.56 eV and 530.46 eV, corresponding to the hydroxyl groups adsorbed on the surface and the Fe–O bond in the crystal lattice, respectively [31]. The C1s spectrum could be fitted to four carbon species at 284.58, 285.55, 286.9, and 289.46 eV, corresponding to C/C=C groups in the nonoxygenated rings, C–OH, epoxy C–O–C, and carboxyl group COOH, respectively (Figure 5(e)) [32].

The magnetic hysteresis curves of the $CoFe_2O_4$ and $CoFe_2O_4$/rGO composite, measured at 298 K with the field sweeping from −10000 to 10000 Oe, indicate that the two materials are ferromagnetic (Figure 6). The saturation magnetization is 60.2 emu·g^{-1} for $CoFe_2O_4$ and 48.6 emu·g^{-1} for $CoFe_2O_4$/rGO. These values are slightly higher than those of other cobalt-ferrite-based materials, reported previously [32–34].

The specific surface area and pore volume of the materials were determined by using the nitrogen sorption

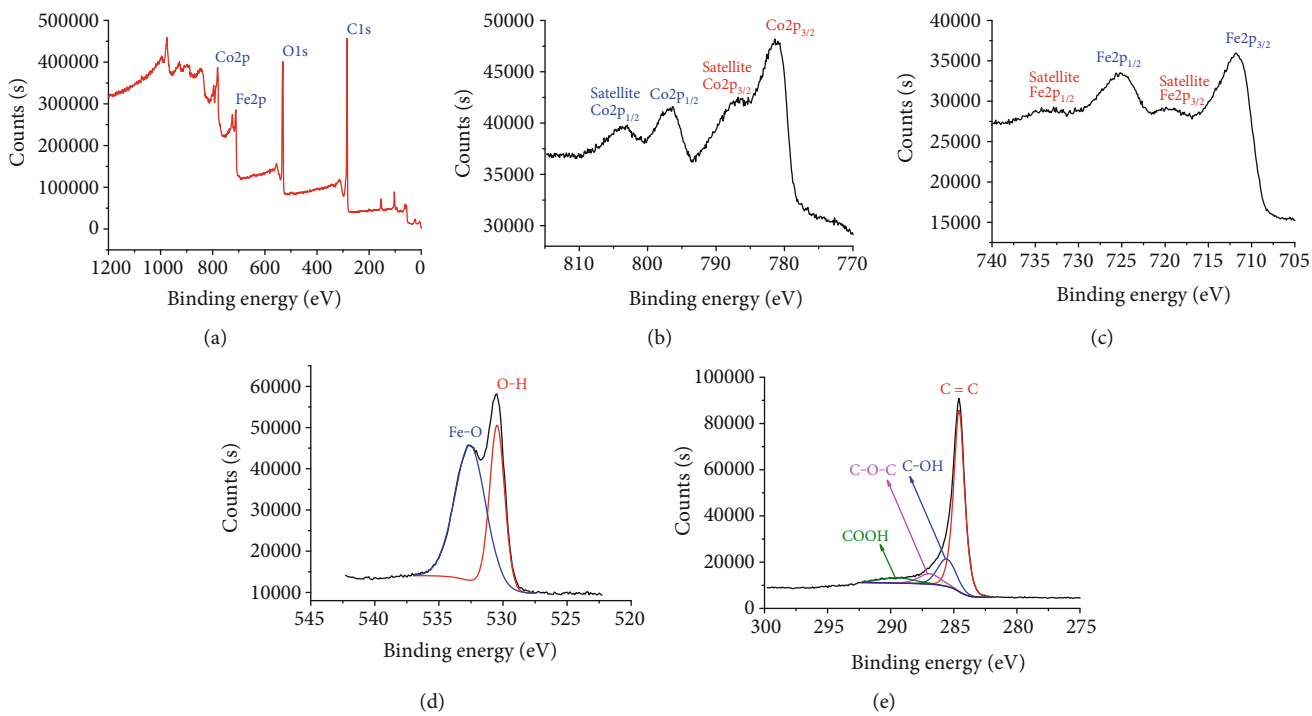

Figure 5: XPS spectrum of $CoFe_2O_4$/rGO: (a) survey spectrum; (b) XPS spectrum Co2p; (c) XPS spectrum Fe2p; (d) XPS spectrum O1s; (e) XPS spectrum C1s.

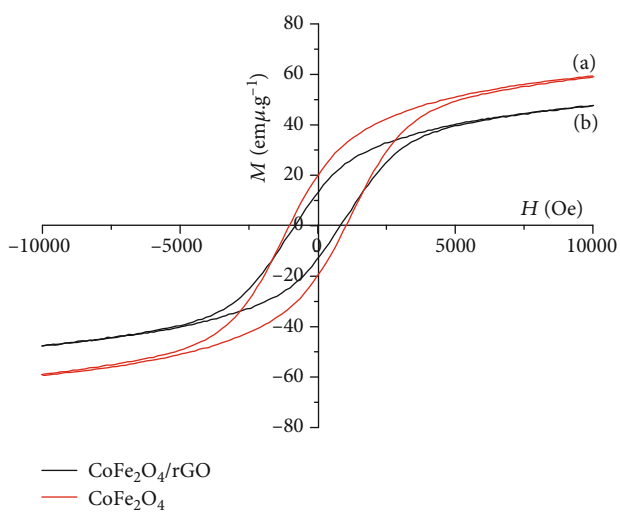

Figure 6: Magnetic saturation curves of (a) $CoFe_2O_4$ and (b) $CoFe_2O_4$/rGO.

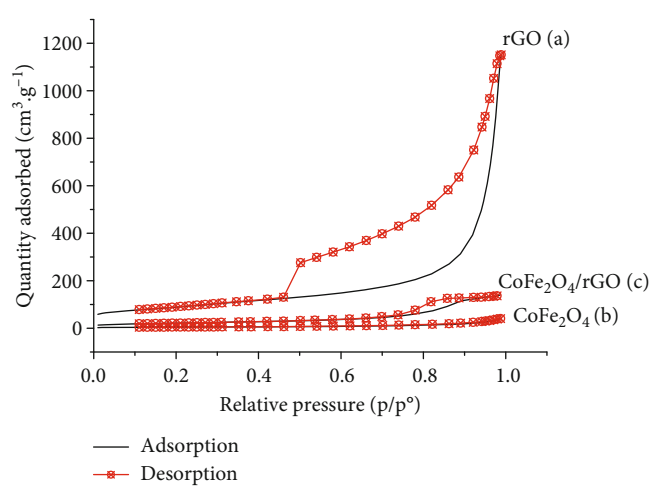

Figure 7: Nitrogen adsorption/desorption of (a) rGO, (b) $CoFe_2O_4$, and (c) $CoFe_2O_4$/rGO.

technique, with a typical isotherm shown in Figure 7. The isotherms of rGO, $CoFe_2O_4$, and $CoFe_2O_4$/rGO exhibit type IV with hysteresis loops at high relative pressures. This indicates the presence of interparticle and nonordered mesoporosity in the materials. The BET surface area is $319\,m^2{\cdot}g^{-1}$ for rGO, $16\,m^2{\cdot}g^{-1}$ for $CoFe_2O_4$, and $77\,m^2{\cdot}g^{-1}$ for $CoFe_2O_4$/rGO. The surface area of the $CoFe_2O_4$/rGO composite is nearly fivefold compared with that of pure $CoFe_2O_4$. These findings indicate that cobalt ferrite particles are highly dispersed on the rGO matrix, and the material possesses a large surface area.

3.2. Electrochemical Performance of $CoFe_2O_4$/rGO-Modified Electrode

3.2.1. Voltammetric Behavior of Different Electrodes. As seen in Figure 8, all electrodes provide an anodic peak current (I_a) for the analytes, and the highest peak current with low standard deviation is observed on $CoFe_2O_4$-rGO/GCE for all the analytes.

The $CoFe_2O_4$-rGO/GCE is favorable for electron transfer and oxidation. Therefore, this modified electrode was selected for further experiments.

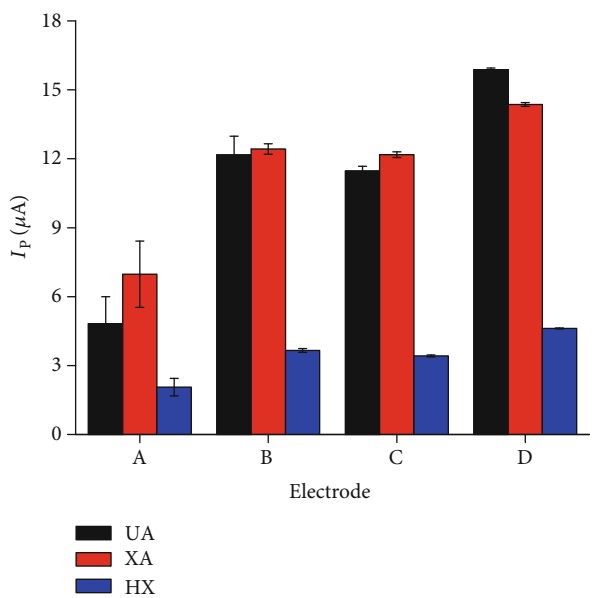

Figure 8: Anodic peak current (I_p) of UA, XA, and HX at bare GCE (A), $CoFe_2O_4$/GCE (B), rGO/GCE (C), and $CoFe_2O_4$-rGO/GCE (D). Conditions: $E_{acc} = -0.3$ V, $t_{acc} = 20$ s, $\Delta E = 120$ mV, and $v = 20$ mV · s^{-1} ($C_{UA} = C_{XA} = C_{HX} = 2 \times 10^{-5}$ M; 0.2 M PBS pH 7, $n = 4$).

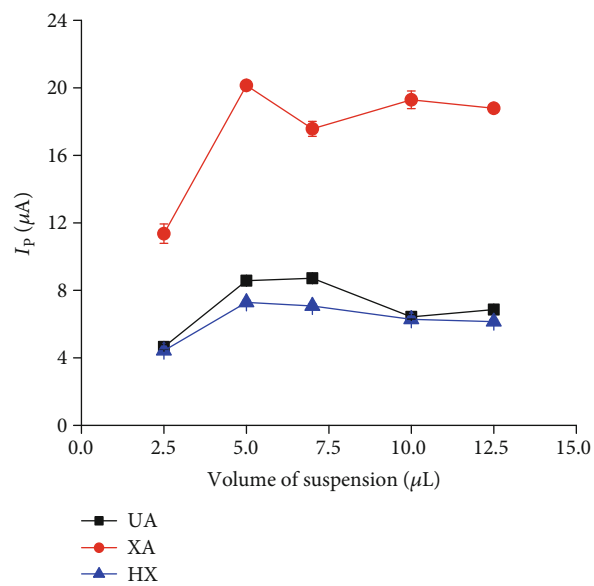

Figure 9: Effects of the amount of $CoFe_2O_4$/rGO on the GCE on the anodic peak currents (I_p) of $C_{UA} = C_{XA} = C_{HX} = 2 \times 10^{-5}$ M in 0.2 M B–RBS pH 7. Other conditions are as in Figure 8.

3.2.2. Effect of Amount of Electrode Modifier. The amount of $CoFe_2O_4$/rGO on the electrode surface is related to the thickness of the cast film and responsible for the total specific surface area. Therefore, this amount affects the adsorption of UA, XA, and HX on the electrode surface and, thus, the anodic peak current of UA, XA, and HX. To study this effect, we changed the volume of the $CoFe_2O_4$/rGO suspension (1.0 mg·mL^{-1}) during the measurements. At the beginning of the volume range, the I_a increases with the volume of the $CoFe_2O_4$/rGO suspension, owing to the increasing amount of UA, XA, and HX adsorbed on the modified electrode surface. Later, the I_a changes slightly when the volume of the $CoFe_2O_4$/rGO suspension exceeds 5 μL, indicating an insignificant influence of the film thickness on the adsorption of the analytes (Figure 9). This also suggests a rapid electron transfer within the $CoFe_2O_4$/rGO film. However, when the volume of the $CoFe_2O_4$/rGO suspension is greater than 7.5 μL, the I_a tends to decrease due to larger film thickness and the increasing mass transfer resistance against the electron transfer. In this work, the amount of $CoFe_2O_4$/rGO suspension on the GCE surface was selected at 5 μL.

3.2.3. . Effects of pH. The pH of the solution has a remarkable influence on the UA, XA, and HX electrooxidation on the $CoFe_2O_4$/rGO-GCE. Figure 10(a) illustrates the DPV curves of UA, XA, and HX on the modified electrode in the pH range of 2–10. As shown in Figure 10(b), when the pH of the solution is lower than 4, the I_a of all analytes decreases with pH. At a pH higher than 6, only the I_a of XA increases with pH and reaches a maximum at pH 6. However, the I_a of UA and HX tends to reduce until pH reaches 7. Afterward, they change irregularly as pH increases. The dependence of the peak current of UA, XA, and HX on pH is complicated, but a decreasing tendency is observed with all the analytes (Figure 10(b)). This may result from the adsorption behavior of UA, XA, and HX on the $CoFe_2O_4$/rGO-GCE. UA, XA, and HX are known as protic aromatic molecules and can become deprotonated to form negatively charged species (anions) at higher pH. Simultaneously, the surface of $CoFe_2O_4$/rGO-GCE also becomes negatively charged at high pH. As a result, less intensive adsorption of the analytes on the electrode might take place, thus reducing the I_a.

The pH effects on peak potentials (E_p) for UA, XA, and HX oxidations on the $CoFe_2O_4$/rGO-GCE were also studied. The E_p values shift to more negative potential with pH, and the plots of E_p vs. pH exhibit high linearity with high determination coefficients (>0.99) (Figure 10(c)). The regression equations are expressed as follows:

$$\begin{aligned}
\text{UA}: E_{p,UA} &= (0.607 \pm 0.010) + (-0.061 \pm 0.001) \times \text{pH}, \\
&\quad r = 0.9978. \\
\text{XA}: E_{p,XA} &= (0.976 \pm 0.010) + (-0.056 \pm 0.001) \times \text{pH}, \\
&\quad r = 0.9976. \\
\text{HX}: E_{p,HX} &= (1.346 \pm 0.012) + (-0.060 \pm 0.002) \times \text{pH}, \\
&\quad r = 0.9970.
\end{aligned} \tag{1}$$

The slopes of the lines are −0.061, −0.056, and −0.060 for UA, XA, and HX, respectively, and they are close to the theoretical slope of −0.0599 V/pH. This indicates that the oxidation of UA, XA, and HX involves an equal number of electrons and protons.

3.2.4. Effects of Scan Rate. The effect of the scan rate on electrochemical signals of UA, XA, and HX was also assessed by

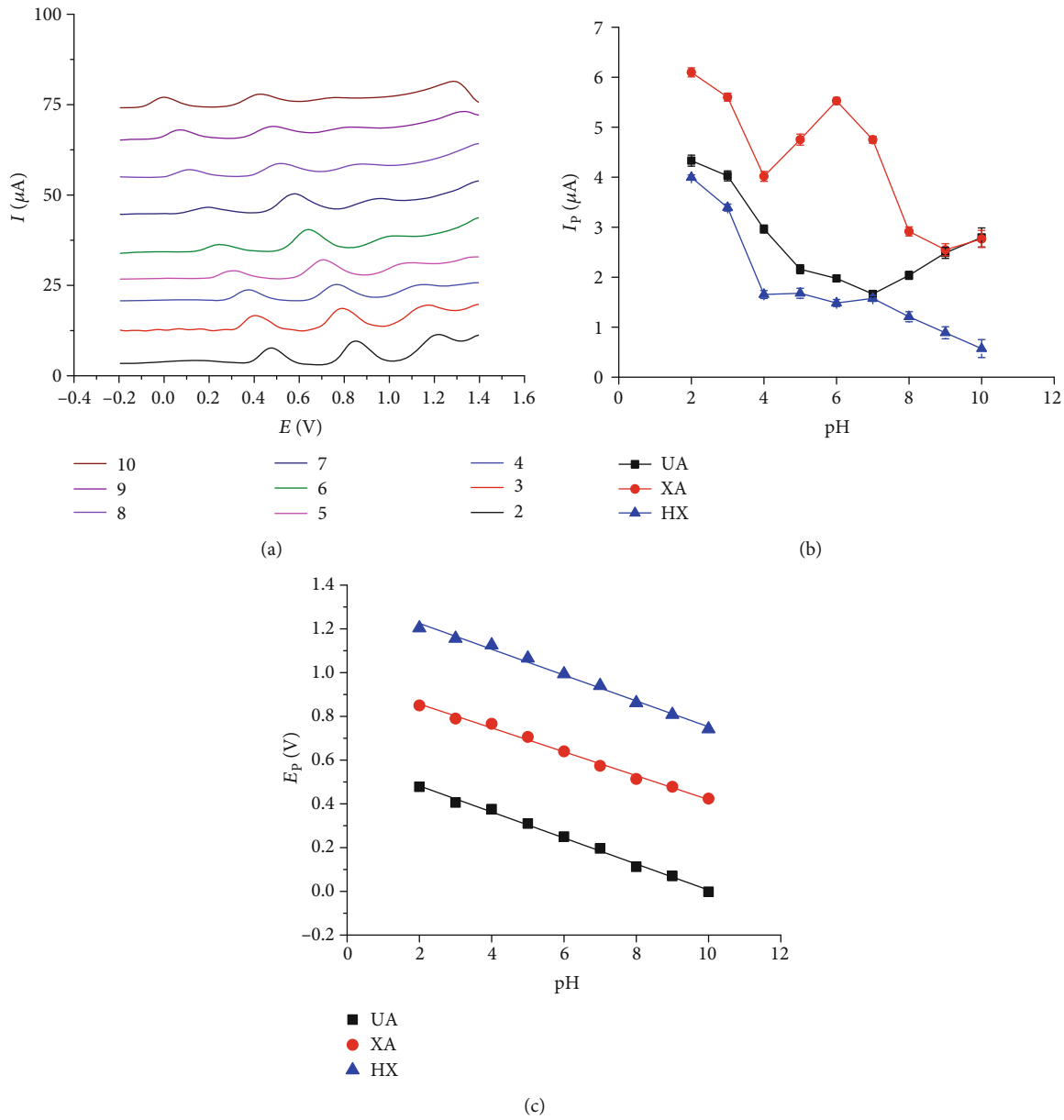

Figure 10: (a) DPV curves of UA, XA, and HX oxidations on the modified electrode at different pH. (b) Effects of pH on the anodic peak currents (I_p). (c) The linear plot of anodic peak current (I_p) vs. pH ($C_{UA} = C_{XA} = C_{HX} = 2 \times 10^{-5}$ M in 0.2 M B–RBS). Other conditions are as in Figure 8.

changing the scan rate from 50 to 500 mV·s^{-1} (Figure 11). Figure 11(a) presents the scan rate effect of electrochemical responses studied with the CV method. The linear plot of the peak current vs. the square root of the scan rate was conducted to estimate whether the electrooxidation reaction is controlled by diffusion or adsorption. If the plot of I_p vs. $v^{1/2}$ passes the origin, this process is controlled by diffusion; otherwise, it is controlled by adsorption [35, 36]. The plots of $I_{p,UA}$, $I_{p,XA}$, and $I_{p,HX}$ vs. $v^{1/2}$ are highly linear ($r = 0.9588 \div 0.9866$, $p < 0.001$) (Figure 11(b)). The number in the parentheses presents the 95% confidence interval. No lines pass the origin because all the intercepts are greater than zero (varying from 0.690 to 6.770 for UA, 10.913 to 16.767 for XA, and 1.799 to 7.843 for HX at 95% confidence—Equations (2), (3), and (4)). This indicates that the electrode process is controlled by adsorption.

$$I_{p,UA} = (3.730 \pm 3.040) + (1.276 \pm 0.189) \times v^{1/2}, \quad r = 0.9588, \tag{2}$$

$$I_{p,XA} = (13.840 \pm 2.927) + (2.182 \pm 0.182) \times v^{1/2}, \quad r = 0.9863, \tag{3}$$

$$I_{p,HX} = (4.771 \pm 3.072) + (1.435 \pm 0.191) \times v^{1/2}, \quad r = 0.9663. \tag{4}$$

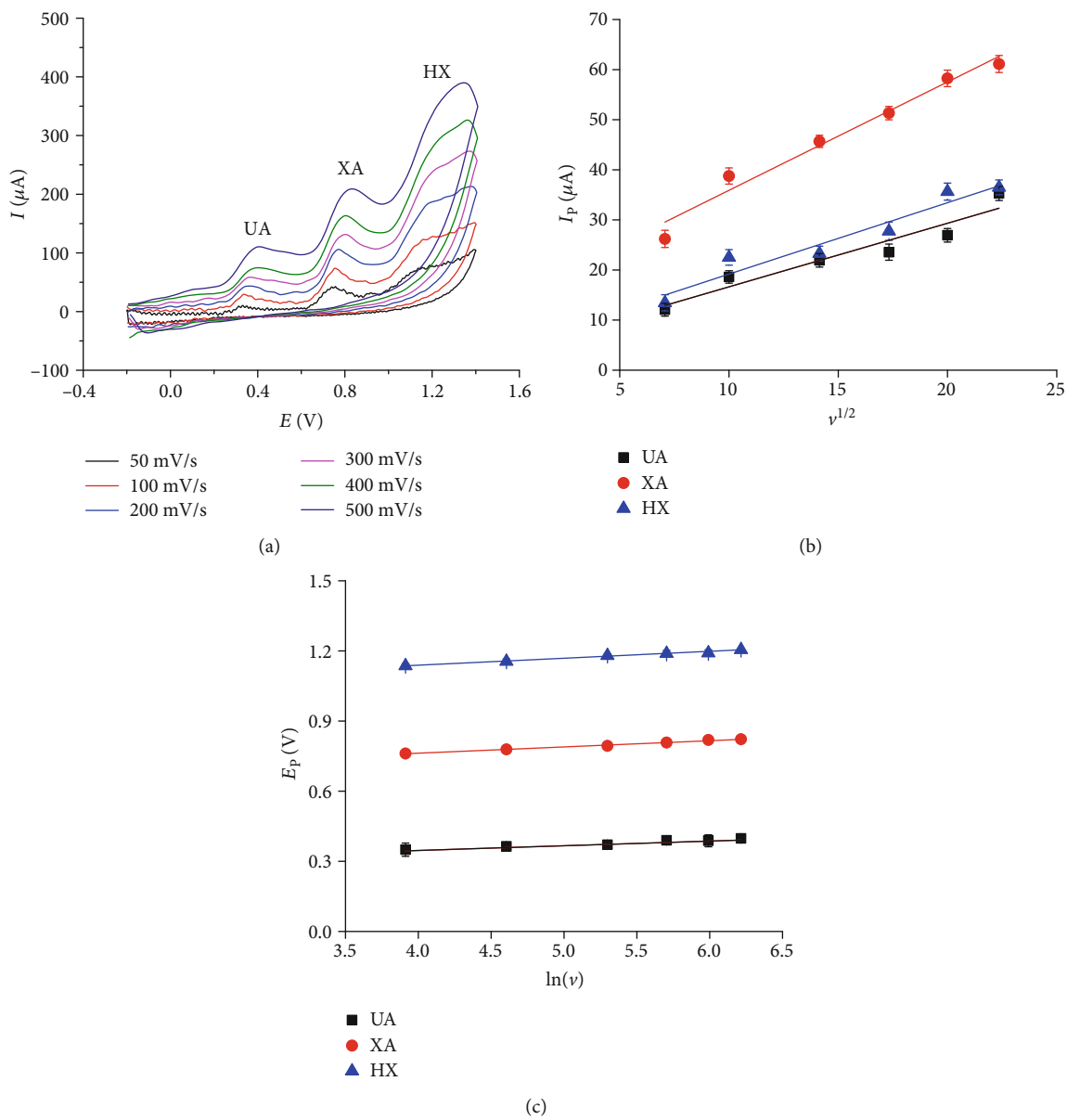

Figure 11: (a) DPV curves of UA, XA, and HX oxidations at the $CoFe_2O_4$/rGO-GCE. (b) The plot of anodic peak current (I_a) vs. $v^{1/2}$. (c) The plot of anodic peak potential (E_a) vs. ln (v). Conditions: $E_{acc} = -0.3$ V, $t_{acc} = 20$ s, $E_{range} = -0.0 \div +1.4$ V ($C_{UA} = C_{XA} = 5 \times 10^{-4}$ M and $C_{HX} = 10^{-3}$ M in 0.2 M B–RBS pH 5).

The relationship of the anodic potential vs. the natural logarithm of the scan rate is expressed by the Laviron equation [37].

$$E_p = E^\circ - \frac{R \times T}{(1-\alpha) \times n \times F} \ln \frac{R \times T \times K_s}{(1-\alpha) \times n \times F} + \frac{R \times T}{(1-\alpha) \times n \times F} \times \ln(v), \quad (5)$$

where K_s is the electron rate constant of the surface-confined redox couple, n is the number of electrons transferred, α is the charge transfer coefficient, v is the scan rate ($V \cdot s^{-1}$), E° is the formal redox potential, $T = 298$ K, $R = 8.314\ J \cdot mol \cdot K^{-1}$, and $F = 96480\ C \cdot mol^{-1}$.

The plots of the anodic peak potential vs. the natural logarithm of the scan rate are presented in Figure 11(c). The regression equation is expressed in Equations (6)–(8).

$$E_{p,UA} = (0.270 \pm 0.012) + (0.021 \pm 0.002) \times \ln(v), \quad r = 0.977 \quad (6)$$

$$E_{p,XA} = (0.654 \pm 0.006) + (0.027 \pm 0.001) \times \ln(v), \quad r = 0.996, \quad (7)$$

$$E_{p,HX} = (0.994 \pm 0.019) + (0.030 \pm 0.004) \times \ln(v), \quad r = 0.978. \quad (8)$$

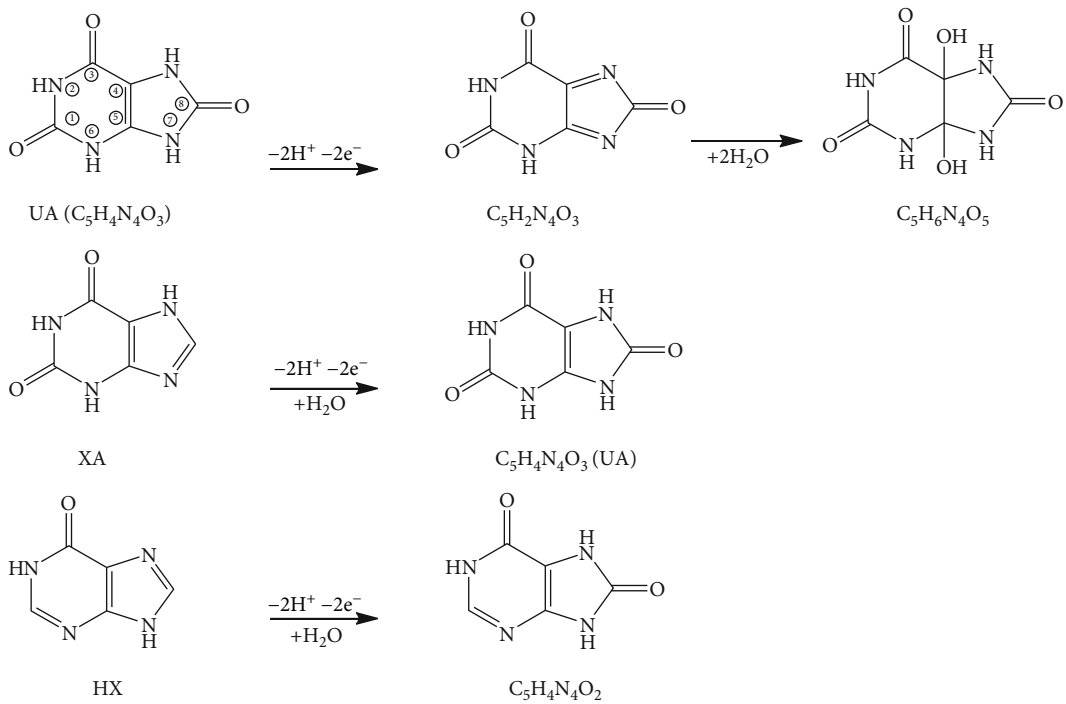

Scheme 1: Proposed mechanism for the oxidation of UA, XA, and HX.

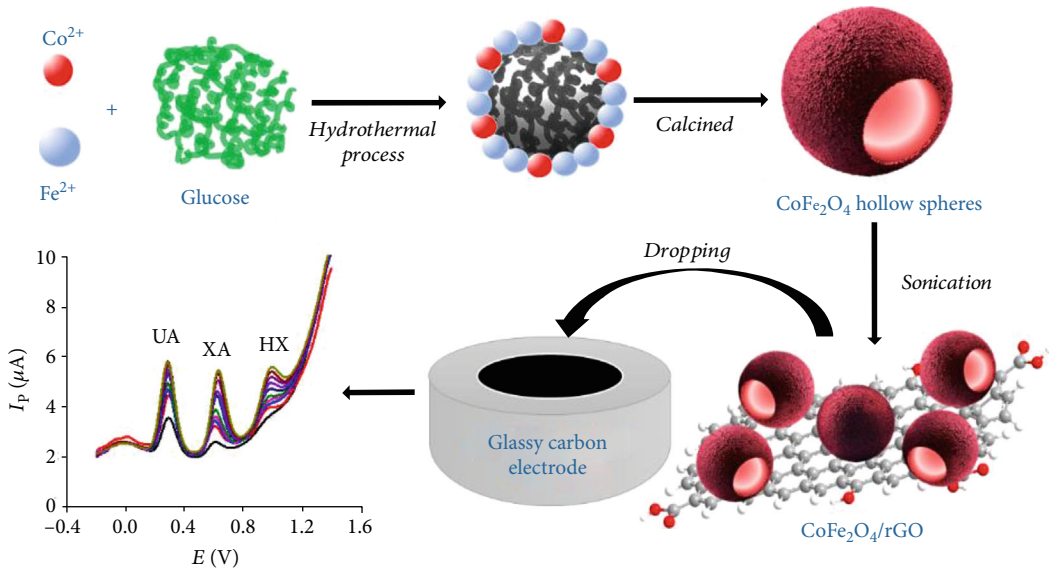

Scheme 2: Proposed mechanism for the electrode process of UA, XA, and HX oxidations.

The values of $n \times \alpha$ for UA, XA, and HX are 1.222, 0.950, and 0.856, respectively. For the irreversible system, α is assumed to be 0.5 [38]. Therefore, the average values of n are 2.444, 1.900, and 1.912. Because the number of electrons transferred is an integer, this number should be 2 in this case for all analytes. Therefore, the oxidation of UA, XA, and HX involves two electrons and two protons. This is consistent with previous work [8]. The mechanism for the oxidation of the analytes is proposed in Scheme 1.

The $CoFe_2O_4$/rGO film possesses a large number of negatively charged surface functional groups (–OH) and electron-rich oxygen atoms (epoxide, OH, C=O), and they could interact with the purine derivatives (in this case, they are UA, XA, and HX). Furthermore, the $CoFe_2O_4$/rGO-modified electrode exhibits a larger real surface, π-π conjugated bonds, an abundant number of active sites, and better electronic conductivity, which leads to a strong interaction between the purine derivatives and the electrode interface. Therefore, the electrochemical oxidation of UA, XA, and HX may be substantially accelerated in the presence of the $CoFe_2O_4$/rGO film. This might result from the enhanced rate of electron transfer and electrocatalytic activity towards

Table 1: Tolerance limit of interfering species at $C_{UA} = C_{XN} = C_{HX} = 10^{-5}$ M in 0.2 M PBS pH 5.

Interferent	Interferent/analyte molar ratio	UA		XA		HX	
		I_p (μA)	RE (%)	I_p (μA)	RE (%)	I_p (μA)	RE (%)
Paracetamol	10 : 1	4.25	17.49	3.68	−5.00	1.96	−1.23
Ascorbic acid	50 : 1	4.81	28.05	3.75	−7.57	2.03	−4.86
D-Glucose	1000 : 1	3.40	−1.92	3.65	0.06	1.96	−1.11
KCl	20 : 1	1.429	2.15	4.574	1.64	2.60	0.902
Na_2CO_3	20 : 1	0.562	−5.23	3.66	2.52	2.262	4.31
$MgSO_4$	100 : 1	0.620	−1.27	3.530	−3.29	2.085	−5.51

Table 2: Mean values of I_p, RSD, and RSD_H.

	C (M)	$I_{p,average}$ (μA)	SD	RSD (%)	$1/2 \times RSD_H$ (%)
EPX 1	$C_{UA} = 10^{-5}$	1.968	0.04	2.17	5.66
	$C_{XA} = 10^{-5}$	0.918	0.02	2.04	5.66
	$C_{HX} = 10^{-5}$	0.381	0.01	2.33	5.66
EPX 2	$C_{UA} = 5 \times 10^{-5}$	3.299	0.05	1.49	4.44
	$C_{XA} = 5 \times 10^{-5}$	2.788	0.03	1.18	4.44
	$C_{HX} = 5 \times 10^{-5}$	1.338	0.01	1.05	4.44
EPX 3	$C_{UA} = 10^{-4}$	2.604	0.06	2.29	4.00
	$C_{XA} = 10^{-4}$	3.423	0.04	1.11	4.00
	$C_{HX} = 10^{-4}$	1.718	0.03	1.50	4.00

SD: standard deviation; RSD: relative standard deviation. B–RBS pH = 5; $n = 4$.

the oxidation of UA, XA, and HX. The argument is illustrated in Scheme 2.

3.2.5. Interferent Study. For evaluating the selectivity of the modified electrode, several possible interferents were evaluated for their behavior in the determination of UA, XA, and HX (equal concentration of 2.0×10^{-5} mol · L^{-1}). The tolerance limit is the maximum concentration of a foreign substance that causes an approximately ±5% relative error in the determination. It is found that 10-fold of paracetamol and 50-fold of ascorbic acid do not interfere with the peak current of XA and HX but significantly affect that of UA. However, 1000-fold of *D*-glucose, 20-fold of KCl and Na_2CO_3, and 100-fold of $MgSO_4$ do not interfere with the determination of UA, XA, and HX (Table 1). These findings indicate that the present method can be used for real samples.

3.2.6. Repeatability, Linear Range, and Limit of Detection. The repeatability of I_p at the $CoFe_2O_4$/rGO-GCE was estimated by comparing the relative standard deviation (RSD) with the relative standard deviation calculated from Horwitz's equation: $RSD_H = 2^{1-0.5\times\lg C}$, where C is the concentration in mole fraction. If the RSD is less than $1/2 \times RSD_H$, the repeatability is acceptable [39]. Each signal of I_p was obtained by conducting a series of four successive measurements at three concentrations. Table 2 displays the values of RSD and the $1/2 \times RSD_H$ predicted, and we can see that all the measurements are repeatable. Therefore, the $CoFe_2O_4$/rGO-GCE can be used repeatedly for the detection of UA, XA, and HX at low or high concentrations.

Under optimum conditions, the peak current in stripping voltammetry exhibits two linear ranges: 2 μM to 10 μM (P1) and 10 μM to 35 μM (P2) (Figure 12). The linear regression equations are as follows:

$$\begin{aligned}
\text{UA}: I_{p1,\text{UA}} &= (1.301 \pm 0.039) + (0.145 \pm 0.006) \times C_{\text{UA}}, \\
r &= 0.9976, \\
I_{p2,\text{UA}} &= (2.387 \pm 0.055) + (0.038 \pm 0.002) \times C_{\text{UA}}, \\
r &= 0.9928. \\
\text{XA}::I_{p1,\text{XA}} &= (0.277 \pm 0.029) + (0.126 \pm 0.004) \times C_{\text{XA}}, \\
r &= 0.9982, \\
I_{p2,\text{XA}} &= (1.017 \pm 0.074) + (0.059 \pm 0.003) \times C_{\text{XA}}, \\
r &= 0.9945. \\
\text{HX}::I_{p1,\text{HX}} &= (0.119 \pm 0.008) + (0.044 \pm 0.001) \times C_{\text{HX}}, \\
r &= 0.9989, \\
I_{p2,\text{HX}} &= (0.270 \pm 0.025) + (0.031 \pm 0.0001) \times C_{\text{HX}}, \\
r &= 0.9976.
\end{aligned} \tag{9}$$

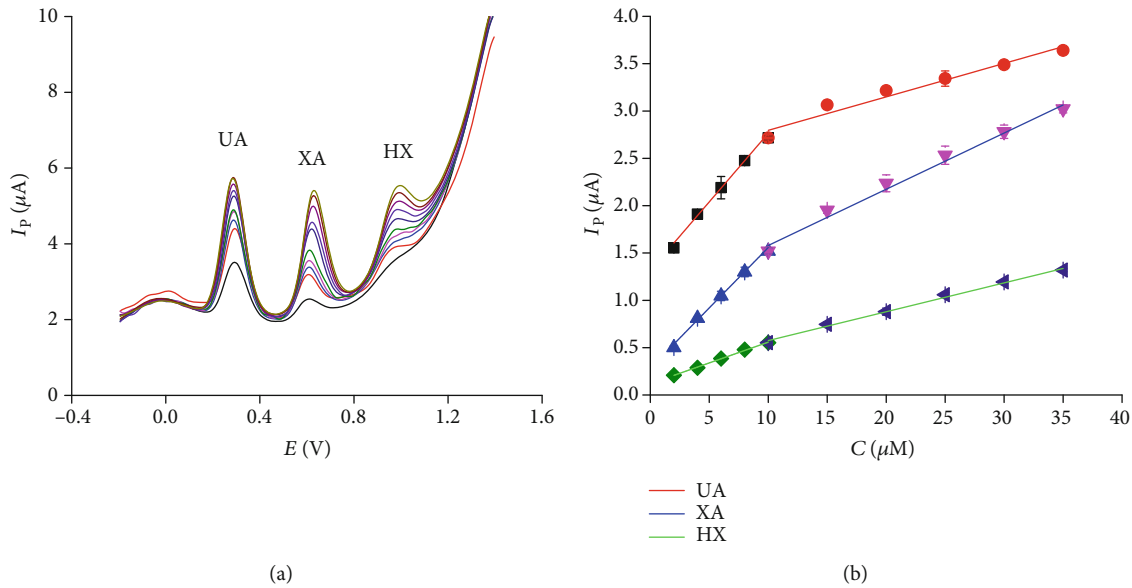

Figure 12: (a) DPV curves for UA, XA, and HX with different concentrations in B–RBS 0.2 M pH 5. (b) The plot of I_a vs. concentration. Other conditions are as in Figure 8.

Table 3: Comparison of the proposed method with other electrochemical approaches for the simultaneous determination of UA, XA, and HX.

Electrode modifier	Analytes	Linear range (μM)	LOD (μM)	References
	UA	100–700	0.372	
Ru $(DMSO)_4Cl_2$ nanoaggregated Nafion	XA	50–500	2.35	[7]
	HX	50–300	2.37	
	UA	2.0–40	0.42	
Preanodized nontronite	XA	2.0–40	0.07	[6]
	HX	4.0–30	0.34	
	UA	0.5–120	0.20	
Poly(bromocresol purple)	XA	0.1–100	0.06	[8]
	HX	20–80	0.12	
	UA	0.1–10	0.05	
Poly-(L-arginine)/graphene composite	XA	0.1–10	0.05	[41]
	HX	0.2–20	0.1	
	UA	10–500	10	
Pyrolytic graphite	XA	10–500	10	[42]
	HX	10–500	10	
	UA	2–10	0.767	The present work
$CoFe_2O_4$/rGO	XA	2–10	0.650	The present work
	HX	2–10	0.506	The present work

Limit of detection (LOD) is calculated using the formula [40]

$$\mathrm{LOD} = \frac{3S}{b}, \tag{10}$$

where S is the standard deviation of the lowest concentration of UA, XN, and HP and b is the slope of calibration curve obtained from the DPV. The detection limits of UA, XA, and HX obtained in the first range are 0.767, 0.650, and 0.506 μM, respectively. A comparison of the proposed method with other electrochemical approaches for UA, XA, and HX is presented in Table 3. It is notable that the LOD of UA, XA, and HX from the proposed methods is compatible with those based on the modified electrodes reported previously. From the analysis above, we can conclude that $CoFe_2O_4$/rGO is a potential electrode modifier for determining UA, XA, and HX.

Table 4: Determination of UA, XA, and HX in human urine sample.

Samples	Analyte	Detected (mM) Ave ± SD ($n = 4$)	Added (mM)	Found (mM) Ave ± SD ($n = 4$)	Rev (%)	Detected by HPLC (mM)
Urine 01	UA	4.31 ± 0.47	1.50	5.820 ± 0.270	101.0	4.250
	XA	0.106 ± 0.004	0.045	0.149 ± 0.016	95.4	0.111
	HX	<LOD	n/a	n/a	n/a	n/a
Urine 02	UA	1.990 ± 0.170	1.500	3.440 ± 0.30	96.4	2.180
	XA	0.059 ± 0.009	0.045	0.105 ± 0.015	101.9	0.077
	HX	<LOD	0.750	0.786 ± 0.042	104.8	n/a
Urine 03	UA	5.57 ± 0.08	1.500	7.15 ± 0.75	105.3	5.390
	XA	0.007 ± 0.001	0.045	0.053 ± 0.003	101.3	0.012
	HX	<LOD	0.750	0.712 ± 0.037	95.0	n/a

n/a: not applicable; Ave: average value; SD: standard deviation; n: the number of repetitions of experiments.

3.2.7. Determination of Purine Derivatives in Human Samples. The proposed DPV method was applied to determining the human purine derivatives. The standard addition technique was employed. The recovery experiments were conducted with human urine samples using the $CoFe_2O_4$/rGO-CGE, and the findings are listed in Table 4. The recoveries found in the range of 95%–105.3% indicate the accuracy and efficiency of the proposed method for the urine samples. The results obtained with HPLC for the real samples are given for comparison. The results from HPLC are comparable with those obtained from the DPV method proposed in this paper (paired sample t-test: $\alpha = 0.05$, $t(5) = 0.5$, $p = 0.637 > 0.05$).

4. Conclusions

In this paper, the $CoFe_2O_4$/rGO-GCE is fabricated by using a simple method and employed as an electrochemical sensor for the simultaneous detection of UA, XA, and HX with the differential pulse voltammetry technique. The modified electrode has good stability and sensitivity. The results obtained with the proposed method are consistent with those from standard HPLC analysis. Therefore, $CoFe_2O_4$/rGO is expected to become a potential tool for the assay of UA, XA, and HX both in research and in clinical diagnosis owing to its good precision, high speed, and low cost of analysis.

Data Availability

The data used to support the findings of this study are available from the corresponding author upon request.

Conflicts of Interest

The authors declare that they have no conflicts of interest.

Acknowledgments

The authors are thankful for the financial support from the Vietnamese Ministry of Education and Training for the development of the basic sciences in the fields of chemistry, science of life, science of earth, and science of sea from 2017 to 2025 (Code No. B2019-DQN-562-03).

References

[1] T. Yamamoto, Y. Moriwaki, and S. Takahashi, "Effect of ethanol on metabolism of purine bases (hypoxanthine, xanthine, and uric acid)," *Clinica Chimica Acta*, vol. 356, no. 1-2, pp. 35–57, 2005.

[2] E. Caussé, A. Pradelles, B. Dirat, A. Negre-Salvayre, R. Salvayre, and F. Couderc, "Simultaneous determination of allantoin, hypoxanthine, xanthine, and uric acid in serum/-plasma by CE," *Electrophoresis*, vol. 28, no. 3, pp. 381–387, 2007.

[3] J. R. Klinenberg, S. Goldfinger, K. H. Bradley, and J. E. Seegmiller, "An enzymatic spectrophotometric method for the determination of xanthine and hypoxanthine," *Clinical Chemistry*, vol. 13, no. 10, pp. 834–846, 1967.

[4] R. Boulieu, C. Bory, P. Baltassat, and C. Gonnet, "High-performance liquid chromatographic determination of hypoxanthine and xanthine in biological fluids," *Journal of Chromatography B: Biomedical Sciences and Applications*, vol. 233, no. 1, pp. 131–140, 1982.

[5] N. Cooper, R. Khosravan, C. Erdmann, J. Fiene, and J. W. Lee, "Quantification of uric acid, xanthine and hypoxanthine in human serum by HPLC for pharmacodynamic studies," *Journal of Chromatography B*, vol. 837, no. 1-2, pp. 1–10, 2006.

[6] J.-M. Zen, Y.-Y. Lai, H.-H. Yang, and A. S. Kumar, "Multianalyte sensor for the simultaneous determination of hypoxanthine, xanthine and uric acid based on a preanodized nontronite-coated screen-printed electrode," *Sensors and Actuators B: Chemical*, vol. 84, no. 2-3, pp. 237–244, 2002.

[7] A. S. Kumar and P. Swetha, "$Ru(DMSO)_4Cl_2$ nano-aggregated Nafion membrane modified electrode for simultaneous electrochemical detection of hypoxanthine, xanthine and uric acid," *Journal of Electroanalytical Chemistry*, vol. 642, no. 2, pp. 135–142, 2010.

[8] Y. Wang and L.-l. Tong, "Electrochemical sensor for simultaneous determination of uric acid, xanthine and hypoxanthine based on poly (bromocresol purple) modified glassy carbon electrode," *Sensors and Actuators B: Chemical*, vol. 150, no. 1, pp. 43–49, 2010.

[9] F. Zhang, Z. Wang, Y. Zhang et al., "Simultaneous electrochemical determination of uric acid, xanthine and hypoxanthine based on poly(l-arginine)/graphene composite film modified electrode," *Talanta*, vol. 93, pp. 320–325, 2012.

[10] G. El-Shobaky, A. Turky, N. Mostafa, and S. Mohamed, "Effect of preparation conditions on physicochemical, surface and catalytic properties of cobalt ferrite prepared by coprecipitation," *Journal of Alloys and Compounds*, vol. 493, no. 1-2, pp. 415–422, 2010.

[11] I. Sandu, L. Presmanes, P. Alphonse, and P. Tailhades, "Nanostructured cobalt manganese ferrite thin films for gas sensor application," *Thin Solid Films*, vol. 495, no. 1-2, pp. 130–133, 2006.

[12] V. A. Kumary, J. Divya, T. M. Nancy, and K. Sreevalsan, "Voltammetric detection of paracetamol at cobalt ferrite nanoparticles modified glassy carbon electrode," *International Journal of Electrochemical Science*, vol. 8, pp. 6610–6619, 2013.

[13] J.-T. Han, K.-J. Huang, J. Li, Y.-M. Liu, and M. Yu, "β-Cyclodextrin-cobalt ferrite nanocomposite as enhanced sensing platform for catechol determination," *Colloids and Surfaces B: Biointerfaces*, vol. 98, pp. 58–62, 2012.

[14] F. S. Yardımcı, M. Şenel, and A. Baykal, "Amperometric hydrogen peroxide biosensor based on cobalt ferrite-chitosan nanocomposite," *Materials Science and Engineering: C*, vol. 32, no. 2, pp. 269–275, 2012.

[15] A. A. Ensafi, H. A. Alinajafi, M. Jafari-Asl, B. Rezaei, and F. Ghazaei, "Cobalt ferrite nanoparticles decorated on exfoliated graphene oxide, application for amperometric determination of NADH and H_2O_2," *Materials Science and Engineering: C*, vol. 60, pp. 276–284, 2016.

[16] Z.-S. Wu, W. Ren, L. Gao et al., "Synthesis of graphene sheets with high electrical conductivity and good thermal stability by hydrogen arc discharge exfoliation," *ACS Nano*, vol. 3, no. 2, pp. 411–417, 2009.

[17] S. Pei and H.-M. Cheng, "The reduction of graphene oxide," *Carbon*, vol. 50, no. 9, pp. 3210–3228, 2012.

[18] Z.-H. Sheng, X.-Q. Zheng, J.-Y. Xu, W.-J. Bao, F.-B. Wang, and X.-H. Xia, "Electrochemical sensor based on nitrogen doped graphene: simultaneous determination of ascorbic acid, dopamine and uric acid," *Biosensors and Bioelectronics*, vol. 34, no. 1, pp. 125–131, 2012.

[19] M. A. Raj and S. A. John, "Simultaneous determination of uric acid, xanthine, hypoxanthine and caffeine in human blood serum and urine samples using electrochemically reduced graphene oxide modified electrode," *Analytica Chimica Acta*, vol. 771, pp. 14–20, 2013.

[20] Y. Wei, C. Gao, F.-L. Meng et al., "SnO_2/reduced graphene oxide nanocomposite for the simultaneous electrochemical detection of cadmium (II), lead (II), copper (II), and mercury (II): an interesting favorable mutual interference," *The Journal of Physical Chemistry C*, vol. 116, pp. 1034–1041, 2011.

[21] J. Li, D. Kuang, Y. Feng, F. Zhang, Z. Xu, and M. Liu, "A graphene oxide-based electrochemical sensor for sensitive determination of 4-nitrophenol," *Journal of Hazardous Materials*, vol. 201, pp. 250–259, 2012.

[22] W. S. Hummers Jr. and R. E. Offeman, "Preparation of graphitic oxide," *Journal of the American Chemical Society*, vol. 80, no. 6, pp. 1339–1339, 1958.

[23] T. Qi, C. Huang, S. Yan, X.-J. Li, and S.-Y. Pan, "Synthesis, characterization and adsorption properties of magnetite/reduced graphene oxide nanocomposites," *Talanta*, vol. 144, pp. 1116–1124, 2015.

[24] R. Waldron, "Infrared spectra of ferrites," *Physical review*, vol. 99, no. 6, pp. 1727–1735, 1955.

[25] M. Zhang and M. Jia, "High rate capability and long cycle stability Fe_3O_4-graphene nanocomposite as anode material for lithium ion batteries," *Journal of Alloys and Compounds*, vol. 551, pp. 53–60, 2013.

[26] D. Barreca, C. Massignan, S. Daolio et al., "Composition and microstructure of cobalt oxide thin films obtained from a novel cobalt (II) precursor by chemical vapor deposition," *Chemistry of Materials*, vol. 13, no. 2, pp. 588–593, 2001.

[27] D. G. Castner, P. R. Watson, and I. Y. Chan, "X-ray absorption spectroscopy, X-ray photoelectron spectroscopy, and analytical electron microscopy studies of cobalt catalysts. 2. Hydrogen reduction properties," *Journal of Physical Chemistry*, vol. 94, no. 2, pp. 819–828, 1990.

[28] T. Jafari, E. Moharreri, A. S. Amin, R. Miao, W. Song, and S. L. Suib, "Photocatalytic water splitting—the untamed dream: a review of recent advances," *Molecules*, vol. 21, no. 7, p. 900, 2016.

[29] X. Zeng, L. Zhu, G. Jiang, C. Wang, Z. Xia, and R. Yu, "Template-free formation of uniform Fe3O4Hollow nanoflowers supported on reduced graphene oxide and their excellent microwave absorption performances," *Physica Status Solidi (a)*, vol. 215, no. 7, article 1701049, 2018.

[30] B. Qu, C. Zhu, C. Li, X. Zhang, and Y. Chen, "Coupling hollow Fe_3O_4–Fe nanoparticles with graphene sheets for high-performance electromagnetic wave absorbing material," *ACS Applied Materials & Interfaces*, vol. 8, pp. 3730–3735, 2015.

[31] P. Peerakiatkhajohn, J. H. Yun, H. Chen, M. Lyu, T. Butburee, and L. Wang, "Stable hematite nanosheet photoanodes for enhanced photoelectrochemical water splitting," *Advanced Materials*, vol. 28, no. 30, pp. 6405–6410, 2016.

[32] T. Zhu, S. Chang, Y.-F. Song, M. Lahoubi, and W. Wang, "PVP-encapsulated $CoFe_2O_4$/rGO composites with controllable electromagnetic wave absorption performance," *Chemical Engineering Journal*, vol. 373, pp. 755–766, 2019.

[33] K. Zhang, J. Li, F. Wu, M. Sun, Y. Xia, and A. Xie, "Sandwich $CoFe_2O_4$/RGO/$CoFe_2O_4$ nanostructures for high-performance electromagnetic absorption," *ACS Applied Nano Materials*, vol. 2, pp. 315–324, 2018.

[34] Y. Yao, Z. Yang, D. Zhang, W. Peng, H. Sun, and S. Wang, "Magnetic $CoFe_2O_4$–graphene hybrids: facile synthesis, characterization, and catalytic properties," *Industrial & Engineering Chemistry Research*, vol. 51, no. 17, pp. 6044–6051, 2012.

[35] J. Soleymani, M. Hasanzadeh, N. Shadjou et al., "A new kinetic-mechanistic approach to elucidate electrooxidation of doxorubicin hydrochloride in unprocessed human fluids using magnetic graphene based nanocomposite modified glassy carbon electrode," *Materials Science and Engineering: C*, vol. 61, pp. 638–650, 2016.

[36] A. J. Bard and L. R. Faulkner, "Fundamentals and applications," *Electrochemical Methods*, vol. 2, pp. 580–632, 2001.

[37] E. Laviron, "General expression of the linear potential sweep voltammogram in the case of diffusionless electrochemical systems," *Journal of Electroanalytical Chemistry and Interfacial Electrochemistry*, vol. 101, no. 1, pp. 19–28, 1979.

[38] D. Kang, "On the elliptic problems with critical weighted Sobolev-Hardy exponents," *Nonlinear Analysis: Theory, Methods & Applications*, vol. 66, no. 5, pp. 1037–1050, 2007.

[39] W. Horwitz and R. Albert, "Quality IssuesThe concept of uncertainty as applied to chemical measurements," *Analyst*, vol. 122, no. 6, pp. 615–617, 1997.

[40] S. K. Ponnaiah, P. Periakaruppan, and B. Vellaichamy, "New electrochemical sensor based on a silver-doped iron oxide nanocomposite coupled with polyaniline and its sensing application for picomolar-level detection of uric acid in human blood and urine samples," *The Journal of Physical Chemistry B*, vol. 122, no. 12, pp. 3037–3046, 2018.

[41] F. Pan, T.-M. Chen, J.-J. Cao, J.-P. Zou, and W. Zhang, "$Ga(ClO_4)_3$-catalyzed synthesis of quinoxalines by cycloaddition of α-hydroxyketones and _o_ -phenylenediamines," *Tetrahedron Letters*, vol. 53, no. 20, pp. 2508–2510, 2012.

[42] R. Goyal, A. Mittal, and S. Sharma, "Simultaneous voltammetric determination of hypoxanthine, xanthine, and uric acid," *Electroanalysis*, vol. 6, no. 7, pp. 609–611, 1994.

Hindawi
Journal of Nanomaterials
Volume 2020, Article ID 4679061, 14 pages
https://doi.org/10.1155/2020/4679061

Research Article

Voltammetric Determination of Rhodamine B Using a ZIF-67/Reduced Graphene Oxide Modified Electrode

Huynh Truong Ngo,[1,2] Vo Thang Nguyen,[3] Tran Duc Manh,[3] Tran Thanh Tam Toan,[1] Nguyen Thi Minh Triet,[4] Nguyen Thanh Binh,[5] Nguyen Thi Vuong Hoan,[6] Tran Vinh Thien,[7] and Dinh Quang Khieu[1]

[1]*University of Sciences, Hue University, 49000, Vietnam*
[2]*TT-Hue Department of Food Safety and Hygiene, 49000, Vietnam*
[3]*University of Education and Science, The University of Da Nang, 50000, Vietnam*
[4]*Ly Thai To High School, 70000, Vietnam*
[5]*Dalat Nuclear Research Institute, 66000, Vietnam*
[6]*Qui nhon University, 55000, Vietnam*
[7]*University of Natural Resource and Environment of Ho Chi Minh City, 70000, Vietnam*

Correspondence should be addressed to Tran Vinh Thien; tvthien@hcmunre.edu.vn and Dinh Quang Khieu; dqkhieu@hueuni.edu.vn

Received 6 April 2020; Accepted 11 May 2020; Published 3 June 2020

Guest Editor: Yu Liu

In the present article, the synthesis of zeolite imidazolate framework-67/reduced graphene oxide (ZIF-67/rGO) and voltammetric determination of Rhodamine B (RhB) are demonstrated. The obtained materials were characterized by X-ray diffraction, scanning electron microscopy, transmission electron microscopy, X-ray photoelectron spectroscopy, and nitrogen adsorption/desorption isotherms. It was found that the ZIF-67/rGO composite consists of ZIF-67 nano-particles highly dispersed on the rGO matrix and possesses a high specific surface area. Because of the synergistic effect of good conductivity of rGO and high surface area of ZIF-67, the ZIF-67/rGO—modified glassy carbon electrode exhibits good electrochemical behavior toward Rhodamine B (RhB) oxidation. The use of this electrode to quantitate RhB with differential pulse voltammetric method was successful with a broad linear range, from 0.96 to 44.07 $\mu g.L^{-1}$ of RhB and a low limit of detection of 1.79 $\mu g.L^{-1}$. The procedure was able to be applied to quantitatively determine RhB content in several food samples with an exceptional recovery rate (98-103%). The quantitative results highly agreed with that provided by high-performance liquid chromatography, revealing that this material is promising in *in situ* monitoring of other illegal additives in food.

1. Introduction

Rhodamine B (RhB), 9-(2-carboxyphenyl)-6-diethylamino-3-xanthenylidene]-diethylammonium chloride), is one of the xanthene dyes and is highly water-soluble. It is the most common synthetic dyes employed as a colorant in textiles, foodstuffs, plastic, leather, and paper [1]. RhB is thought to be a carcinogen and to exhibit developmental toxicity, neurotoxicity, and chronic toxicity towards humans and animals. It has been illegally used to provide the red color in chili powder and sauces as one of the methods of economically motivated adulteration. Thus, due to the health risks arose from RhB consumption, there have been intensive research efforts to develop a simple method for the determination of RhB in different sample matrix. Some methods are available for the determination of RhB such as spectrophotometric determination with micelle-mediated cloud point extraction [2], UV-Vis Spectrophotoscopy following solid phase extraction [3], magnetic solid phase extraction using ionic liquid-coated core–shell magnetic nanoparticles followed by high-performance

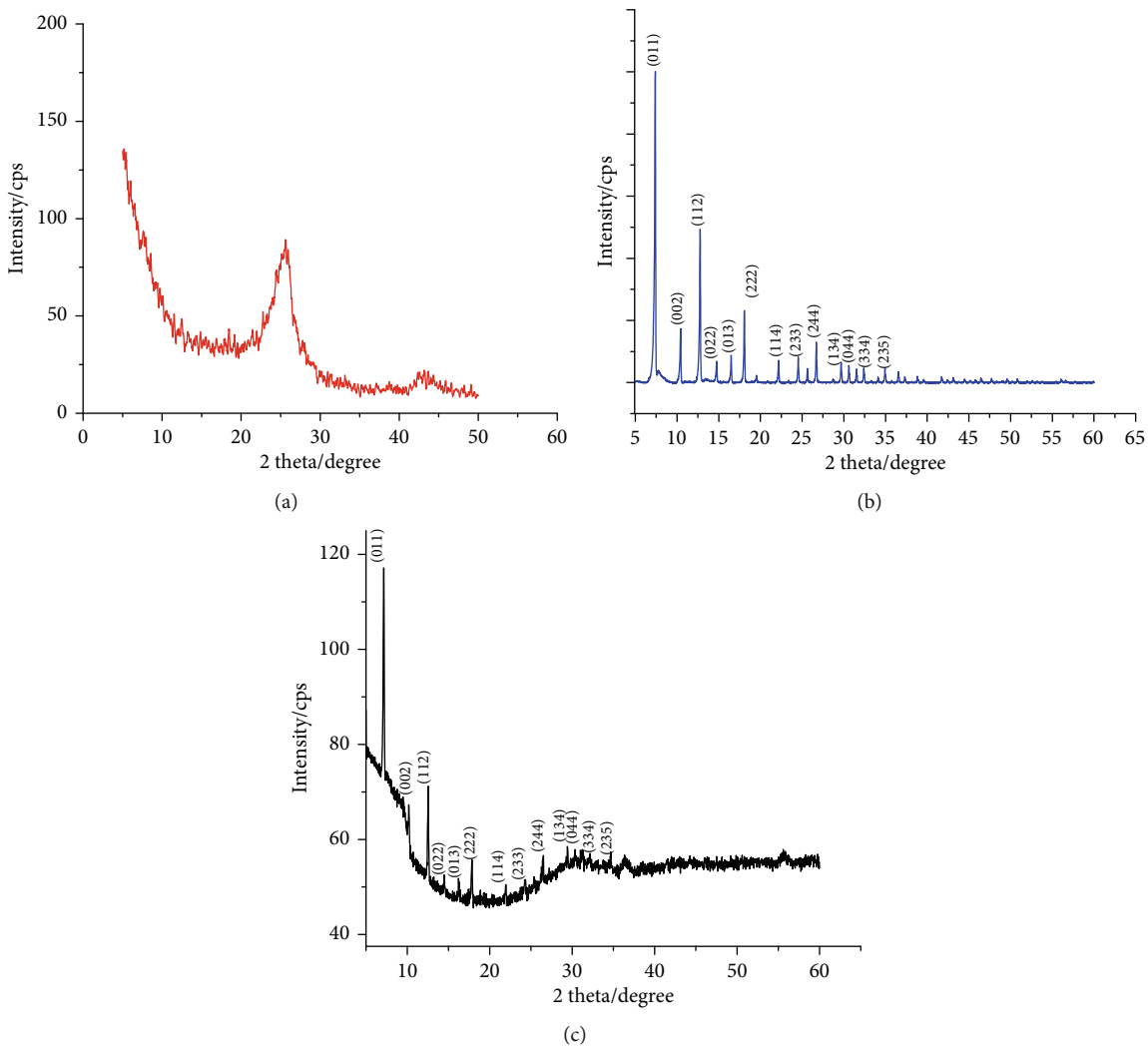

Figure 1: XRD patterns of (a) rGO, (b) ZIF-67, and (c) ZIF-67/rGO.

liquid chromatography [4], and high-pressure liquid chromatography (HPLC) [5, 6]. However, the fact that the operational procedure is complicated, and the cost is high limits the application of these approaches.

The voltammetric approaches have been recognized as the potential methods for the detection of organic and inorganic compounds in trace amount as they offer a simple, low cost, highly selective, and *in situ* operational procedure. The voltammetric method has been employed for the detection of RhB in which it was used to determine RhB in food [7–9]. The development of novel electrodes by modifying them with hybrid organic-inorganic materials provides potential tools in trace analysis of not only RhB but other organic and inorganic substances. Several modified electrodes such as exfoliated graphene-modified electrode [7], silica-pillared zirconium phosphate/nafion composite (SPZP/NAF)-modified electrode [8], betacyclodextrin functionalized nanogold/hollow carbon nanosphere nanohybrid (beta-CD-AuNPs/HCNS)-modified electrode [9], and core-shell-structured Cu@carbon sphere (Cu@CS) nanohybrid-modified electrode have been developed to determine RhB content in different samples by voltammetric methods. Zeolitic imidazolate frameworks-67 (ZIF-67), which are constructed from the tetrahedrally coordinated divalent cations Co^{2+} linked by the imidazolate ligands, are typical ZIFs with high thermal and chemical stability, as well as tunable zeotype topologies. ZIF-67 have been applied in gas storages and adsorption catalyst [10, 11] but has been rarely employed in electrochemistry due to its poor electronic conductivity. Reduced graphene oxide (rGO), an oxidized form of graphene, has attracted great interest in the nanoelectronics and electrochemical industry because it has exhibited outstanding properties such as superior electrical conductivity, high surface area, and chemically stable behaviors. The combination of desirable properties of ZIF-67 and rGO expects a versatile electrode modifier. To our knowledge, few works in the literature have studied the voltammetric determination of Rhodamine B using ZIF-67/rGO/GCE.

In the present paper, the ZIF-67/rGO was synthesized by the microwave-assisted method. The ZIF-67/rGO modified GCE was obtained by drop-casting ZIF-67/rGO suspension on the electrode surface. The electrochemical behaviors of ZIF-67/rGO/GCE were investigated by means of cyclic and

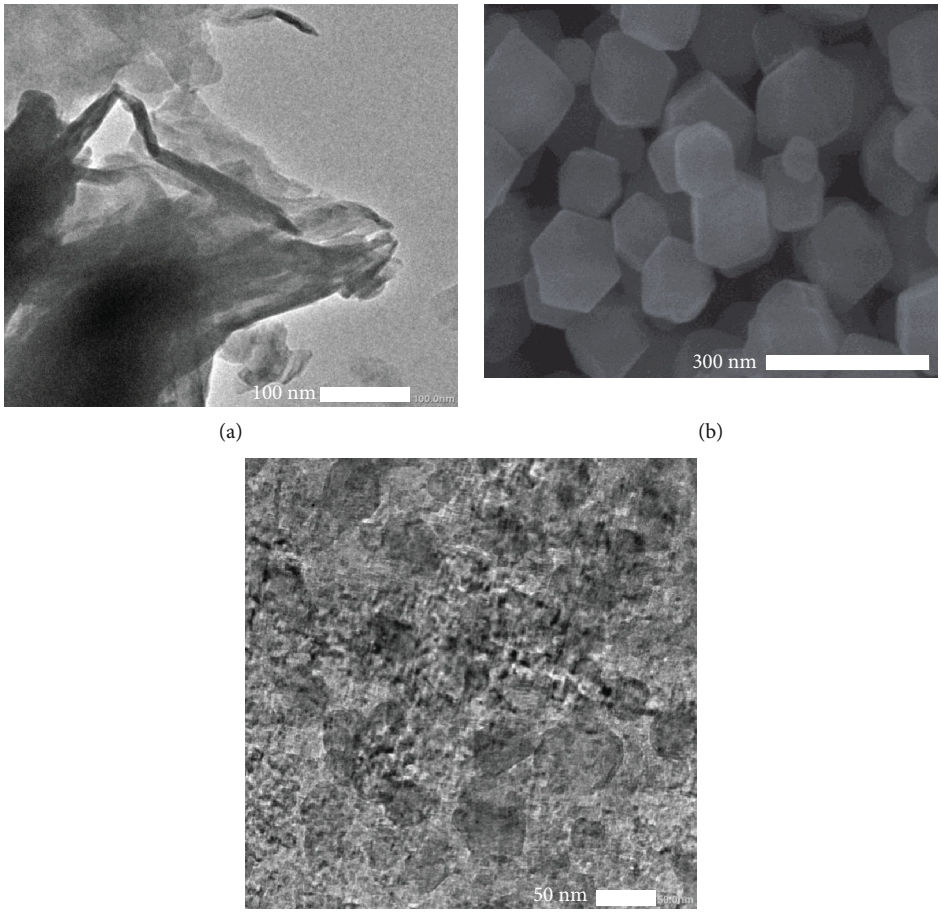

Figure 2: (a) TEM image of rGO. (b) SEM image of ZIF-67. (c) TEM image of ZIF-67/rGO.

differential pulse voltammetry. The modified electrode was employed to determine the RhB in food samples using different pulse voltammetry method, and the results were compared with those from high-performance liquid chromatography.

2. Experimental

2.1. Materials. Cobalt (II) nitrate hexahydrate ($Co(NO_3)_2{\cdot}6H_2O$, Daejung, Korea) and 2-methylimidazole ($C_4H_6N_2$, Sigma-Aldrich, U.S.A., 99%) were used to prepare ZIF-67. Graphite powder, potassium permanganate ($KMnO_4$), sodium acetate ($NaCH_3COO$), sodium citrate ($Na_3C_6H_5O_7$), acetic acid (CH_3COOH, 96%), citric acid ($C_6H_8O_7$), boric acid (H_3BO_3), ammonia solution (NH_4OH, 25%), and ascorbic acid ($C_8H_6O_6$, 99.7%) were purchased from Merck company (Germany). Sodium nitrate ($NaNO_3$), ethanol (C_2H_5OH, 99%), hydroperoxide (H_2O_2, 30%), and potassium hydroxide (KOH) were provided by Daejung company (Korea). Britton–Robinson buffer solutions (BR-BS) were prepared from 0.5 M H_3BO_3, 0.5 M H_3PO_4, and 0.5 M CH_3COOH solutions. The desired pH buffer was adjusted using 1 M KOH or 1 M H_3PO_4 solutions.

2.2. Instrumentation. The morphologies of ZIF-67, GO and ZIF-67/rGO were observed by scanning electron microscopy (SEM) using SEM JMS–5300LV (Japan) and by transmission electron microscopy (TEM) using JEOL-2100F microscope. Ramma spectra were obtained by XPLORA, HORIBA with laser excitation wavelength of 532 nm. Fourier transformation Infrared (FT-IR) analyses were recorded on a Shimadzu IR Prestige–21 (Japan). X-ray diffraction (XRD) patterns were recorded using D8 Advance—Bruker (Germany) with CuK_α radiation ($\lambda = 0.1514$ nm). X-ray photoelectron spectra (XPS) were collected by using a Shimadzu Kratos AXISULTRA DLD spectrometer (Japan). Voltammetric experiments were undertaken at room temperature using a CPA-HH5 Computerized Polarography Analyser (Vietnam) electrochemical workstation. A three-electrode cell configuration, comprising a glassy-carbon working electrode (GCE) with a diameter of 2.8 ± 0.1 mm, the GCE or the modified GCE were used for formatting the modified electrode as a working electrode, an Ag/AgCl/3 M KCl reference electrode, and a platinum wire auxiliary electrode was employed in these experiments.

The Schimadzu 2030 HPLC system was used to analyze Rhodamine B. The chromatographic conditions were as follows: UV detector ($\lambda = 275$ nm), flow rate of 2.0 mL·min^{-1} with the injection volume of 10 μL, column temperature of $45^\circ C \pm 1^\circ C$. The quantitative analysis was performed with external standardisation by measuring the peak areas on the chromatograms.

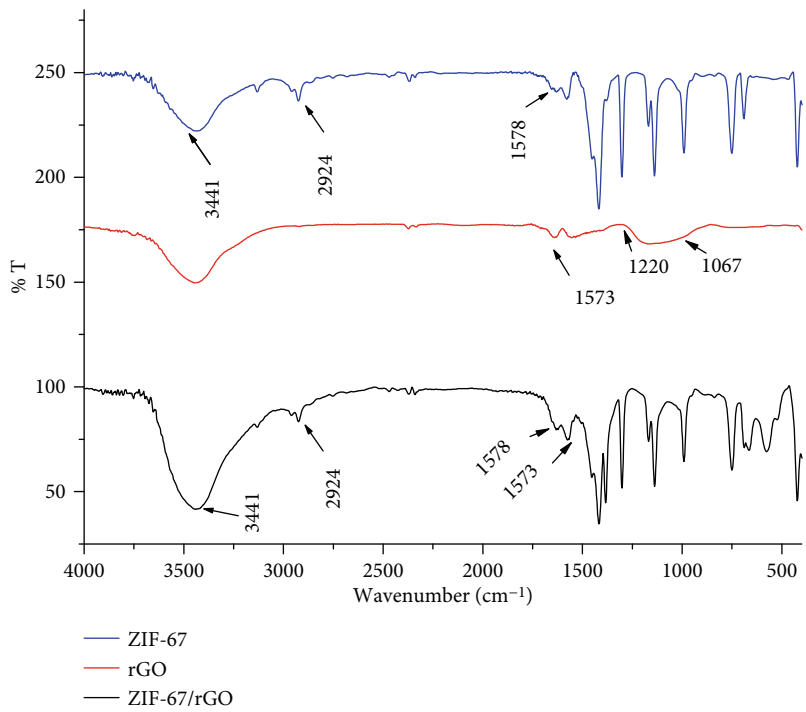

Figure 3: FT-IR spectra of ZIF-67, rGO, and ZIF-67/rGO.

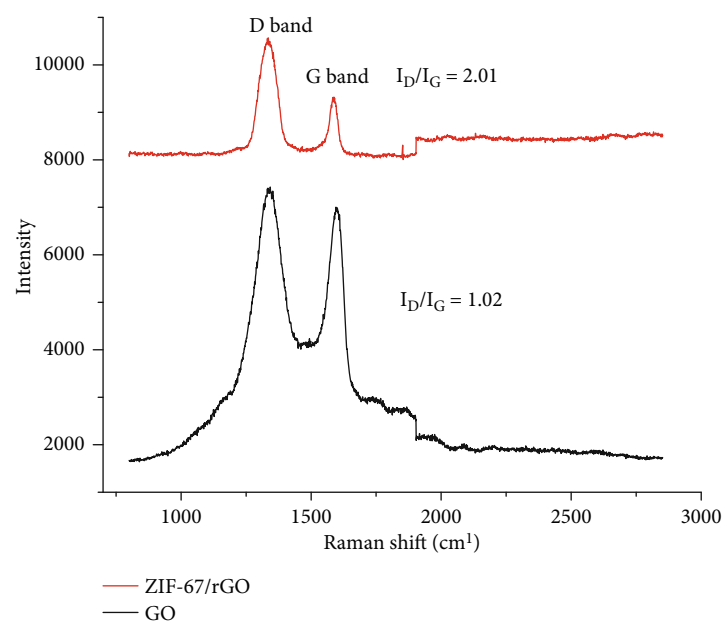

Figure 4: Raman spectra of rGO và ZIF-67/rGO.

2.3. Preparation of ZIF-67/rGO

2.3.1. Preparation of rGO (Reduced Graphene Oxide). Graphite oxide was generated from graphite powder using the Hummers process [12]. Briefly, 3.0 grams of graphite was added to a mixture containing 120.0 mL concentrated H_2SO_4 and 14.0 mL concentrated H_3PO_4 solution, followed by a gradual addition of 6.0 g $KMnO_4$ to this suspension under stirring for 72 hours. 6.0 mL of cold H_2O_2 (30%) was then added to this suspension under stirring for 10 minutes. The obtained solid was separated by centrifuging and washed with a 1.0 M HCl solution until a clear supernatant was clear. The final solid obtained by centrifuging was washed with distilled water to remove any HCl residue. The yellow-brown solid of graphite oxide was obtained after drying at 65°C for 12 hours and then finely ground. The graphite oxide (0.1 g) was exfoliated by ultrasonication in 100.0 mL of distilled water for 1 h to obtain an aqueous suspension of graphene

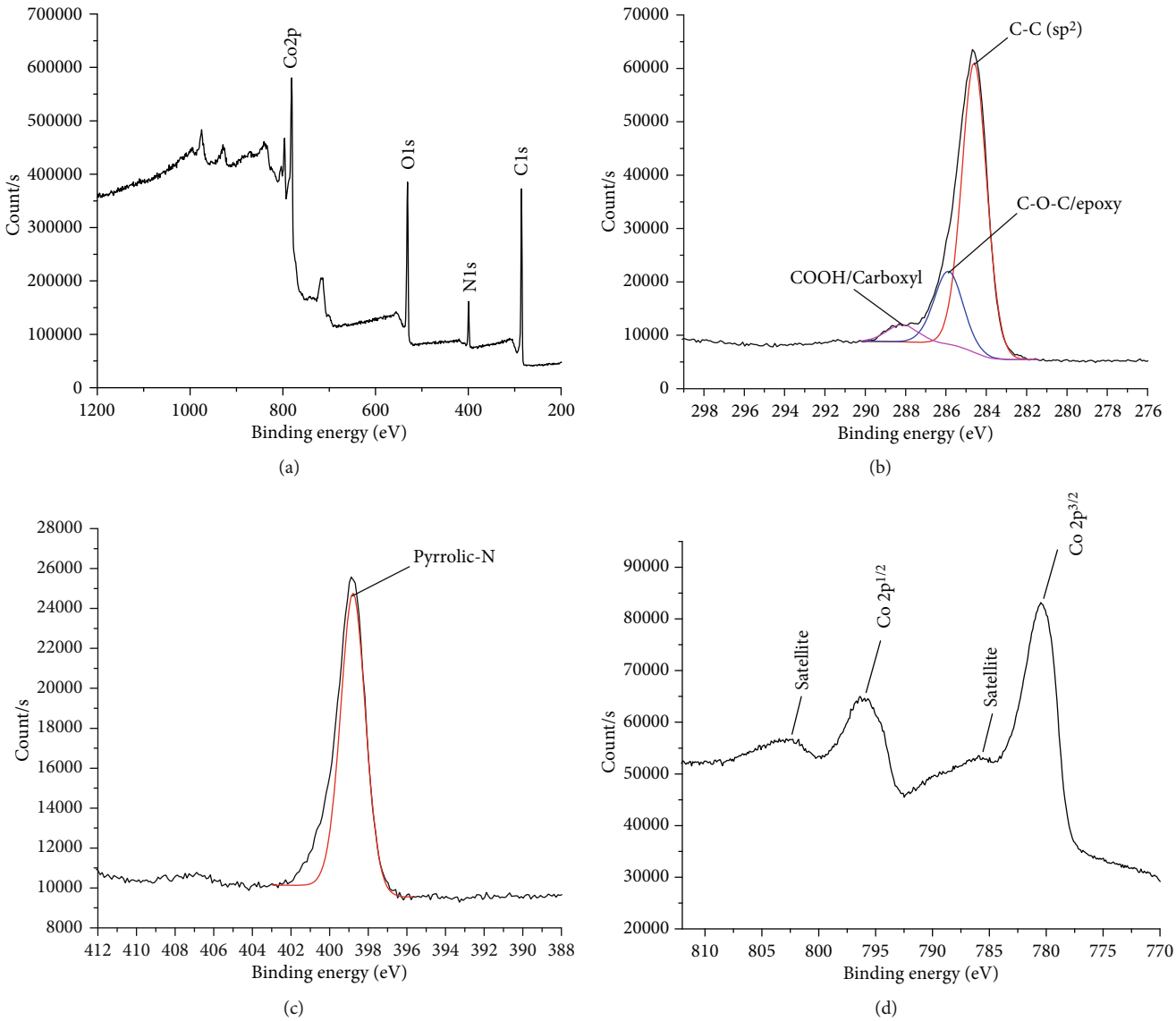

Figure 5: (a) XPS survey spectrum of ZIF67/rGO. (b) XPS C1s spectrum. (c) XPS N1s spectrum. (d) XPS Co2p spectrum.

oxide. Ascorbic acid (0.15 g) was introduced slowly to the graphene oxide suspension, and the mixture was stirred for 8 hours at 50°C to reduced GO. The reduced graphene oxide (rGO) was separated by centrifugation and washed several times with ethanol and dried at 80°C in a vacuum oven for 5 h.

2.3.2. Preparation of ZIF-67 and ZIF-67/rGO Composite. A solvent containing a mixture of ethanol: distilled water: DMF (1 : 1 : 1 in w/w) (denoted as solvent A) was prepared. For the synthesis of ZIF-67/rGO, a stable aqueous suspension of rGO (0.025 g of rGO in 50.0 mL of solvent A) was prepared under ultrasonic irradiation for 1 hour. Then, 10.0 mL of 0.1 M cobalt salt in solvent A was added to this suspension and stirred for 3 hours at ambient temperature. Subsequently, 10.0 mL of 0.2 $g.L^{-1}$ 2-methylimidazole solution in solvent A was also introduced under microwave irradiation for 15 minutes. The final product (ZIF-67/rGO composite) was washed several times with ethanol and distilled water and dried at 80°C in a vacuum oven for 5 h.

The ZIF-67 was also synthesized according to the reference [13] for comparison. Briefly, 2-methylimidazole (16.0 mmol) and $Co(NO_3).6H_2O$ (4.0 mmol) were added into 200.0 mL of a mixture of ethanol: distilled water: DMF (1 : 1 : 1 in *w*/*w*). The resulting mixture was treated by the microwave irradiation time for 40 min (250 W). Then, the purple solid (ZIF-67) was separated by centrifugation and washed with DMF three times and dried at 100°C for 24 hours.

2.4. Preparation and Modification of Electrode. Prior to the modification, the electrode surface was cleaned with ethanol and polished with alumina (0.05 μm). A 1 $mg.L^{-1}$ suspension of ZIF-67/rGO in water was prepared by dispersing 10 mg ZIF-67/rGO into 10 mL of distilled water under ultrasonic condition for 4 hours. The modified electrode was obtained by drop-cast 5 μL of ZIF-67/rGO suspension on the surface of GCE and then dried at ambient temperature. The rGO

or ZIF-67 modified electrode was fabricated in a similar manner by replacing ZIF-67/rGO suspension with ZIF-67 or rGO one.

The samples of tomato and chili sauces were purchased in local area. 15.0 grams of sample was dispersed in 30.0 mL distilled water under ultrasonic stirring within 4 hours and filtered. The RhB concentration in the filtrate was then determined by the proposed method under optimized conditions.

3. Results and Discussion

3.1. Characterization of ZIF-67/rGO Composite. XRD patterns of reduced graphene oxide (rGO), ZIF-67, and ZIF-67/rGO composite were obtained and compared (Figure 1). Figure 1(a) presents a weak and broad reflection peak at *ac.* 26° corresponding to the relative short-range order structures in disordered stacked rGO [14], which indicates the successful reduction of graphene oxide. The XRD pattern in Figure 1(b) exhibits the characteristic peaks of ZIF-67 corresponding to planes (011), (002), (112), (022), (013), (222), (114), (223), (244), (134), (044), (334), and (235) according to CCDC671073 database. The formation of ZIF-67/rGO composite is confirmed with the appearance of the characteristic peaks of ZIF-67 in the XRD pattern but in lower intensity. The characteristic peaks of rGO at 26° are not observed due to the overlap of ZIF-67 diffractions.

The morphology of the obtained materials was observed by TEM and SEM images. The TEM image of rGO shows a stacked and crumpled morphology, revealing deformation because of the exfoliation and restacking process [15] (Figure 2(a)). The ZIF-67 crystal particles aggregated and were in uniform polyhedral morphology with the size of 140 ± 5.6 nm (counted for 50 particles) (Figure 2(b)). The TEM image of ZIF-67/rGO composite shows that the ZIF-67 particles with an average size of 50-70 nm dispersed well on the rGO sheet (Figure 2(c)). The formation of composite material in this experimental condition can be explained when considering the possible interactions between the reactants. Upon adding Co^{2+} to rGO suspension, there may be an interaction between Co^{2+} with oxygen-containing functional group in rGO, although this interaction can be weak. Therefore, as 2-methylimidazole is introduced into the mixture, its bonding to Co^{2+}, which is stronger than its competence mentioned above, is formed to generate ZIF-67 as particles of around 10-20 nm dispersing on the rGO matrix as shown in Figure 2(c). The synthesis of ZIF-67 on rGO matrix limits the possibility of ZIF-67 crystals growth. Consequently, its size is significantly smaller compared with that of ZIF-67 synthesized separately as shown in Figure 2(c).

The formation of ZIF-67, rGO, and ZIF-67/rGO composite is also confirmed by the FT-IR spectra (Figure 3). The position of characteristic absorption bands of ZIF-67 synthesized in this study is in good agreement with those reported previously [16]. The absorption band centered at 3441 cm^{-1} is assigned to the stretching of OH in water adsorbed in material. The main absorption peaks from 600-1500 cm^{-1} are assigned to the vibrations of functional groups in

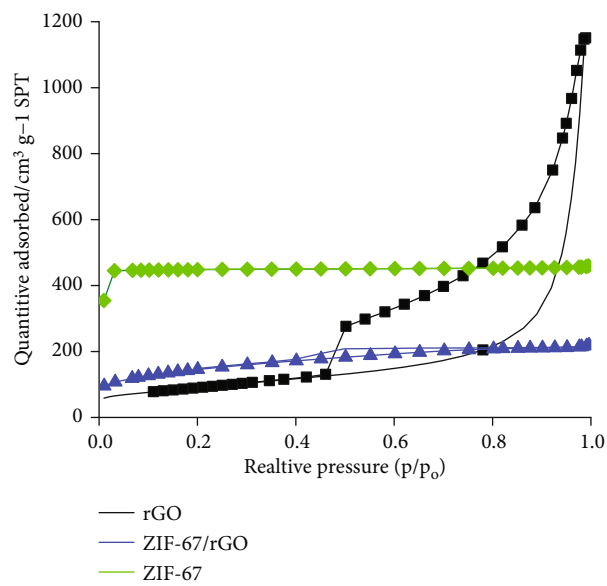

Figure 6: Nitrogen adsorption/desorption isotherms of ZIF-67 (green), rGO (black), and ZIF-67/rGO (blue).

2-methylimidazole, in which the peak at 1578 cm^{-1} can be attributed to the stretching vibration of C=N bond and the peak at 2924 cm^{-1} belongs to the symmetric stretching vibration of CH_3 [17]. The absorption band at 1573 cm^{-1} in the FT-IR spectrum of rGO can be attributed to the skeletal vibration of graphene sheets. The vibration of C–O stretching of epoxy group and alkoxy is observed at broad peak from 1220 cm^{-1} to 1067 cm^{-1} due to incomplete reduction of GO [18]. The FT-IR spectrum for ZIF-67/rGO exhibits a combination of infrared peaks of ZIF-67 and rGO indicating that the structures of ZIF-67 and GO are maintained in the composite.

Raman spectroscopy can also be employed to effectively probe the disorder in the carbon structure of the material. In the Raman spectra of rGO and rGO/ZIF-67 (Figure 4), two peaks are clearly visible at 1336 cm^{-1} and 1602 cm^{-1}, corresponding to the so-called D and G bands, respectively. It is reported that the D band peak corresponds to the breathing mode of κ-point phonons of A_{1g} symmetry, and the G band peak represents the first-order scattering of the E_{2g} phonons [19]. The intensity of the D band is related to the size of the in-plane sp2 domains, and the relative intensity ratio (ID/IG) is a measure of the extent of disorder [19]. An increase in intensity ratio (I_D/I_G) and the higher intensity of D band indicate the presence of more isolated graphene domain in ZIF-67/rGO compared to in rGO. It is found that the intensity ratio of I_D/I_G is 1.02 for rGO and 2.01 for ZIF-67/rGO. The results confirm that the composite consists of rGO and ZIF-67 structures.

The oxidation states of elements were examined by XPS (Figure 5). The XPS survey spectrum presents the existence of Co, O, N, and C in ZIF-67/rGO composite (Figure 5(a)). The C1s spectrum of ZIF-67/rGO (Figure 5(b)) is able to be fitted by three components at 284.59, 285.87, and 288.16 eV, corresponding to carbon in aromatic rings, epoxy C-O-C, and carboxyl COOH groups, respectively [15, 20]. These components indicate that the reduction of graphene

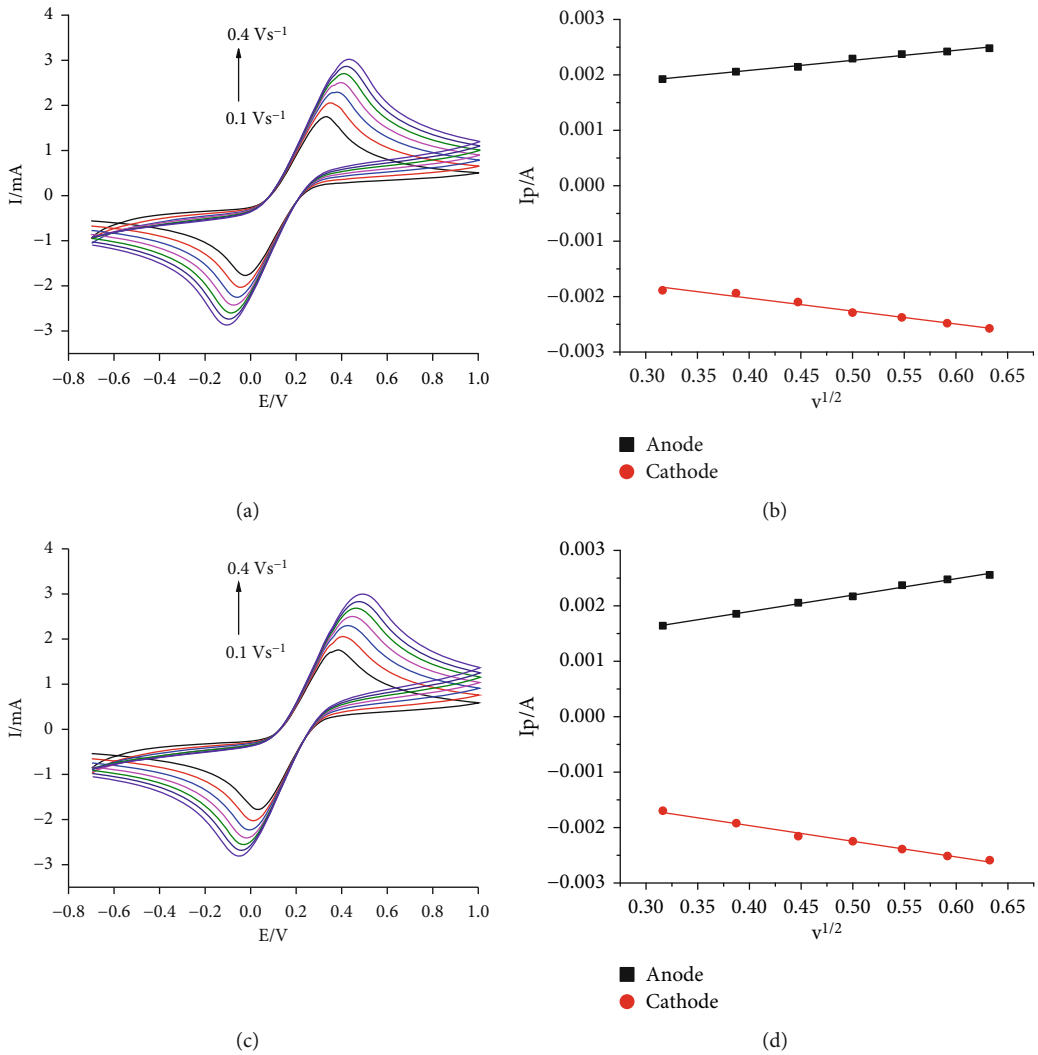

Figure 7: Cyclic voltammograms (CVs) obtained in aqueous solution (0.1 M KCl) containing 1.0 mM $K_3[Fe(CN)_6]$ at designated scan rate (from 0.1 to 0.4 Vs^{-1}) at different electrodes (a) bare GCE. (b) The corresponding linear plot of peak current (*Ip*) vs. $v^{1/2}$ and (c) ZIF-67/rGO-GCE. (d) the corresponding linear plot of *Ip* vs. $v^{1/2}$.

oxide is not complete. The N1s XPS spectrum at 400 eV represents a dominant contribution from nitrogen atom in the pyrrolic-N and a shoulder at 398.8 eV, which possibly due to the interaction of N-imidazolate with graphene sheets (Figure 5(c)) [21]. The Co2p spectrum exhibits two main peaks coupled with two satellites, 805.01 eV coupled with 797.7 eV for Co2p1/2 and 785.7 eV coupled with 780.5 eV for Co2p3/2 [22] (Figure 5(d)). The estimation of the oxidation states of Co cations can be done by analyzing the energy gap between the Co2p main peak and the satellite peak. Typically, this energy gap of Co(II) cation is *ca.* 6.0 eV, while that of Co(III) cation is approximately 9-10 eV [23, 24]. In the present case, the energy gap of cobalt cation is 6.27 eV for Co2p1/2 and 5.2 for Co2p3/2. Therefore, Co(II) is the main form in the as-prepared ZIF-67 material.

The textural properties of ZIF-67, rGO, and ZIF-67/rGO were examined via nitrogen adsorption-desorption isotherms (Figure 6). The ZIF-67 material exhibits a typical type-I adsorption isotherm with a high amount of N_2 adsorption indicating high porosity. An increase in adsorption volume at a low relative pressure indicates the existence of micropores in all ZIF-67 samples. The isotherm curves of rGO and ZIF-67/rGO belong to typical type IV according to IUPAC classification. The presence of the hysteresis loop at high relative pressure region indicates the existence of mesopore which can be attributed to the void among the primary particles [25, 26]. The specific surface areas of ZIF-67, rGO, and ZIF-67/rGO derived from the BET model are found to be 1330 $m^2.g^{-1}$, 200 $m^2.g^{-1}$, and 498 $m^2.g^{-1}$, respectively. The surface area ZIF-67/rGO sample in this study is higher than that of rGO based materials reported previously [27, 28].

3.2. Voltammetric Determination of Rh-B Using ZIF-67/rGO Modified Electrode

3.2.1. The Electroactive Surface Area of ZIF-67/rGO-GCE. The electrochemical behavior of different electrodes was characterized via cyclic voltammetry (CV) experiments on $K_3[Fe(CN)_6]$ solution. Figures 7(a) and 7(c) present the

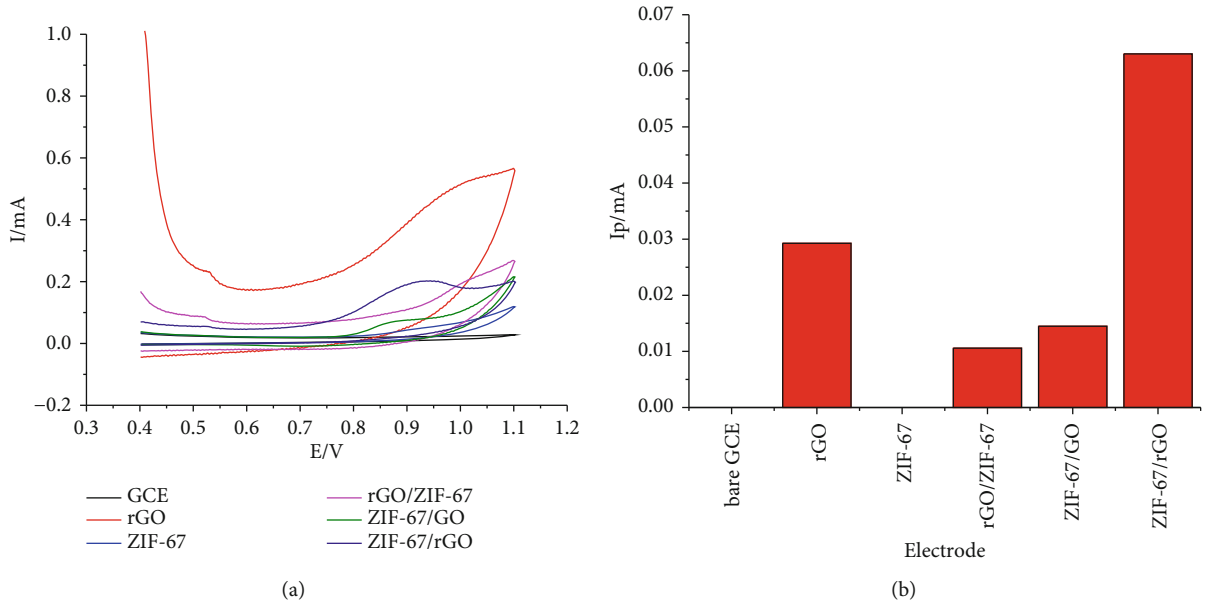

Figure 8: (a) CVs obtained in aqueous solution containing 24 mg/L RhB (0.1 M BR-BS pH 6) and (b) the corresponding anodic peak currents at different electrodes.

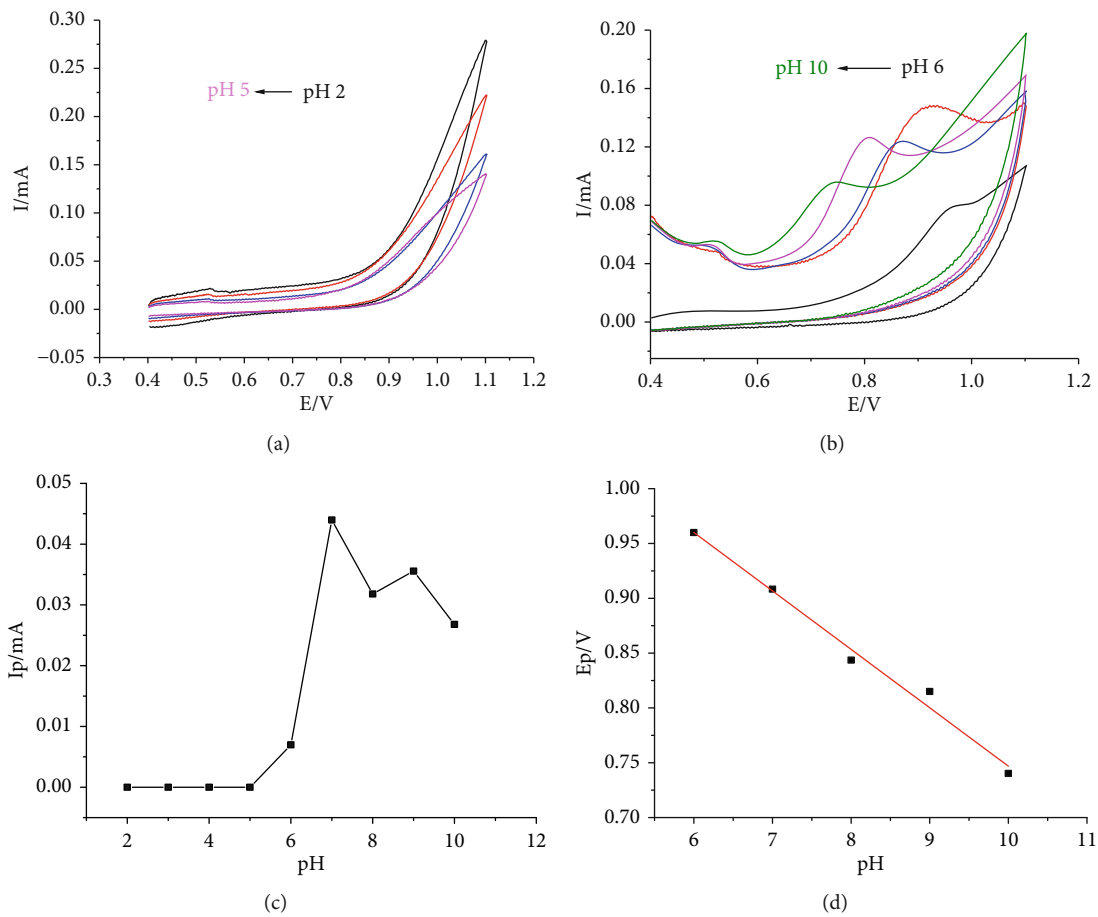

Figure 9: (a) Cyclic voltammograms (CV) obtaining with ZIF-67/rGO-GCE in aqueous solution containing 24 mg/L RhB at pH = 2 – 5. (b) At pH = 6 – 10. (c) The dependence of pH on the anodic peak current (*Ip*). (d) The linear plot of the anodic peak potential (*Ep*) *vs.* pH.

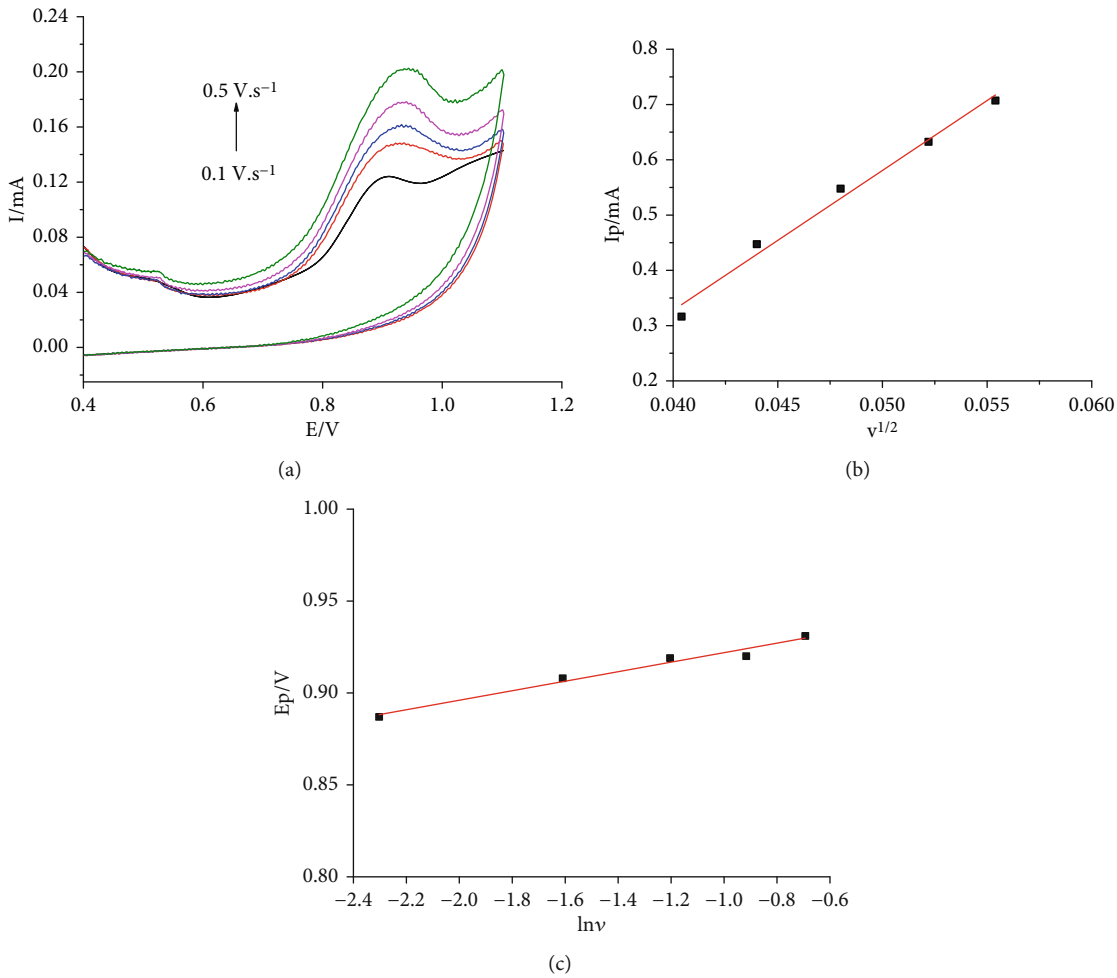

Figure 10: (a) CVs obtained with ZIF-67/rGO-GCE in aqueous solution (0.1 M BR-BS pH 7) containing 24 mg/L RhB at designated scan rates. (b) The plot of *Ipvs.* $v^{1/2}$. (c) The linear plot *Epvs* ln$v$.

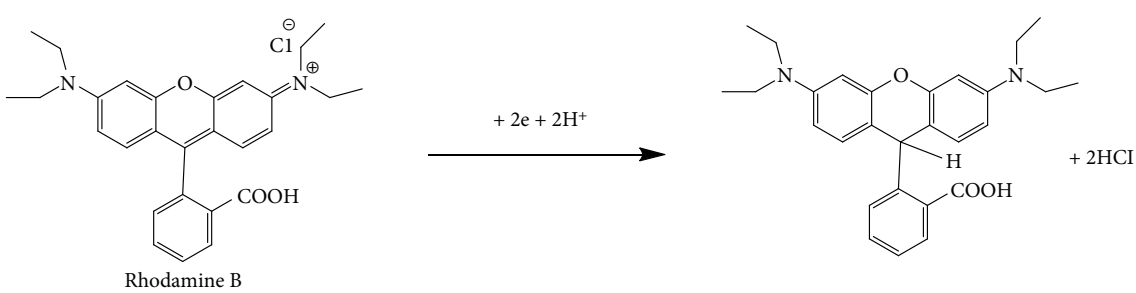

Scheme 1: Oxidation mechanism of RhB.

CVs using bare GCE and ZIF67/rGO/GCE in 1.0 mM $[Fe(CN)_6]^{3-}$ solution (0.1 M KCl). For a reversible process, the anodic peak current (*I*pa) is proportional to the square root of scan rates (v1/2) as describe in Randles-Sevcik formula:

$$Ipa = 2.69x10^5 n^{3/2} AD^{1/2} C0v^{1/2} \quad (1)$$

where *I*pa is the peak current (anodic peak current), n is the number of electrons transferred ($n = 1$ in the $[Fe(CN)_6]^{3-/4-}$ redox system), A is the surface area of electrode (cm^2), $C0$ is the concentration of $[Fe(CN)_6]^{3-}$, $D0$ is the diffusion coefficient of the $[Fe(CN)_6]^{3-/4-}$ ($Co = 1$ mM; $6.7 \times 10 - 6$ cm2 s − 1 [29]), and v is the scan rate ($V.s^{-1}$).

Therefore, from the linear plot of the *I*pa versus $v^{1/2}$ (Figures 7(b) and 7(d)), the value of A is found to be 0.070 cm^2 for bare GCE and 0.117 cm^2 for ZIF-67/rGO-GCE indicating that the effective electroactive surface area of the modified electrodes is improved significantly.

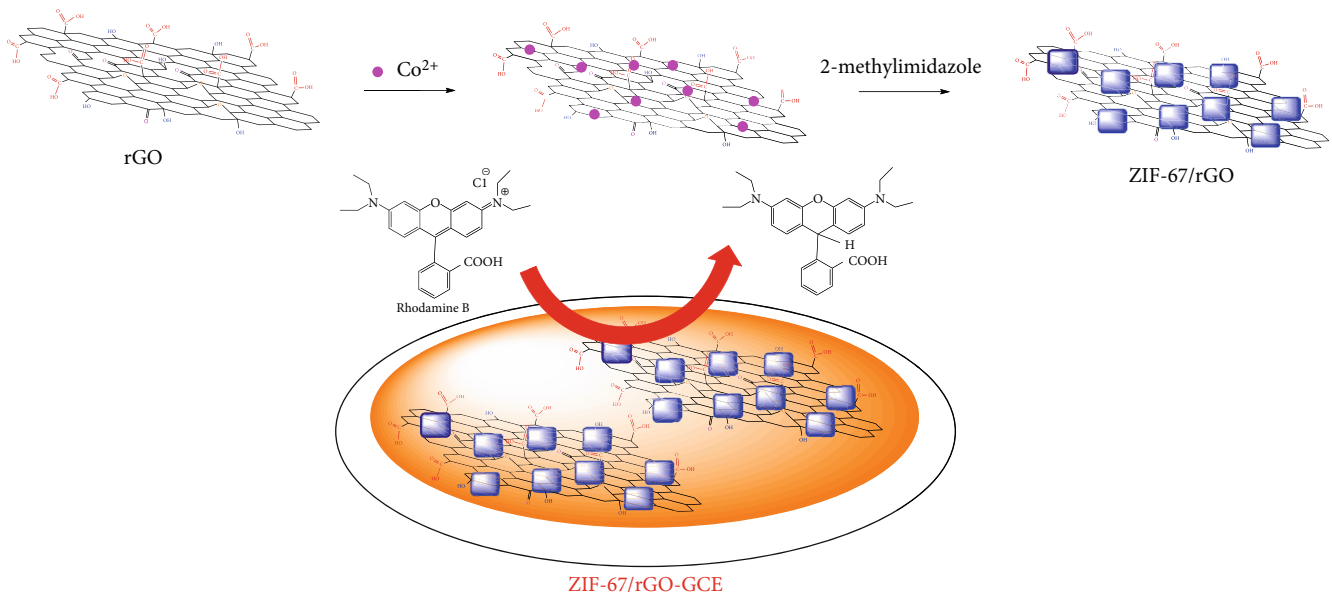

Scheme 2: The proposed mechanism of electrode process for RhB oxidation.

3.2.2. Cyclic Voltammetry Behavior of RhB at ZIF-67/rGO/GCE

(1) Cyclic Voltammetry Behavior. Figure 8(a) presents the CVs of RhB at bare GCE, ZIF-67/GCE, rGO/GCE, and ZIF-67/rGO-GCE. It is clear that there is no obvious redox peak on the CVs with the use of bare GCE and ZIF-67/GCE. When rGO/GCE was used, on the scan toward positive potential, the rise of oxidation current at 0.92 V indicating an oxidation process of RhB at the electrode surface. No reduction process can be observed on the reversed scan suggesting that this is an irreversible process. However, the CV behavior on ZIF-67/rGO-GCE assembles that on rGO/GCE, except the fact that this electrode significantly enhances not only the shape of the oxidation peak but also the peak current at 0.92 V. It is found that the peak current magnitude is 2.2 times higher compared with rGO/GCE (Figure 8(b)). The ZIF-67/rGO-GCE exhibits good electroactivity toward the oxidation of RhB probably due to the synergistic effect of high electrical conductivity of rGO [30] and excellent textural properties of ZIF-67, including large surface area, abundant number of adsorptive sites, and large volume of porosity.

(2) Effect of pH. Figure 9 presents the effect of pH on electrochemical responses of CV. At solution pH lower than 5, the oxidation peak cannot be observed (Figure 9(a)). However, the peak becomes more apparent at pH > 6 and the peak current magnitude reaches a maximum value at pH 7 (Figures 9(b) and 9(c)). Hence, pH = 7 was selected for further experiments. Furthermore, upon increasing pH from 6 to 10, the peak potential shifts to more negative value from 0.96 V to 0.74 V indicating that the protons are involved in the RhB oxidation at electrode. The relationship between pH of solution and oxidation peak potential is plotted as in Figure 9(d) illustrating a linear correlation.

Table 1: Tolerance limit of interfering species at 5.7 μg.L^{-1} RhB.

Interferent	Concentration interferent (mg/L)	Concentration ratio of Interferent/RhB	RSD (%)
Saccharine	570	100	4.2
Glucose	342	60	5
Sodium benzoate	285	50	4.9
Saccharine	285	50	4.2
K_2CO_3	583	>100	<5
Na_2SO_4	285	50	4.3
$Ca(H_2PO_4)_2$	580	>100	<5
NaCl	595	>100	<5

The linear regression equation of *Ep* against pH is expressed as follows:

$$Ep = (1.27 \pm 0.03) + (-0.053 \pm 0.003)pH \quad r = 0.993 \quad (2)$$

The value of 0.053 is close to the theoretical Nestian value of 0.0592 (Figure 9(d)) implying that the oxidation reaction of RhB at electrode involves an equal number of electrons and protons.

(3) Effect of Scan Rate. Effect of scan rate on electrochemical signals also provides the information on oxidation mechanism (Figure 10). Upon increasing scan rates, the cathodic peak current magnitude grows along with the shift of peak potential to more positive value as shown in Figure 10(a) implying a nondiffusion controlled process.

In order to confirm whether the electrooxidation reaction is diffusion controlled or adsorption controlled, the

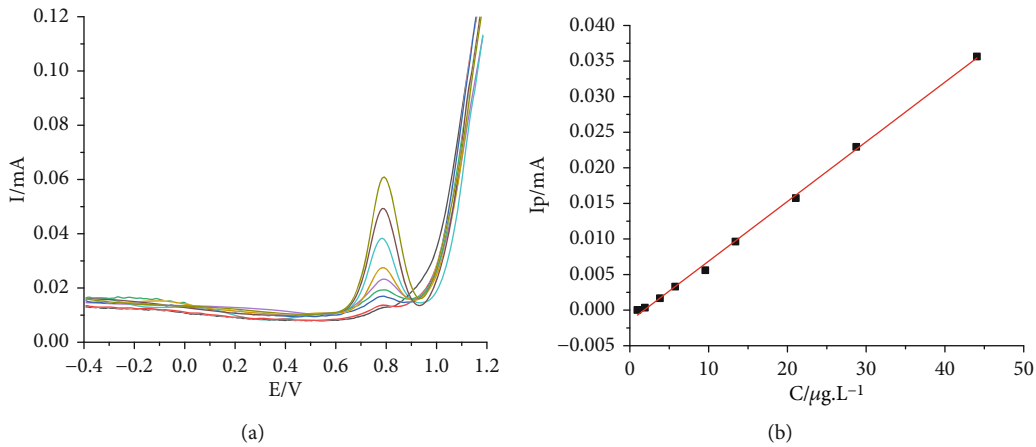

Figure 11: (a) DPV curves of different concentration of RhB at ZIF-67/rGO modified electrode in 0.1 M BR-BS pH 7. (b) A linear plot of *I*pa *vs.* RhB concentration.

dependence between Ip and $v^{1/2}$ was plotted (Figure 10(b)). The linear regression equation of Ip vs $v^{1/2}$ is derived as follows:

$$Ip = (0.039 \pm 0.008)\, v^{1/2} + (0.027 \pm 0.0045),\ r = 0.993 \quad (3)$$

The plot of Ip vs. square root of the scan rate is highly linear ($r = 0.993$). The value in bracket presents the confidence interval of 95%. With a confidence interval of 95%, the intercept varies from 0.023 to 0.032 which means that the oxidation of RhB at the modified electrode is an adsorption controlled process [14, 31].

The dependence of anodic peak potential (Ep) on the scan rate also provides another insight into the mechanism of the process. The number of electrons transferred during the oxidation process can be determined via the relation of peak potential (Ep) and natural logarithm of scan rate expressed by Laviron equation: [32].

$$E_p = E^0 - \frac{RT}{(1-\alpha)nF} \ln \frac{RTK_s}{(1-\alpha)nF} + \frac{RT}{(1-\alpha)nF} \ln v \quad (4)$$

where $E0$ is the formal redox potential, ks is the apparent electron-transfer rate constant, α is the charge transfer coefficient, n is the number of electrons transferred, v is the scan rate ($V.s^{-1}$), and $T = 298$ K, $R = 8.314$ J mol K − 1, and $F = 96480$ C mol − 1.

From the plot (Figure 10(c)), the linear regression equation of Ep vs. lnv can be written as follow:

$$Ep, RhB = (0.112 \pm 0.004) + (0.026 \pm 0.003) \ln (v) \quad r = 0.984 \quad (5)$$

The value of $n(1-\alpha)$ obtained from the slope of the linear regression line of Eq. (6) is found as 0.99. The value of α is assumed to be 0.5, which is commonly used for a totally irreversible system [33]. Therefore, the number of electrons transferred (n) in the electro-oxidation of RhB is 1.98, which implies that the oxidation mechanisms for RhB can involve two electrons and two protons.

The oxidation mechanism of RhB oxidation on the electrode surface can be illustrated in Scheme 1.

The enhancement of RhB oxidation on ZIF-67/rGO/GCE can be explained by the improvement of RhB absorption on this electrode due to the contribution of various intermolecular interactions between RhB and each individual component of the electrode. The interaction can be electrostatic interaction between ionic RhB with charged ZIF-67/rGO surface, depending on pH, or π–π stacking interactions between 2-methylimidazole ligand of ZIF-67 and the π-electron of benzene ring in RhB moiety, or complexation interaction between Co(II) and carboxyl group (Scheme 2).

3.2.3. Quantitative Determination of RhB Using Differential Pulse Voltammetry Method (DPV). Differential pulse voltammetry method, which is more sensitive than the CV approach, using a ZIF67/rGO/GCE was investigated to quantify the RhB content in real samples, normally at low concentration. By using a solution containing 21.1 μg/L RhB, the operational parameters were optimized as follows: accumulation potential: -0.2 V; accumulation time: 20s; pulse altitude: 0.06 V; rating potential: 0.008 V (Figure S1-4).

(1) Interference, Reproducibility, Repeatability, Linear Range and Limit of Detection. Relative standard deviation (RSD) is applied to estimate the effect of some potential interfering species on the detection of RhB in which the $RSD = (Io - I)/Io$ where Io is peak current measured without and with interference. The tolerance limit is defined as the maximum concentration of the interferent that leads to a RSD of over ±5%. This value of some possible inorganic and organic substances in the use of 5.7 $\mu g.L^{-1}$ RhB is given in Table 1. For inorganic salts, except for Na_2SO_4, tested at 50-fold excess, all other inorganic substances at 100-fold excess show no interference effect on the detection of RhB. Similarly, saccharine (at 100-fold excess), glucose (60-fold excess), sodium benzoate, and saccharine (50-fold excess) do not interfere the signal of RhB.

The reproducibility was investigated with nine individual ZIF-67/rGO-GCEs in the detection of 5.7 μg/L RhB under

Table 2: Comparison of LOD and linear range of the proposed method with the previous methods.

Methods	Linear range (μg/L)	LOD (μg/L)	References
Magnetic solid phase extraction with ionic liquid coated-core shell-magnetic nanoparticles followed by high-performance liquid chromatography	0.5–150	0.08	[4]
Solid phase extraction with Sepab eads SP 70 resin followed by UV-Vis spectrophotometry	250–3000	3.4	[3]
Micelles mediated separation fluorimetric methodology	0.0467–100	0.014	[1]
Cyclodextrin-functionalized nanogold/hollow carbon nanospheres modified electrode, DPV method	4.79–958.00	0.96	[9]
Silica-pillared zirconium phosphate/nafion Composite modified glassy carbon electrode, DPV	0.005–2.395	2.06	[8]
Core-shell structured Cu@carbon sphere nanohybrid modified electrode, DPV	143.7–1437	47.9	[35]
Glassy carbon electrode, DPV	4.78–956.1	2.93	[36]
ZIF-67/rGO modified electrode, DPV	0.96–44.07	1.79	The present work

Table 3: Recovery and precision of Rhodamine B in different spiked food samples.

Sample	RhB added (μg/mL)	DPV RhB found ± SD (μg/mL)	ReV (%)	HPLC RhB found ± SD (μg/mL)	ReV (%)
Tomato sauce #1	0	0	98	0	99
	100	98.0 ± 0.9		99.2 ± 0.5	
Tomato sauce #2	0	0	96	0	101
	100	95.9 ± 0.8		101 ± 1	
Chili sauce	0	0	103	0	98
	100	103.0 ± 2.0		98.3 ± 0.2	

SD: standard derivation; ReV: recovery.

the optimized conditions. It was found that a good reproducibility with the RSD of the current responses of 7.0% can be obtained. The expectable RSD for nine independent electrodes indicates the good reproducibility of the ZIF-67/rGO-GCE in the present work.

The repeatability of ZIF-67/rGO-GCE for DPV was also studied with the solutions of 5.7; 21.1 and 44.1 μg/L RhB. The determination of 5.7, 21.1, and 44.1 μg/L RhB was measured successively for nine times (Figure S5). The obtained RSD for 5.7, 21.1, and 44.1 μg/L RhB was 6.2, 3.9, and 0.8%, respectively, which are lower than the 1/2 $RSD_{\text{Horwitz predicted}}$ [34]. Such reasonable RSD of successive measurements confirm that the ZIF-67/rGO-GCE is able to be repeatedly used for the determination of RhB in either low concentration range or high concentration range.

Figure 11 presents the DPV curves of different RhB concentration in 0.1 M BR-BS pH 7. As shown in the figure, the linear concentration range of RhB is 0.96–44.07 μg/L and the regression equation is expressed as follows:

$$I\text{pa} = (-0.0015 \pm 0.0001) + (8.38643 \pm 0.00001)C_{\text{RhB}} \quad r = 0.999 \tag{6}$$

The LOD, calculated by 3 Sy/b, where Sy is the standard deviation of y-residuals and b is the slope of linearity, is found to be 1.79 μg.L^{-1}.

The detection performance of the ZIF-67/rGO modified electrode in DPV method was compared with the other methods as shown in Table 2. It could be noticed that the linear range and LOD of RhB at the ZIF-67/rGO-GCE are lower or comparable with those results reported previously. The ZIF-67/rGO modified electrode presents a lower LOD compared to UV-Vis spectrophotoscopy method with solid phase extraction using Sepab eads SP 70 resin, or voltammetric method using silica-pillared zirconium phosphate/nafion composite modified glassy carbon electrode. Overall, the ZIF-67/rGO composite is proved to be an effective electrode modifier for the detection of RhB in aqueous solution.

3.2.4. Real Sample Analysis. In order to assess the application of the proposed method on real samples, two samples of tomato sauce and one of the chili sauce were chosen to use for the spiked experiments in comparison with the results from high-performance liquid chromatography (HPLC). The results are given in Table 3 showing that all samples are free of RhB and the recovery is in the exceptional range of 98–103% with RSD less than 2%. The results obtained by this method are in statistical agreement with those by HPLC method (paired samples t-test, $t(2) = 0.99$, $p = 0.427 > \alpha = 0.05$) manifesting that the voltammetric method using ZIF-67/rGO-GCE is satisfactory.

4. Conclusions

A novel modified electrode for RhB quantifying was developed based on the composite of ZIF-67 and reduced graphene oxide. Owing to synergetic effects from rGO with good electroconductivity properties and ZIF-67 with excellent textural properties, the use of ZIF-67/rGO modified electrode in DPV technique provides the broad linear response range and low LOD of RhB detection. Furthermore, the ZIF-67/rGO-GCE has good stability and reproducibility making the proposed method a prospective application for the determination of RhB in foodstuffs.

Data Availability

The data used to support the findings of this study are available from the corresponding author upon request.

Conflicts of Interest

The authors declare that they have no conflicts of interest.

Acknowledgments

This research is funded by Vietnam National Foundation for Science and Technology Development (NAFOSTED) under grant number 104.06-2018.15.

Supplementary Materials

Figure S1: (a) DPV curves of 21.1 μg/L RhB in 0.1 M BR-BS pH 7 and (b) anodic peak current (Ip) at different accumulation potentials. Figure S2: (a) DPV curves of 21.1 μg/L RhB in 0.1 M BR-BS pH 7 and (b) anodic peak current (Ip) at different accumulation times. Figure S3: (a) DPV curves of 21.1 μg/L RhB in 0.1 M BR-BS pH 7 and (b) anodic peak current (Ip) at different pulse amplitudes. Figure S4: (a) DPV curves of 21.1 μg/L RhB in 0.1 M BR-BS pH 7 and (b) anodic peak current (Ip) at different rating potentials. Figure S5: DPV curves measured successively for nine times at 5.7, 21.1, and 44.1 μg/L RhB. *(Supplementary Materials)*

References

[1] M. Alesso, G. Bondioli, M. C. Talío, M. O. Luconi, and L. P. Fernández, "Micelles mediated separation fluorimetric methodology for rhodamine B determination in condiments, snacks and candies," *Food Chemistry*, vol. 134, no. 1, pp. 513–517, 2012.

[2] N. Pourreza, S. Rastegarzadeh, and A. Larki, "Micelle-mediated cloud point extraction and spectrophotometric determination of rhodamine B using triton X-100," *Talanta*, vol. 77, no. 2, pp. 733–736, 2008.

[3] M. Soylak, Y. E. Unsal, E. Yilmaz, and M. Tuzen, "Determination of rhodamine B in soft drink, waste water and lipstick samples after solid phase extraction," *Food and Chemical Toxicology*, vol. 49, no. 8, pp. 1796–1799, 2011.

[4] J. Chen and X. Zhu, "Magnetic solid phase extraction using ionic liquid-coated core-shell magnetic nanoparticles followed by high-performance liquid chromatography for determination of rhodamine B in food samples," *Food Chemistry*, vol. 200, pp. 10–15, 2016.

[5] C. Franke, H. Westerholm, and R. Niessner, "Solid-phase extraction (SPE) of the fluorescence tracers uranine and sulphorhodamine B," *Science*, vol. 31, no. 10, pp. 2633–2637, 1997.

[6] L. Gagliardi, D. De Orsi, G. Cavazzutti, G. Multari, and D. Tonelli, "HPLC determination of rhodamine B (C.I. 45170) in cosmetic products," *Chromatographia*, vol. 43, no. 1–2, pp. 76–78, 1996.

[7] D. Sun and X. Yang, "Rapid determination of toxic rhodamine B in food samples using exfoliated graphene-modified electrode," *Food Analytical Methods*, vol. 10, no. 6, pp. 2046–2052, 2017.

[8] J. Zhang, L. Zhang, W. Wang, and Z. Chen, "Sensitive electrochemical determination of rhodamine B based on a silica-pillared zirconium phosphate/nafion composite modified glassy carbon electrode," *Journal of AOAC International*, vol. 99, no. 3, pp. 760–765, 2016.

[9] Y. Yi, H. Sun, G. Zhu, Z. Zhang, and X. Wu, "Sensitive electrochemical determination of rhodamine B based on cyclodextrin-functionalized nanogold/hollow carbon nanospheres," *Analytical Methods*, vol. 7, no. 12, pp. 4965–4970, 2015.

[10] P. M. Usov, C. McDonnell-Worth, F. Zhou, D. R. MacFarlane, and D. M. D'Alessandro, "The electrochemical transformation of the zeolitic imidazolate framework ZIF-67 in aqueous electrolytes," *Electrochimica Acta*, vol. 153, pp. 433–438, 2015.

[11] L. Yang, L. Yu, M. Sun, and C. Gao, "Zeolitic imidazole framework-67 as an efficient heterogeneous catalyst for the synthesis of ethyl methyl carbonate," *Catalysis Communications*, vol. 54, pp. 86–90, 2014.

[12] W. S. Hummers and R. E. Offeman, "Preparation of Graphitic Oxide," *Journal of the American Chemical Society*, vol. 80, no. 6, article 1339, 1958.

[13] J. Qian, F. Sun, and L. Qin, "Hydrothermal synthesis of zeolitic imidazolate framework-67 (ZIF-67) nanocrystals," *Materials Letters*, vol. 82, no. 55, pp. 220–223, 2012.

[14] J. Soleymani, M. Hasanzadeh, N. Shadjou et al., "A new kinetic-mechanistic approach to elucidate electrooxidation of doxorubicin hydrochloride in unprocessed human fluids using magnetic graphene based nanocomposite modified glassy carbon electrode," *Materials Science and Engineering: C*, vol. 61, pp. 638–650, 2016.

[15] M. Zhang and M. Jia, "High rate capability and long cycle stability Fe3O4–graphene nanocomposite as anode material for lithium ion batteries," *Journal of Alloys and Compounds*, vol. 551, pp. 53–60, 2013.

[16] X. Guo, T. Xing, Y. Lou, and J. Chen, "Controlling ZIF-67 crystals formation through various cobalt sources in aqueous solution," *Journal of Solid State Chemistry*, vol. 235, pp. 107–112, 2016.

[17] Y. Hu, X. Song, Q. Zheng, J. Wang, and J. Pei, "Zeolitic imidazolate framework-67 for shape stabilization and enhanced thermal stability of paraffin-based phase change materials," *RSC Advances*, vol. 9, no. 18, pp. 9962–9967, 2019.

[18] G. Bharath, B. S. Latha, E. H. Alsharaeh, P. Prakash, and N. Ponpandian, "Enhanced hydroxyapatite nanorods formation on graphene oxide nanocomposite as a potential candidate for protein adsorption, pH controlled release and an effective drug delivery platform for cancer therapy," *Analytical Methods*, vol. 9, no. 2, pp. 240–252, 2017.

[19] Y. Y. Wang, Z. . Ni, T. Yu et al., "Raman studies of monolayer graphene: the substrate effect," *Journal of Physical Chemistry C*, vol. 112, no. 29, pp. 10637–10640, 2008.

[20] K. Jayaramulu, J. Masa, O. Tomanec et al., "Nanoporous nitrogen-doped graphene oxide/nickel sulfide composite sheets derived from a metal-organic framework as an efficient electrocatalyst for hydrogen and oxygen evolution," *Advanced Functional Materials*, vol. 27, no. 33, article 1700451, 2017.

[21] J. Qin, S. Wang, and X. Wang, "Visible-light reduction CO2 with dodecahedral zeolitic imidazolate framework ZIF-67 as an efficient co-catalyst," *Applied Catalysis B: Environmental*, vol. 209, pp. 476–482, 2017.

[22] W. Wei, W. Chen, and D. G. Ivey, "Rock salt-spinel structural transformation in anodically electrodeposited Mn-Co-O nanocrystals," *Chemistry of Materials*, vol. 20, no. 5, pp. 1941–1947, 2008.

[23] D. Barreca, C. Massignan, S. Daolio et al., "Composition and microstructure of cobalt oxide thin films obtained from a novel cobalt (II) precursor by chemical vapor deposition," *Chemistry of Materials*, vol. 13, no. 2, pp. 588–593, 2001.

[24] D. G. Castner, P. R. Watson, and I. Y. Chan, "X-ray absorption spectroscopy, X-ray photoelectron spectroscopy, and analytical electron microscopy studies of cobalt catalysts. 1. Characterization of calcined catalysts," *The Journal of Physical Chemistry*, vol. 93, no. 8, pp. 3188–3194, 1989.

[25] Y. Yang, H. Dong, Y. Wang, C. He, Y. Wang, and X. Zhang, "Synthesis of octahedral like Cu-BTC derivatives derived from MOF calcined under different atmosphere for application in CO oxidation," *Journal of Solid State Chemistry*, vol. 258, pp. 582–587, 2018.

[26] X. Zhang, H. Li, X. Lv et al., "Facile synthesis of highly efficient amorphous Mn-MIL-100 catalysts: formation mechanism and structure changes during application in CO oxidation," *Chemistry - A European Journal*, vol. 24, no. 35, pp. 8822–8832, 2018.

[27] Y. Chen, B. Song, X. Tang, L. Lu, and J. Xue, "One-step synthesis of hollow porous Fe3O4 beads–reduced graphene oxide composites with superior battery performance," *Journal of Materials Chemistry*, vol. 22, no. 34, article 17656, 2012.

[28] V. Chandra, J. Park, Y. Chun, J. W. Lee, I. C. Hwang, and K. S. Kim, "Water-Dispersible Magnetite-Reduced Graphene Oxide Composites for Arsenic Removal," *ACS Nano*, vol. 4, no. 7, pp. 3979–3986, 2010.

[29] A. M. Bagoji and S. T. Nandibewoor, "Electrocatalytic redox behavior of graphene films towards acebutolol hydrochloride determination in real samples," *New Journal of Chemistry*, vol. 40, no. 4, pp. 3763–3772, 2016.

[30] V. B. Mohan, R. Brown, K. Jayaraman, and D. Bhattacharyya, "Characterisation of reduced graphene oxide: effects of reduction variables on electrical conductivity," *Materials Science and Engineering: B*, vol. 193, no. C, pp. 49–60, 2015.

[31] A. J. Bard and L. J. Falkner, *Electrochemical methods, fundamentals and applications*, vol. 60, no. 1, 20012ed., Wiley, 2001.

[32] E. Laviron, "General expression of the linear potential sweep voltammogram in the case of diffusionless electrochemical systems," *Journal of Electroanalytical Chemistry*, vol. 101, no. 1, pp. 19–28, 1979.

[33] C. Li, "Electrochemical determination of dipyridamole at a carbon paste electrode using cetyltrimethyl ammonium bromide as enhancing element," *Colloids and Surfaces B: Biointerfaces*, vol. 55, no. 1, pp. 77–83, 2007.

[34] I. Taverniers, M. de Loose, and E. van Bockstaele, "Trends in quality in the analytical laboratory. II. Analytical method validation and quality assurance," *TrAC Trends in Analytical Chemistry*, vol. 23, no. 8, pp. 535–552, 2004.

[35] J. Sun, T. Gan, Y. Li, Z. Shi, and Y. Liu, "Rapid and sensitive strategy for Rhodamine B detection using a novel electrochemical platform based on core-shell structured Cu@carbon sphere nanohybrid," *Journal of Electroanalytical Chemistry*, vol. 724, pp. 87–94, 2014.

[36] L. Yu, Y. Mao, and L. Qu, "Simple voltammetric determination of rhodamine B by using the glassy carbon electrode in fruit juice and preserved fruit," *Food Analytical Methods*, vol. 6, no. 6, pp. 1665–1670, 2013.

Hindawi
Journal of Nanomaterials
Volume 2020, Article ID 1523164, 14 pages
https://doi.org/10.1155/2020/1523164

Research Article

Synthesis of C-N-S-Tridoped TiO_2 from Vietnam Ilmenite Ore and Its Visible Light-Driven-Photocatalytic Activity for Tetracyline Degradation

Nguyen Thi Lan,[1] Vo Hoang Anh,[1] Hoang Duc An,[1] Nguyen Phi Hung,[1] Dao Ngoc Nhiem,[2] Bui Van Thang,[3] Pham Khac Lieu,[4] and Dinh Quang Khieu[5]

[1]*Qui Nhon University, 550000, Vietnam*
[2]*Institute of Materials Science, VAST, 10000, Vietnam*
[3]*Dong Thap University, 81000, Vietnam*
[4]*Hue University, 49000, Vietnam*
[5]*University of Sciences, Hue University, 49000, Vietnam*

Correspondence should be addressed to Nguyen Phi Hung; nguyenphihung@qnu.edu.vn and Dinh Quang Khieu; dqkhieu@hueuni.edu.vn

Received 3 January 2020; Revised 18 February 2020; Accepted 24 February 2020; Published 16 March 2020

Guest Editor: Yong Hu

In this study, C-N-S-tridoped TiO_2 composite was fabricated from TiO_2 prepared from ilmenite ore and thiourea by means of hydrothermal method. The obtained material was characterized by X-ray diffraction, Raman scattering spectroscopy, UV-Vis diffuse reflectance spectroscopy, nitrogen adsorption-desorption isotherms, scanning electron microscopy (SEM), transmission electron microscopy (TEM), and X-ray photoelectron spectroscopy (XPS). It was found that C-N-S-tridoped TiO_2 material has a large specific surface area, showing good photocatalytic activity on the degradation of antibiotic tetracycline in visible light region. The study on the mechanism of tetracycline photodegradation using the liquid chromatography with mass spectrometry was performed. It was found that tetracycline has been degraded over C-N-S-tridoped TiO_2 catalyst into many different intermediates which can eventually be converted into CO_2 and H_2O. The kinetics of photocatalytic decomposition of tetracycline were investigated. In addition, the obtained material could catalyze well the degradation of other antibiotics (ciprofloxacin and chloramphenicol) and dyes (rhodamine-B, methylene blue, and organe red). The catalyst was stable after five recycles with slight loss of catalytic activity, which indicates great potential for practical application of C-N-S-tridoped TiO_2 catalyst in treatment of wastewater containing tetracycline in particular or antibiotics in general.

1. Introduction

Tetracycline (denoted as TC) is one of the widely used antibiotics in veterinary medicine and aquaculture [1]. Due to poor absorption, most of them are not metabolized and excreted in the faces and urine as the original compounds. Tetracycline is usually detected at a concentration of 0.07-1.34 μg/L in surface water samples. The most dangerous effect of antibiotics in the environment is to create favorable conditions for the development of resistant strains of bacteria and cause the current phenomenon of antibiotic resistance [2]. Therefore, the elimination of tetracycline should be of considerable concern. Most of the amount of tetracycline detected in surface water, drinking water, and mud is due to the ineffective elimination of traditional and biological methods [1, 3]. In order to reduce the amount of tetracycline released into the environment, new treatment methods need to be developed. Advanced oxidation processes (AOPs) such as photochemical processes [1, 3], ozonation [4], ultrasonic waves [5], and Fenton processes [6] are considered as effective technologies to decompose antibiotic pollutants in aqueous solution. Among the AOPs, photocatalytic process based on titanium dioxide is one of the most promising technologies. TiO_2, with the preeminent properties, such as high

photocatalytic activity and super wetting, is very durable and nontoxic and has high reserves; it has been studied and applied widely [7]. However, with a band gap of about 3.2-3.5 eV, TiO_2 material can only give a catalytic effect in the ultraviolet (UV) light region. The portion of UV radiation in the solar spectrum to the earth's surface is only about 5%, so the use of this source of radiation for TiO_2 photocatalytic treatment is limited. In order to expand the use of solar radiation energy in the visible light area into the photocatalytic reaction, it is necessary to reduce the band gap energy of TiO_2 or shift the light absorption of TiO_2 from the UV to the visible region. Many studies have suggested that TiO_2 doped with nonmetal elements such as C, F, N, and S can extend the absorption spectrum to the visible light region [8–11].

Recently, the simultaneous doping of two or three nonmetals as a promising strategy to increase the photocatalytic activity of TiO_2 in the visible region exhibits higher photocatalytic activity than that of TiO_2 doping an element [12]. Zhou and Yu [13] reported that TiO_2 crystals simultaneously modified C, N, and S by solid phase reaction exhibited high photocatalytic activity for formaldehyde decomposition in visible light region. Ao et al. [14] prepared the C-N-S-tridoped TiO_2 through sol-gel method combined with surfactant cetyltrimethylammonium bromide (CTAB) as a soft template. Photocatalytic activity is assessed by the decomposition of Reactive Dyes Brilliant Red X-3B in aqueous solution. Wang et al. [15] prepared C-N-S-doped TiO_2 nanocrystals by hydrothermal method in the presence of TiO_2 and L-cysteine biological molecule. L-cysteine not only provided a source of carbon, sulfur, and nitrogen, but also controlled the final product of crystalline and morphological phases. The high activity of this catalyst in visible region is due to the synergic effect of the large surface area, the red shift at the absorption edge, the strong absorption in the visible light zone, and the phase structure mixture of the material.

In the present study, TiO_2 was prepared from ilmenite ore by using sulfuric acid method, then doping of C, N, and S elements into TiO_2 was performed through the hydrothermal process of TiO_2 and thiourea. Photocatalytic decomposition reaction in the visible region of tetracycline on C-N-S-tridoped TiO_2 composite was investigated.

2. Experimental

2.1. Materials and Synthesis. Ilmenite ore was provided kindly by the Binh Dinh company (Vietnam). The chemical composition analyzed by Atomic Absorption Spectroscopy (AAS) was listed in Table 1.

Sulfuric acid (H_2SO_4, 98%), thiourea (CH_4N_2S, 99%), methylene blue ($C_{16}H_{18}N_3SCl$, 99%), and organe red ($C_{16}H_{11}N_2NaO_4S$, 99%) were purchased from the Factory Co., Ltd. (China); rhodamine-B ($C_{28}H_{31}ClN_2O_3$, Merck, 99%), tetracycline hydrochloride ($C_{22}H_{24}O_8N_2{\cdot}HCl$, 96.09%), ciprofloxacin hydrochloride ($C_{17}H_{18}FN_3O_3{\cdot}HCl$ 94.73%), and chloramphenicol ($C_{11}H_{12}Cl_2N_2O_5$, 99.62%) were obtained from the Drug Testing Institute in Ho Chi Minh city (Vietnam).

Table 1: The chemical composition of ilmenite.

Composition	TiO_2	FeO	Fe_2O_3	SiO_2	Other impurities
Wt%	49.54	32.69	11.21	0.21	6.35

2.1.1. Synthesis of $TiOSO_4$ Material from Ilmenite Ore. Add 137.88 mL sulfuric acid solution (90%) to a 500 mL heat-resistant flask containing 50 grams of ilmenite ore. The mixture was heated for 1 hour with stirring at 200-210°C on a sand bath and then add 380 mL of 0.005 M H_2SO_4 under magnetic stirring for 3 hours at 70°C. Let the mixture settle for about 8 hours and remove the solid phase. Add 7.6 grams of iron billet to the obtained liquid for reducing Fe^{3+} to Fe^{2+} [16, 17]. This solution was concentrated until scum formation. Then cool the solution at a temperature of about -2°C to -5°C for 8 hours. The precipitate was separated, and $TiOSO_4$ solution was obtained.

2.1.2. Synthesis of C-N-S-Tridoped TiO_2 Materials. Take 2.27 grams of $TiOSO_4$ and a defined amount of thiourea (with molar ratio of thiourea: TiO_2 = 2 : 1) into a teflon flask, then dissolve with distilled water. Put the teflon bottle in the autoclave at 180°C for 12 hours. After the hydrothermal process, the autoclave was naturally cooled to room temperature. Filter the white precipitate and wash several times with distilled water until the filtrate has a constant pH. The product is dried and calcined at 400-700°C for 1 hour to obtain the C-N-S-tridoped TiO_2 (denoted as TH-TiO_2-a (a = 400, 500, 600, and 700°C). TiO_2 samples were also prepared as the abovementioned procedure but without adding thiourea.

2.2. Catalytic Activity. The catalytic activity of TiO_2 or TH-TiO_2 was estimated through the decomposition of tetracycline (30 mg/L) and the catalytic mass (0.6 g/L). The mixture was stirred in the dark for 30 minutes to reach the absorption/desorption equilibrium, then illuminated with a 60 W filament lamp (filter cutoff $\lambda < 420$ nm). The remaining tetracycline concentration was determined by HPLC-UV method on Thermo Scientific series 3300 HPLC (Thermo Scientific Technologies, CA, USA) (λ_{max} = 355 nm).

2.3. Methods of Analysis. The X-ray diffraction (XRD) was conducted in D8-Advance 5005 with Cu Kα λ = 0.154 nm. The element composition and oxidation state on the catalyst surface in the sample were determined by X-ray electron spectroscopy (XPS) (ESCALAB 250-Thermo VG, UK). The morphology and the element composition were measured by using scanning electron microscope (SEM) with energy dispersive X-ray spectroscopy (EDX) (Nova Nano SEM 450) and transmission electron microscopy (TEM) (JEOL JEM 1010). The photoluminescence (PL) was measured using a Hitachi F-7000 spectrophotometer over wavelength range of 375–600 nm with a 150 W xenon lamp. Raman spectrum and UV-Vis-DR were conducted by using T64000 Raman with 633 nm and GBC Instrument-2885, respectively. Textural properties of material samples were characterized by nitrogen adsorption/desorption isotherms method using Micromeritics ASAP 2000. The intermediates that appear

during tetracycline decomposition are determined by LC/MSD-Trap-SL method in combination with ESI method ionized mass spectrometry on Agilent. The mineralization of tetracycline in the photocatalytic degradation was monitored with TOC analyzer (Jena multi N/C 2100, Germany).

3. Results and Discussion

3.1. Characterization of Materials. The physical chemistry characterizations of TH-TiO_2 materials calcined at different temperature are presented in Figure S1–4 and Table S1. The primary experiments show that the TH-TiO_2 calcined at 500°C provided the highest photocatalytic activity (Figure S5). Therefore, the only discussion of TH-TiO_2 calcined at 500°C was focused in this text. The obtained materials were studied by XRD measurements (Figure 1). The diffractions of TiO_2 and TH-TiO_2 are observed at the same Bragg-angle and indexed as (101), (004), (200), (105), (211), (204), (116), (220), and (215) of the anatase phase [12, 18], indicating that the titanium oxide in anatase form is the main phase in the obtained samples. However, TH-TiO_2 prepared from hydrothermal process of TiO (SO_4) and thiourea possesses the lower intensities of anatase peaks compared to TiO_2 from hydrothermal process of only TiO (SO_4). The crystallite sizes of the samples could be estimated from the broadening of the X-ray diffraction peak according to Scherrer formula [19]. It was calculated that TiO_2 has an average crystallite size of 14.39 nm, and it decreases to 9.54 nm for TH-TiO_2 indicated that the tridoping of C, N, and S suppressed grain growth.

Raman spectrum (Figure 2) shows only the existence of 4 spectral bands at 144 cm^{-1}, 399 cm^{-1}, 399 cm^{-1}, 519 cm^{-1}, and 639 cm^{-1}, indicating that both TH-TiO_2 and TiO_2 have only anatase phase [20]. The peaks at 144 cm^{-1} (E_g) and 639 cm^{-1} (E_g) are related to the symmetrical stretching of the O-Ti-O bond in TiO_2 while the peak of 399 cm^{-1} (B1g) corresponds to the bending oscillation of the O-Ti-O bond, and 513 cm^{-1} (A1g) could be attributed to the asymmetric bending vibration of the O-Ti-O bond [21]. This result is consistent with XRD analysis.

The products prepared from ilmenite ore are expected to contain a certain amount of iron element. The element composition was investigated by EDX spectrum (Figure S6 and 7). It was found that the main elements in TiO_2 were Ti and O, and TH-TiO_2 were Ti, C, O, N, and S. It was notable that iron element was not detected in TiO_2 or TH-TiO_2 by XPS or EDX, this refuses the effect of iron oxide residue on catalytic activity of TiO_2 and TH-TiO_2.

The oxidation states of C, N, and S in TH-TiO_2 were studied by XPS spectra (Figure 3). The survey XPS spectrum (Figure 3(a)) presents Ti2p peaked at 459.36 eV, C1s at 284.70 eV, O1s at 531.00 eV, N1s at 400.30 eV, and S2p at 168.01 eV. The XPS level core spectrum of C1s (Figure 3(b)) shows a strong peak at 284.70 eV corresponding to the elemental carbon (graphite) that is formed by incomplete combustion of organic compounds under hydrothermal conditions. The spectral shoulders at 289.00 eV are associated with the presence of C=O bond of carbonate radicals on the catalytic surface [20]. According to the XPS spectrum at 286.2 eV, there was a replacement of some Ti atoms by C in lattice and forming Ti-O-C structure [18, 22]. The peak at 281 eV of the Ti-C bond was not found, indicating that C atom does not replace oxygen atoms in the TiO_2 lattice [23].

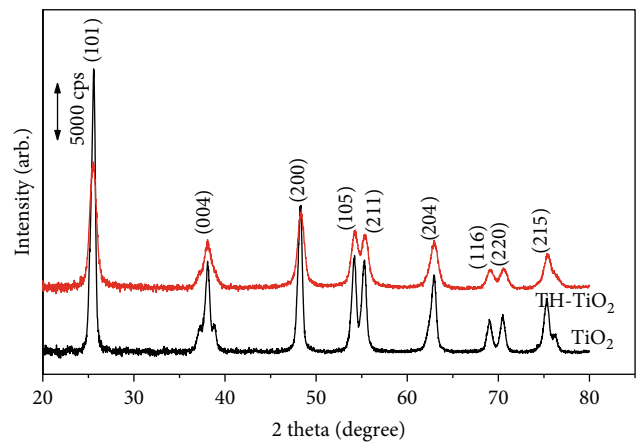

Figure 1: XRD patterns of TiO_2 and TH-TiO_2 samples.

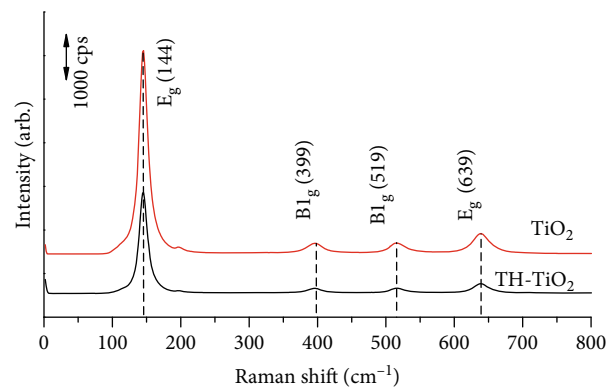

Figure 2: Raman spectra of TiO_2 and TH-TiO_2.

XPS core level spectrum of S2p (Figure 3(c)) with peaks at 168.7 and 169.50 eV corresponding to S^{6+} is replaced by Ti^{4+} [24–26]. No peak presenting for Ti-S links was found around 160-163 eV. This result is consistent with some previous studies which suggested that S^{+6} replacing Ti^{4+} in lattice is easier than replacing O^{2-} with S^{2-}[24, 27, 28]. This substitution also contributes to reducing the band gap energy of TiO_2 by introducing the interband gaps and lowering conduction band. The XPS core level spectrum of N1s (Figure 3(d)) shows that a wide maximum range of 399-401 eV corresponding to the replacement of N into oxygen position in TiO_2 network [29, 30] has contributed to increasing the valence band. Therefore, the band gap energy of TiO_2 decreases with nitrogen doping. The results of XPS analysis showed that carbon, nitrogen, and sulfur were added to the TiO_2 catalyst and their electronic structures change.

The UV-Vis diffuse reflectance spectroscopy (UV-Vis-DRS) is a useful technique to characterize the band gap energy of photocatalytic materials. In the present study, TC

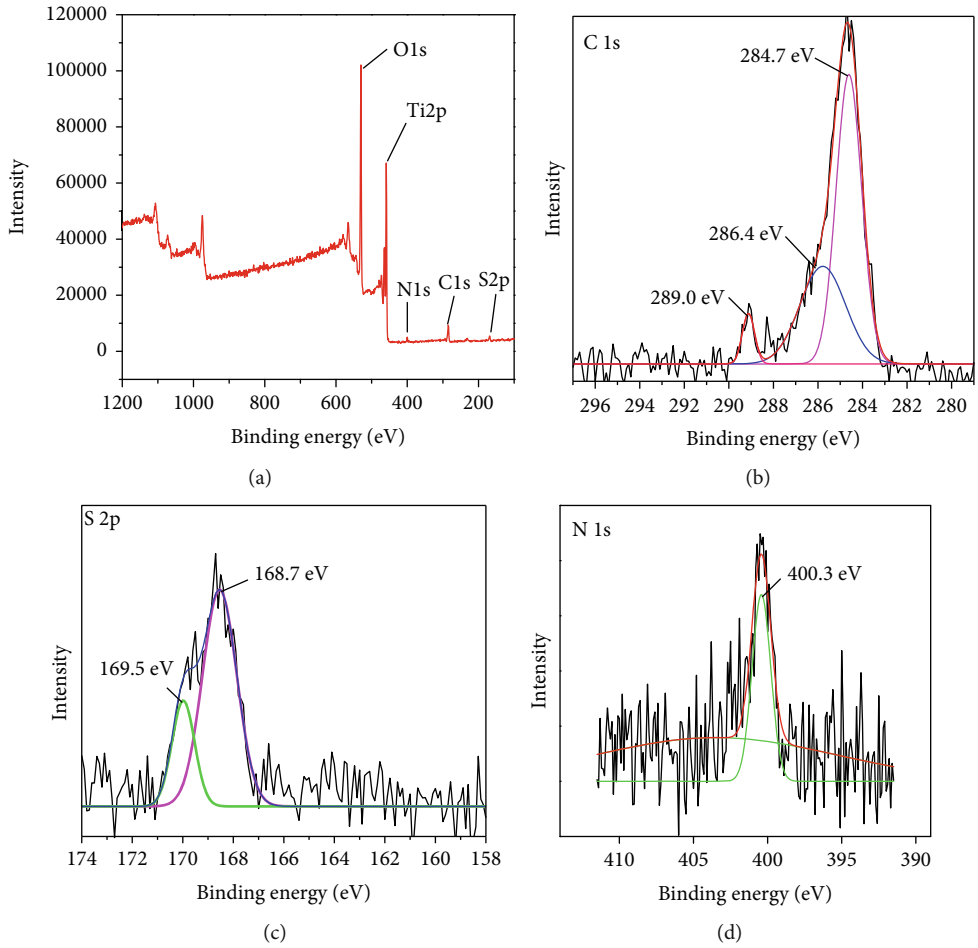

Figure 3: XPS spectrum of survey (a), C1p (b), S2p (c), and N1s (d) in sample TH-TiO_2.

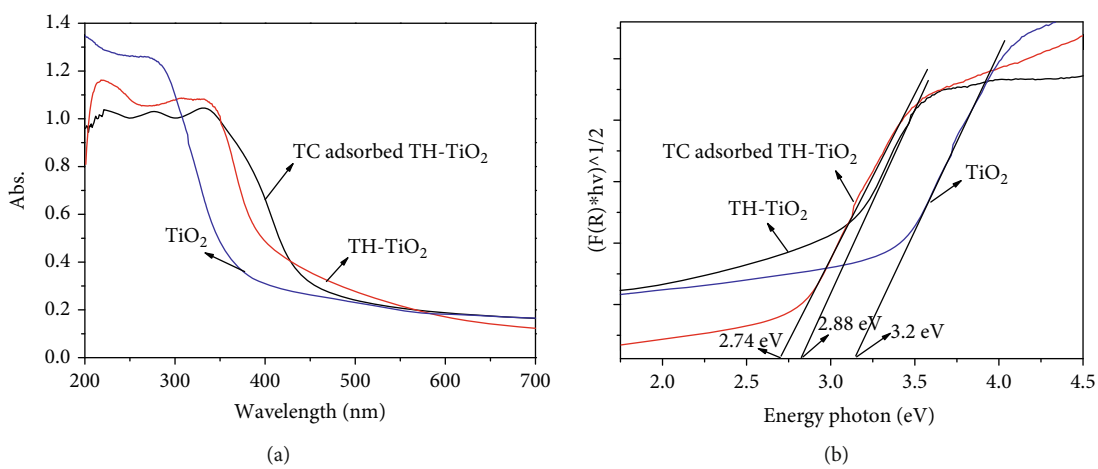

Figure 4: UV-Vis-DRS spectra (a) and the plot of Kubelka-Munk function for TiO_2, TC-adsorbed TH-TiO_2, and TH-TiO_2 (b).

adsorption of TH-TiO_2 in the dark was conducted; therefore, TH-TiO_2 adsorbing tetracycline at equilibrium (TC adsorbed TH-TiO_2), along with TiO_2 and TH-TiO_2, was characterized by means of UV-Vis-DRS. As can be seen from the figure, TH-TiO_2 sample had an absorption band shifting to higher wavelength compared with TiO_2. The band gap energy of TiO_2, TH-TiO_2, and TC-adsorbed TH-TiO_2 samples calculated by Kubelka-Munk function is 3.20, 2.88, and 2.74 eV, respectively (Figure 4(b)).

The red shift is thought to be C, N, and S doping to TiO_2 matrix, narrowing the band gap energy of the TiO_2 due to the occurrence of the hybridized states located in the band gap [31] or tetracyine as photosensitizer. The photoluminescence (PL) is widely used to study the recombination of photo-

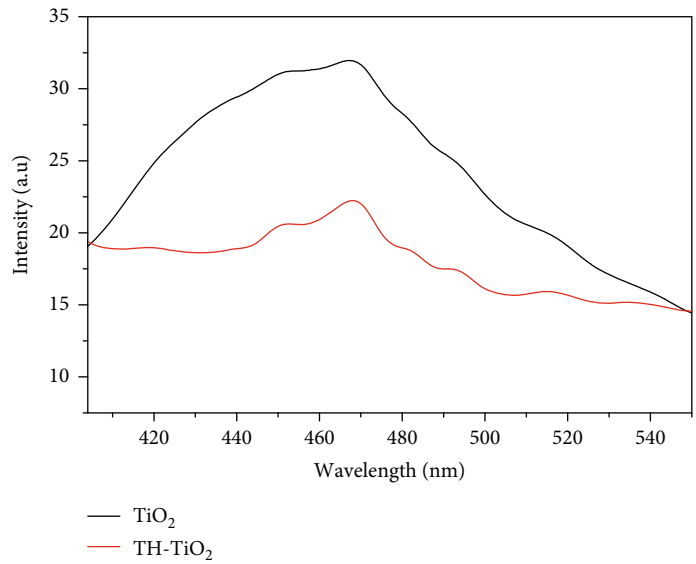

Figure 5: PL spectra of TiO_2 and TH-TiO_2.

induced electron/hole pairs. The PL spectra of TiO_2 and TH-TiO_2 materials are shown in Figure 5. The materials were excited at 404 nm with a strong emission peak at about 468 nm. It was found that there is a significant decrease in luminescence intensity of TH-TiO_2 compared to TiO_2. This demonstrates that the doping of C, N, and S into TiO_2 significantly improved the separation of photo-induced electrons, creating favorable conditions for reacting photo-generated holes and electrons with H_2O or oxygen to active radicals [23, 32].

From SEM images shown in Figures 6(a) and 6(b), it is observable that both of the pure and doped TiO_2 samples perform similar morphology which includes secondary particles with size varying from 500 to 600 nm constructed from primary subparticles. The only difference, however, could be observed is that, compared to pure sample, TH-TiO_2 exhibits significantly rougher surface with higher porosity (as clearly seen in the consistent insets) which could be related to the gas formation due to decomposition of thiourea during synthesis condition. The construction of secondary particles from subone could be clarified in HR-TEM images (as shown in Figure 6(c)) which indicates that the size range of the primary particles is around 12 to 18 nm. The high magnification TEM image in Figure 6(d) displays the observable lattice fringe corresponding to (101) plane with distance of 0.352 nm which is confirmed by Fast Fourier Transforms (FFT) (insets). The acceptable crystallinity of obtained sample was further proved via Selected Area Electron Diffraction (SAED) (Figure 6(e)) which includes separated rings formed form clear spot. The corresponding lattice planes were also indexed in SAED pattern.

The textural properties of the obtained materials were investigated by means of nitrogen adsorption/desorption isotherms (Figure 7). The curves of both materials belong to type V with type H1 loops according to the IUPAC classification which are all characterized for the mesoporous structure formed by intersecting particles [33, 34]. The pore size curves exhibit the normal distribution with average sizes of 36.7 nm for TiO_2 and 13.8 nm for TH-TiO_2 (the inset of Figure 7). The doping of C, N, and S elements into TiO_2 matrix enhanced the specific surface area (the values of 36 $m^2 \cdot g^{-1}$ for TiO_2 and 74 $m^2.g^{-1}$ for TH-TiO_2 as calculated by BET model) and reduced also the pore size of TH-TiO_2.

3.2. Catalytic Activity. Some reports present that some natural minerals containing TiO shows photocatalytic activity in advanced oxidation process [35, 36]; therefore, the present raw ilmenite was conducted to test photocatalytic activity as a reference. Figure 8(a) presents the kinetics of TC degradation over TiO_2, raw ilmenite, and TH-TiO_2. As can be seen in the figure, ilmenite does not exhibit any photocatalytic activity toward to oxidize TC due to the chemical inert property of ilmenite mineral. For TH-TiO_2, the dark adsorption/desorption equilibrium is reached after 30 min, and it displays higher adsorption capacity than TiO_2 around 10% ($F = 14.69\%$ for TiO_2 and 24.63% for TH-TiO_2 in which $F = 100 \times C_t/C_0$, where C_0 and C_t are the initial concentration and at time t). It is worth noting that TH-TiO_2 yields a degradation efficiency of nearly 100% while TiO_2 yields only 50% after 120 min of visible light illumination. This may be due to larger surface area of TH-TiO_2 which increases the number of active sites for TC to adsorb and decompose. In the leaching experiment, the catalyst was filtered after 30 min, and the degradation of TC under illumination almost stops (Figure 8(a)). In addition, the degradation of TC without the catalyst is not observed after 120 min of illumination, revealing that TC is not photo-decomposed in the present condition. Therefore, it can be suggested that TH-TiO_2 acts as a heterogeneous catalyst in the TC photocatalytic degradation.

Figure 8(b) shows the UV-Vis spectra of TC solution during the photocatalytic degradation using visible light source. Two absorption bands peaked at 270 nm and 355 nm are observed. The former band is assigned to $\pi - \pi^*$

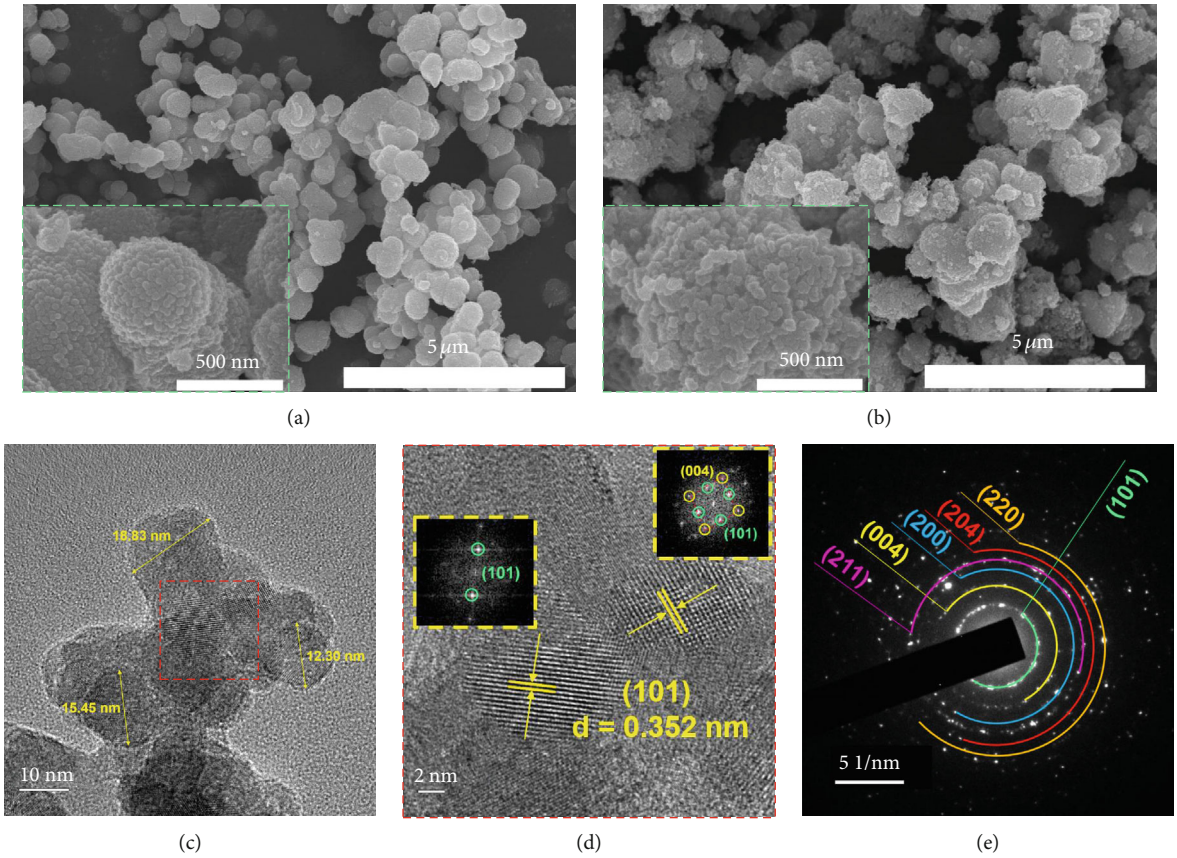

Figure 6: SEM images of (a) TiO_2, (b) TH-TiO_2 samples, (c, d) HR-TEM images with consistent Fast Fourier Transform (FFT) in insets, and (e) Selected Area Electron Diffraction (SAED) of TH-TiO_2.

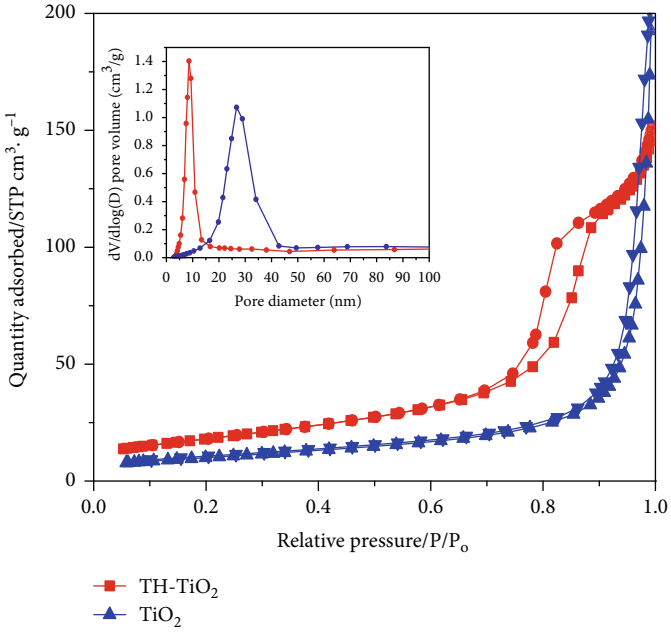

Figure 7: Nitrogen adsorption-desorption isotherms at 77 K; the inset presents pore size distribution of TiO_2 and TH-TiO_2.

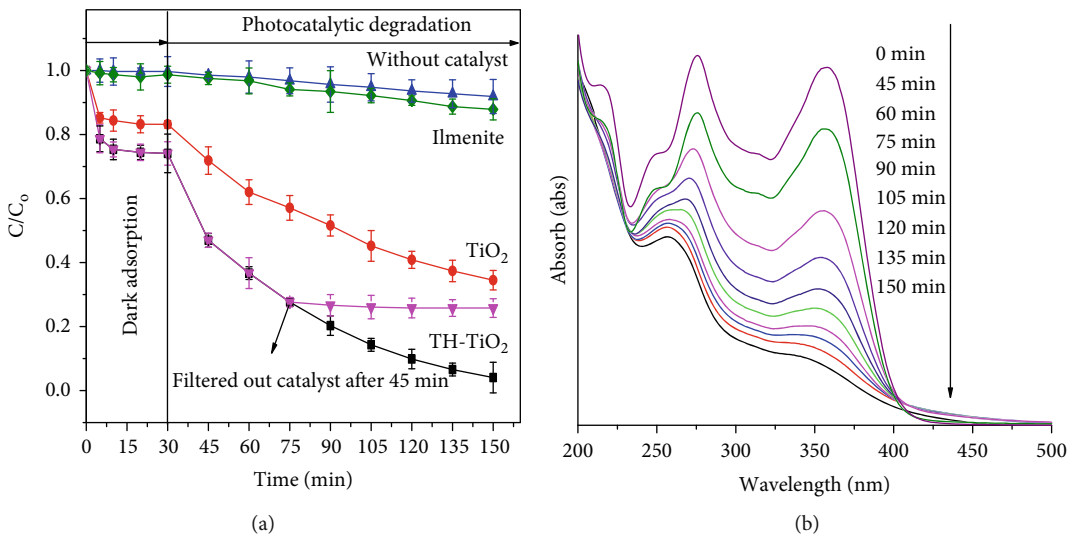

Figure 8: (a) Decolorization kinetics of TC over TiO_2 and TH-TiO_2 under visible light irradiation (conditions: $m_{catalyst} = 0.6\,g \cdot L^{-1}$; concentration of TC = 30 ppm; adsorption time = 30 min). (b) UV-Vis spectra of TC during irradiation time.

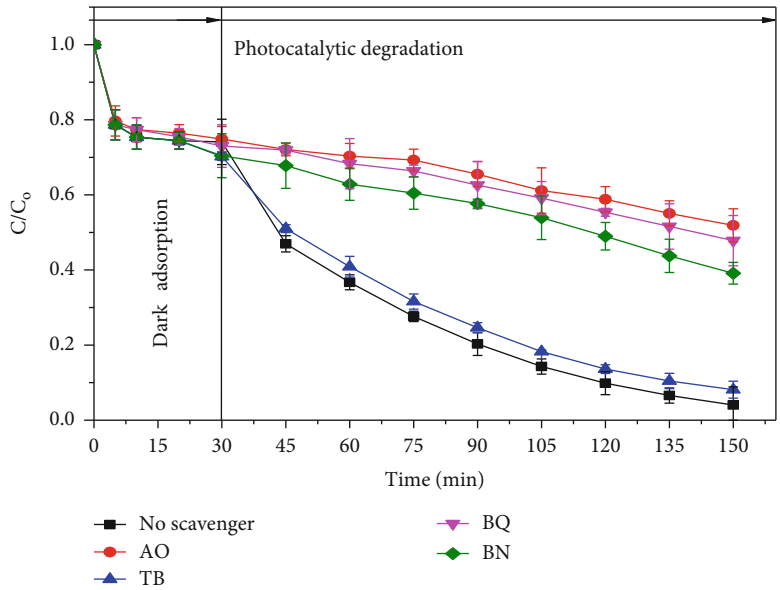

Figure 9: Kinetics of TC degradation on TH-TiO_2 in the presence of different scavengers.

transitions in benzene ring, and the latter is contributed to the conjugated double bonds. The decomposition of TC on TH-TiO_2 catalyst takes place quite quickly, after about 120 minutes of processing, the characteristic absorption peak of TC at 355 nm is almost disappeared. This result shows that TC decomposition has possible formed intermediates with smaller molecular masses.

It is well-known that free radicals such as photo-induced electrons and holes, $^{\bullet}OH$ and $O_2^{(\bullet-)}$, play a critical role in the degradation reactions of organic compounds. In particular, *tert*-butylic alcohol (TB) is used as a quencher for $^{\bullet}OH$ [37], 1,4-benzoquinon- (BQ-) quencher for $O_2^{(\bullet-)}$ [38, 39], ammonium oxalate- (AO-) quencher for H^+ [37, 39], and silver nitrate- (BN-) quencher for photosynthetic electrons e^- [40]. The 2 mL of 10 mM quenching solutions was added just after 30 min of dark adsorption. The effect of extinguishing agents on TC degradation performance is shown in Figure 9. In general, the presence of free radicals reduces the efficiency of TC degradation. AO (quenching h^+), BQ (quenching $O_2^{(\bullet-)}$), and BN (quenching e^-) reduce significantly the degradation rate of TC. However, TB seems not to affect TC degradation. This concludes that the free radicals (h^+; $O_2^{(\bullet-)}$; e^-) take mainly part in degradation reactions of TC while $^{\bullet}OH$ is negligible.

The tridoping of C, N, and S elements into TiO_2 lattice gives to rise new sublevels including S2p and C1s levels under Ti3d conduction band (CB); N2p level above the O2p valence band (VB) [41]. The sublevels of S2p and C1s served as trapping centers for photo-induced electrons that enhance the life times of the charge carriers due to the separation of

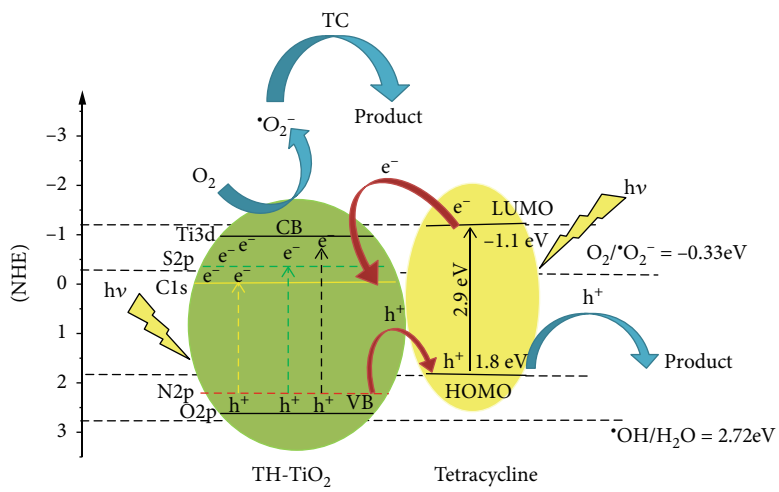

Scheme 1: The mechanisms of charge carrier migration and free radicals formation on TH-TiO_2 catalyst under visible light illumination.

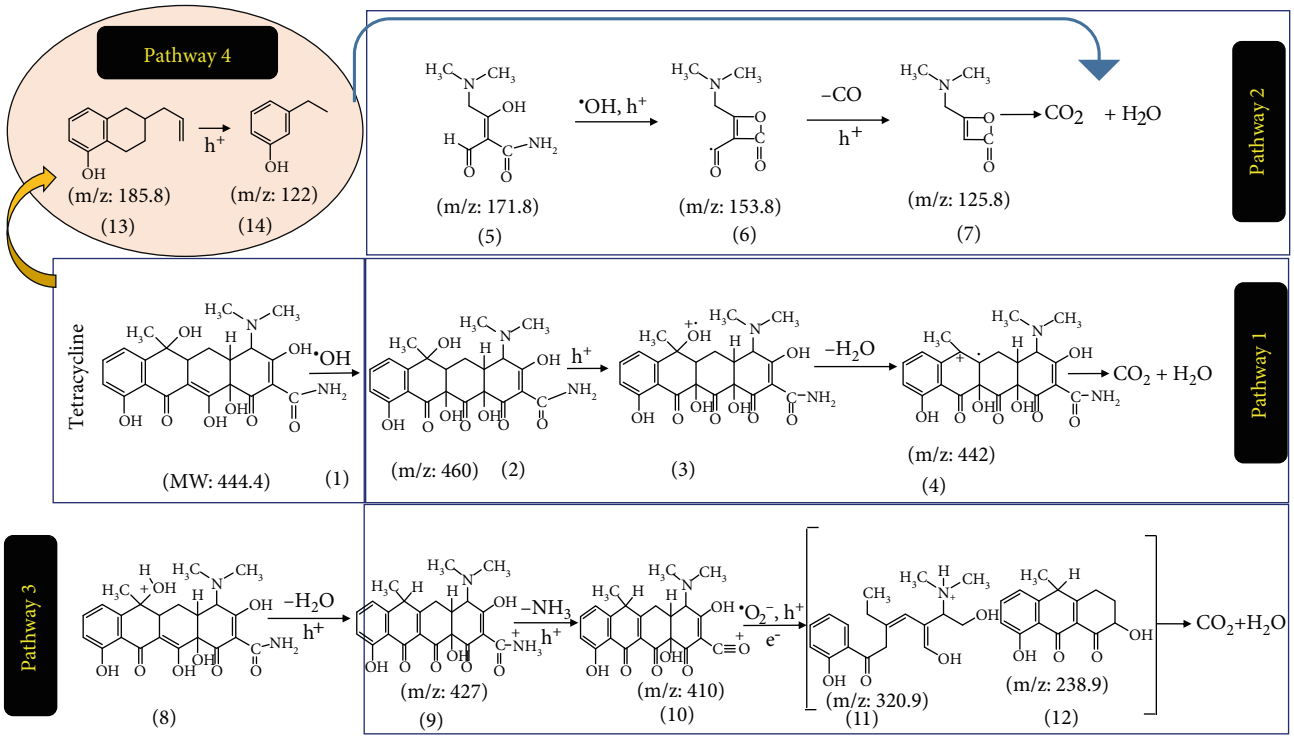

Scheme 2: The possible photocatalytic degradation pathways of TC on TH-TiO_2 catalyst.

hole-electron pairs (Scheme 1). Under visible illumination, TC acts as a photosensitser. TC molecule absorbs light and produces an electron (e^-) and hole (h^+) in LUMO and HOMO regions, respectively. The excited electrons in the LUMO migrated to the CB of the TH-TiO_2 because of the less positive potential of LUMO. E· ($O_2/O_2\bullet^-$, -0.033 eV), hence that photo-induced electrons could react with oxygen to provide $O_2^{\bullet-}$. Similarly, VB band of TH-TiO_2 (2.88 eV) was more positive than the potential of $^\bullet OH/OH^-$ (+2.27 eV), hence the photoinduced electrons are possible to oxidize H_2O to form $^\bullet OH$ radicals. These free radicals are strong oxidizing agent which could oxidize partially or complexly TC. The arguments are illustrated in Scheme 1 and in the following equations:

$$\begin{gathered}
\mathrm{TC} + \mathrm{h}\nu \longrightarrow \mathrm{TC}\left(e_{\mathrm{CB}}^- + h_{\mathrm{VB}}^+\right) \\
\text{Adsorbed TC}\left(e_{\mathrm{CB}}^- + h_{\mathrm{VB}}^+\right) + \mathrm{TH-TiO_2} \longrightarrow \mathrm{TH-TiO_2}\left(e_{\mathrm{CB}}^-\right) + \mathrm{TC}\left(h_{\mathrm{VB}}^+\right) \\
\mathrm{TH-TiO_2}\left(e_{\mathrm{CB}}^-\right) + \text{adsorbed } \mathrm{O_2} \longrightarrow {}^\bullet\mathrm{O_2^-}\ (\text{or}\ {}^\bullet\mathrm{O^-}) + \mathrm{TH-TiO_2} \\
\mathrm{H_2O} \longrightarrow \mathrm{H^+} + \mathrm{OH^-} \\
\mathrm{H_2O} + \mathrm{TH-TiO_2}\left(h_{\mathrm{VB}}^+\right) \longrightarrow \mathrm{H^+} + {}^\bullet\mathrm{OH} \\
{}^\bullet\mathrm{O_2^-}, h^+ \text{ or } {}^\bullet\mathrm{OH} + \text{adsorbed TC/TC}^* \longrightarrow \text{degradation products}
\end{gathered} \tag{1}$$

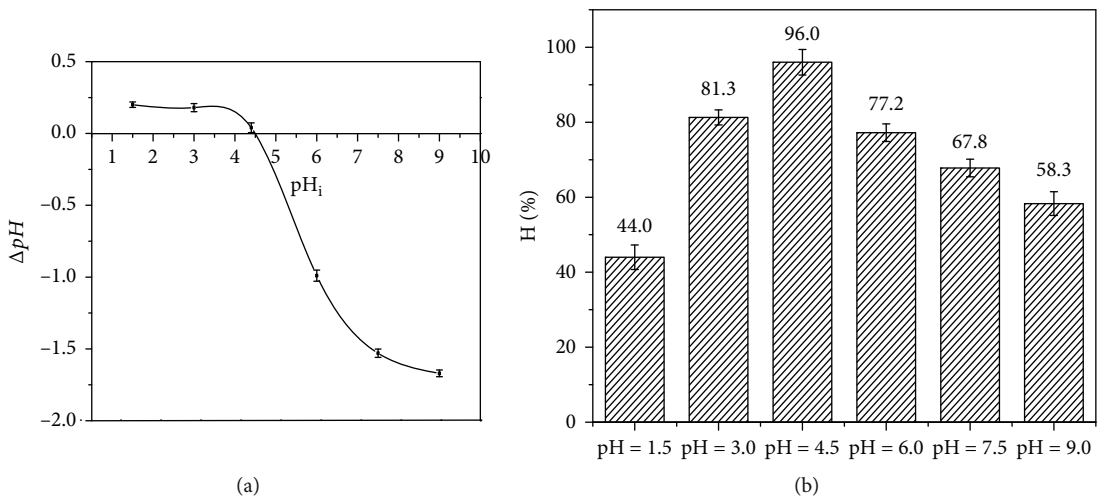

Figure 10: (a) Effect of pH on the TC degradation efficiency. (b) The pH_{PZC} determined by the pH drift method.

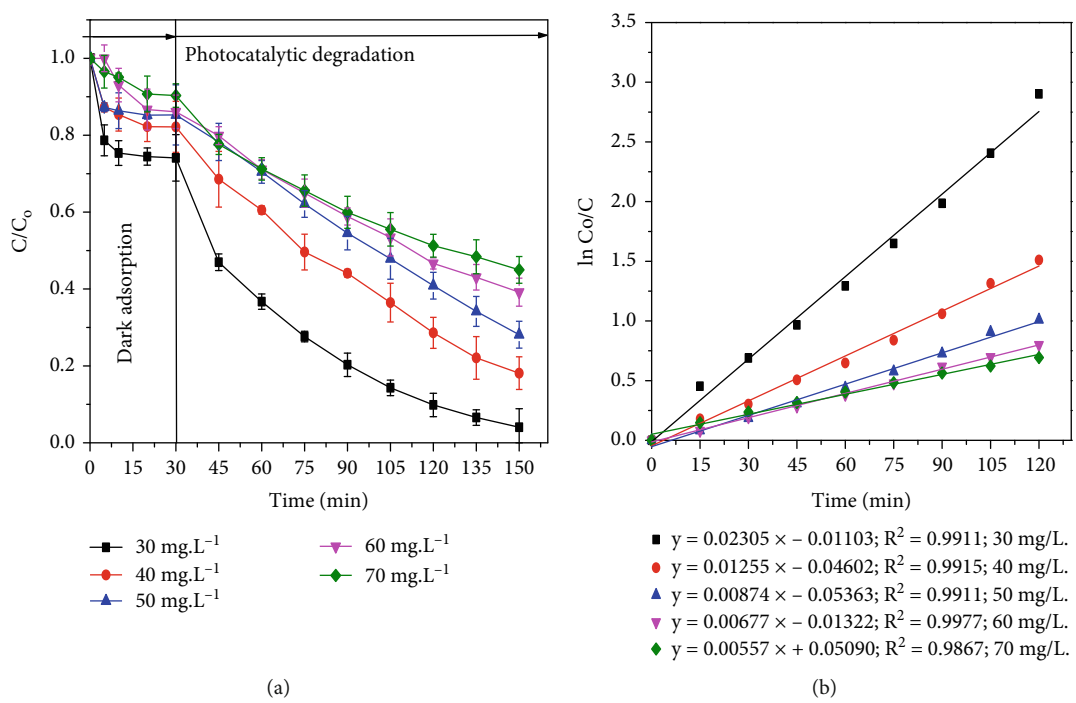

Figure 11: (a) Kinetics of TC decomposition reaction. (b) Plot of Langmuir-Hinshelwood model at different TC initial concentrations.

3.3. LC-MS Analysis. The mechanism of TC photodegradation on TH-TiO_2 catalyst was studied by using the liquid chromatography-mass spectrometry (LC-MS) (see Scheme 2 and Figure S8–10). The LC chromatography was conducted for the solution after reaction time of 30 min followed by mass spectrometry. The finding showed that the intermediates with retention times of 11.9, 16.4, and 30 have m/z values of 460, 427, 171.8, and 185.8, respectively, corresponding to molecular formulae of $C_{22}H_{24}O_9N_2$, $C_{22}H_{23}O_7N_2$, $C_7H_{12}O_3$, and $C_{13}H_{16}O$, respectively. Based on the previous works [42–44], the TC degradation is proposed as follows: initially TC (1) ($m/z = 444.4$) was added with the -OH group in the presence of free radicals $^{\bullet}OH$, and intermediate compound (2) ($m/z = 460$) was further dehydrated in the presence of h^+ to compound (4) ($m/z = 442$). These compounds break down the bonds to form (5), (13), and (14) by the presence of agents $^{\bullet}OH$ and H^+ [45] (Scheme S1).

For pathway 2 (Scheme S2), the ring opening products include compounds (5), (6), and (7), where (5) 4-dimethylamino-2-formyl-3-hydroxybut-2-enamide ($m/z = 171.8$) is formed as a result of direct oxidation from TC (1) or from (4). The presence of 4-((dimethylamino) methyl)-2H-oxet-2-one (7) ($m/z = 125.8$) is due to the internal molecular reaction chain of (5). The reaction mechanism can be described as follows: (step 1) OH (= C-OH) acts as a nucleophile agent, interacting with C = O in the amide function group according to SN2 (CO) mechanism. At the same time, the dehydro group and

Table 2: Comparison of rate constant of the present catalyst with published papers.

Catalyst	Conditions	F^* (%)	Rate constant k (min^{-1})	Ref.
N-TiO_2	(1) Light source: white led, 46 W·m^2 (2) C^o_{TC}: 5 mg·L^{-1} (3) $m_{catalyst}$: 0.3 g·L^{-1} (4) Time for dark adsorption: 45 min (5) Time for photocatalytic degradation: 200 min	74.0	0.012	[49]
N-TiO_2/rGO	(1) Light source: Xenon lamp, 300 W ($\lambda > 400$ nm) (2) C^o_{TC}: 10 mg·L^{-1} (3) $m_{catalyst}$: 1 g·L^{-1} (4) Time for dark adsorption: 30 min (5) Time for photocatalytic degradation: 60 min	98.0	0.057	[50]
Cu-TiO_2	(1) Light source: Xenon lamp, 1000 W ($\lambda > 420$ nm) (2) C^o_{TC}: 20 mg·L^{-1} (3) $m_{catalyst}$: 0.02 g·L^{-1} (4) Time for dark adsorption: 30 min (5) Time for photocatalytic degradation: 240 min	90.0	0.010	[51]
(Mo, C)-TiO_2/FTO	(1) Light source: Xenon lamp, 500 W ($\lambda > 400$ nm) (2) C^o_{TC}: 20 mg·L^{-1} (3) Time for dark adsorption: 60 min (4) Time for photocatalytic degradation: 100 min	89.5	0.022	[52]
$Ti_{0.9}Zr_{0.05}Sn_{0.05}$ O_2	(1) Light source: mercury low pressure lamp, 36 W (2) C^o_{TC}: 30 mg·L^{-1} (3) $m_{catalyst}$: 0.8 g·L^{-1} (4) Time for dark adsorption: 30 min (5) Time for photocatalytic degradation: 180 min	93.0	0.025	[53]
BiOCl/TiO_2/spinel	(1) Light source: Xenon lamp, ($\lambda > 400$ nm) (2) C^o_{TC}: 50 mg·L^{-1} (3) $m_{catalyst}$: 0.6 g·L^{-1} (4) Time for dark adsorption: 60 min (5) Time for photocatalytic degradation: 180 min	92.0	0.004	[54]
TH-TiO_2	(1) Light source: Xenon lamp, 45 W ($\lambda > 400$ nm) (2) C^o_{TC}: 30 mg·L^{-1} (3) $m_{catalyst}$: 0.6 g·L^{-1} (4) Time for dark adsorption: 30 min (5) Time for photocatalytic degradation: 150 min	100	0.023	The present work

* $F = 100 \times (C_o - C_e)/C_o$ where C_o and C_e is the initial and final concentration.

aldehyde reaction also occurs under the action of $^{\bullet}$OH, H. (Step 2) compound (6) is formed unstably because containing single electrons tends to turn into (7) through decarbonylation process. In solution, the –OH (H_3C-C-OH) group of TC with high electron density will give way to H^+, then dehydration process with hydrogen displacement also happens to form a more stable structural compound (9) ($m/z = 427.0$) [46, 47] (Scheme S3). Compounds (11) ($m/z = 320.9$) and (12) ($m/z = 238.9$) are the result of NH_3 splitting and cutting off different bonds due to h^+ and e^-, $O^{2\bullet-}$. However, this process will not be clarified in this study because of the relatively complex mechanism and very short shelf life of intermediate compounds (pathway 3). Finally, compounds (13) and (14) are formed directly from TC or through intermediate compounds (4) (pathway 4). Besides, some compounds with small m/z (116.7, 91) were also found in the analysis process but were not identified because fragmentation data is relatively small. At the same time, the results of LC-ESI-MS analysis and the TOC measurement was subjected to reaction solution. Initial TOC was about 550 mg/L; however, it decreased 92% to 44 mg/L after 150 min treating, indicating the complete mineralization. It is concluded from LC-MS and TOC analysis that TC degradation over TH-TiO_2 catalyst proceeds via many different intermediates and they can eventually be converted into CO_2 and H_2O.

3.4. Kinetic Study. The pH of point of zero charge (pH_{PZC}) of TH-TiO_2 calculated by the pH drift method is 4.5

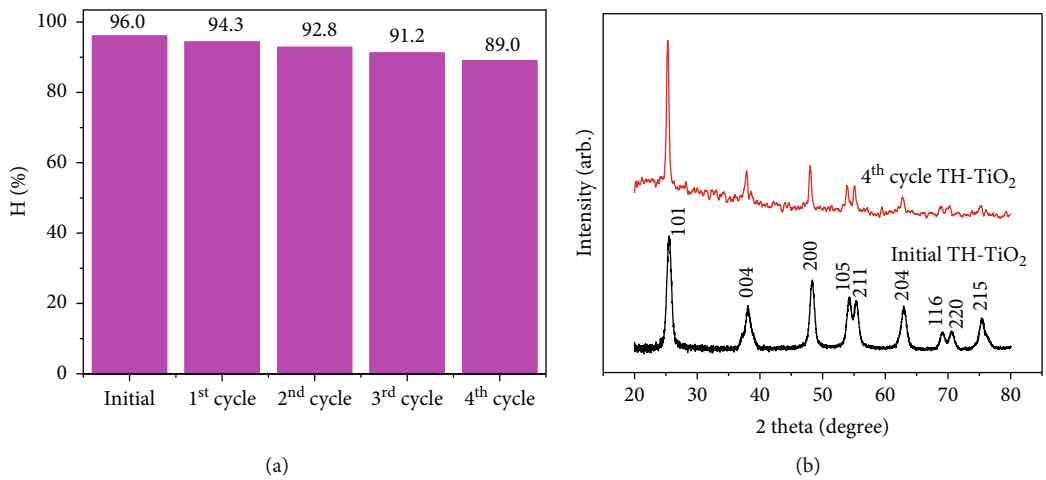

Figure 12: (a) TC degradation efficiency after four reuse cycles of TH-TiO_2. (b) XRD patterns of reused TH-TiO_2.

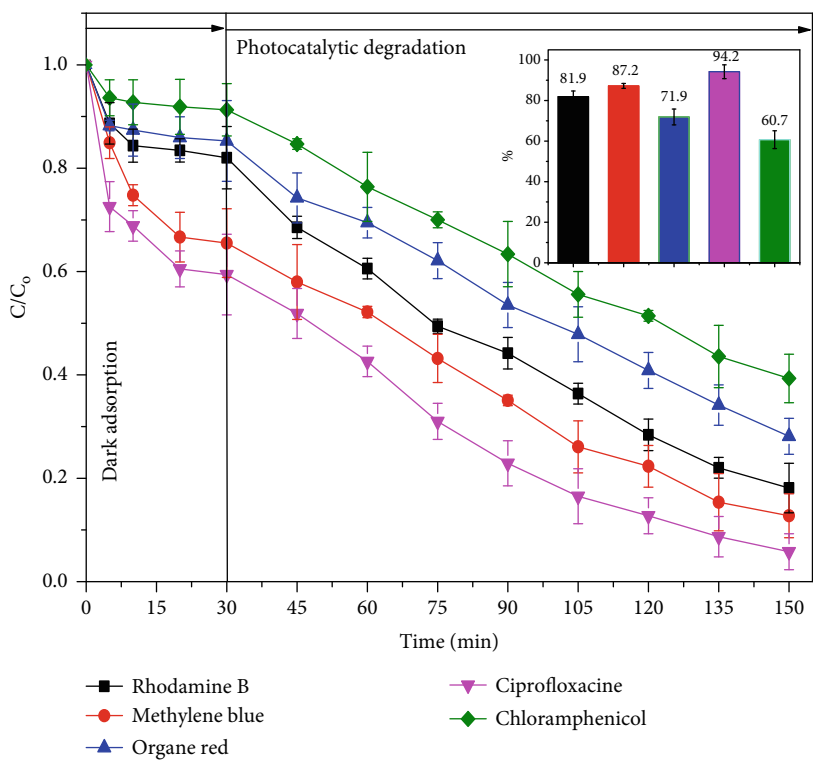

Figure 13: Kinetics of degradation reactions of some dyes and antibiotics over TH-TiO_2.

(Figure 10(a)). TC possesses three of pKa, i.e., pKa1 = 3.3, pKa2 = 7.68, and pKa3 = 9.7 [48].Then, TC is charged positively as pH is less than 3.3 and it is charged negatively as pH is more than 9.7. TC will be charged positively/negatively at pH within 3.3–7.68. The effect of pH on the TC degradation performance is illustrated in Figure 10(b). As can be seen from the figure, the TC degradation efficiency increases with an increase in pH and peaks around pH 4–6 and significantly decreases with further increase in pH. At pH is too low (<3.3) or too high (>7.68), the degradation efficiency was decreased because pulse interaction of the same charge carries. At a range of pH of 3-6, isoelectronic interaction is predominated compared with pulse one.

3.5. Effect of Initial TC Concentrations. In this experiment, the initial TC concentration varied from 30 to 70 mg·L^{-1}, the other experimental conditions remained the same. It was found that when increasing the initial TC concentration from 30 to 70 mg·L^{-1}, decomposition efficiency decreases significantly from 96% to 55% after 120 minutes of visible light illumination (Figure 11(a)). The catalytic reduction performance by TC concentrations can be explained by the fact that the higher initial TC concentration, the more TC molecules adsorbed on the surface of the TH-TiO_2. With a fixed amount of catalyst, excessive TC adsorption causing blockage of active sites on the substrate surface leads to negatively affecting photocatalytic activity. The Langmuir-Hinshelwood model

was employed to analyze the kinetics data in which the linear plot of $\ln(C_t/C_o)$ *vs.t* is constructed. Figure 11(b) presents the Langmuir-Hinshelwood plots at different concentrations. The high determination coefficients, R^2 (0.99–1) confirm that the kinetic degradation reaction of TC over TH-TiO_2 fixed well the Langmuir-Hinshelwood model.

Table 2 presents the rate constants of TC degradation reaction over different catalysts. Although the comparison is lame because the reaction conditions are not the same. However, from Table 1, it can be seen that the rate constant of TH-TiO_2 is relative high compared to previous studies.

3.6. Reusability. Reusability is one of the very important factors when deciding to choose a catalyst for economic and environmental purposes. The used TH-TiO_2 material was washed many times with distilled water and dried at 80°C for 12 hours for regeneration. The TC degradation efficiency over reused catalyst is presented in Figure 12(a). This result shows a slight reduction in TC decomposition efficiency, but after four reuse times, effective TC decomposition still reached over 89.0%. The XRD patterns of TH-TiO_2 (Figure 12(b)) seem slightly changeable indicating TH-TiO_2 possessed excellent structural stability after the regeneration process.

3.7. Catalytic Decomposition of Other Compounds. The photocatalytic activity of TH-TiO_2 was tested for some dyes and antibiotics (Figure 13). It was found that the present TH-TiO_2 could catalyze excellently for dyes (rhodamine-B, methylene blue, and organe red) or antibiotics (ciprofloxacin and chloramphenicol). This offers a potential application of TH-TiO_2 material in the removal of antibiotics in particular and organic pollutants in general from shrimp pond wastewater.

4. Conclusions

The tridoping of S, N, and C into TiO_2 extracted from ilmenite ore by hydrothermal process with thiourea was demonstrated. The S-N-C-tridoped TiO_2 exhibited an excellent catatalytic activity toward the complete minerazation of tetracyline. The possible pathways of tetracyline phototocatalytic degradation over obtained catalyst include hydroxylation, dealkylation, and dehydration via intermediates with smaller molecular mass to final products of CO_2 and water. In addition, the S-N-C-tridoped TiO_2 are potential for photocatalytic degradation of other antibiotics (ciprofloxacin and chloramphenicol) and some dyes (rhodamine-B, methylene blue, and organe red).

Data Availability

The data used to support the findings of this study are available from the corresponding author upon request.

Conflicts of Interest

The authors declare that they have no conflicts of interest.

Acknowledgments

The authors would sincerely like to thank the Team of VLIR-UOS (code ZEIN2016PR431) and the Vietnam Ministry of Education and Training (code B2019-DQN-13) for their financial support.

Supplementary Materials

Figure S1: XRD patterns of TH-TiO2-*a* ($a = 400$, 500, 600, and 700°C). Figure S2: nitrogen adsorption/desorption isotherms of TH-TiO2-*a* ($a = 400$, 500, 600, and 700°C). Figure S3: UV-Vis DRS spectra of TH-TiO2-*a* ($a = 400$, 500, 600, and 700°C) and TiO2. Figure S4: the Kubelka-Munk plots for TH- TH-TiO2-*a* ($a = 400$, 500, 600, and 700°C) and TiO2. Figure S5: the plot of C/C_o *vs.* time for adsorption and photocatalytic reaction or TiO2 và TH-TiO2-*a* ($a = 400$, 500, 600, and 700°C), ($C_o = 30$ mg/L and $m_{catalyst} = 0.6$ gram·L-1); $V = 100$ mL) Figure S6: EDX spectrum and the elements content of TH-TiO2. Figure S7: EDX spectrum and the elements content of TiO2. Figure S8: LC diagram at the retention time of 11.9 min (upper) and its mass spectrum (lower). Figure S9: LC diagram at the retention time of 30 min (upper) and its mass spectrum (lower). Figure S10: LC diagram at the retention time of 16.4 min (upper) and its mass spectra (lower). Table S1: physical chemistry properties of TH-TiO2-*a*. Scheme S1: the proposed fragmentation mechanism of the compound at the retention time of 11.9 min. Scheme S2: the proposed fragmentation mechanism of the compound at the retention time of 30 min. Scheme S3: the proposed fragmentation mechanism of the compound at the retention time of 16.4 min. *(Supplementary Materials)*

References

[1] R. A. Palominos, M. A. Mondaca, A. Giraldo, G. Peñuela, M. Pérez-Moya, and H. D. Mansilla, "Photocatalytic oxidation of the antibiotic tetracycline on TiO_2 and ZnO suspensions," *Catalysis Today*, vol. 144, no. 1-2, pp. 100–105, 2009.

[2] M. Addamo, V. Augugliaro, A. D. Paola et al., "Removal of drugs in aqueous systems by photoassisted degradation," *Journal of Applied Electrochemistry*, vol. 35, no. 7-8, pp. 765–774, 2005.

[3] P. Wang, P. S. Yap, and T. T. Lim, "C-N-S tridoped TiO_2 for photocatalytic degradation of tetracycline under visible-light irradiation," *Applied Catalysis A: General*, vol. 399, no. 1-2, pp. 252–261, 2011.

[4] M. H. Khan, H. Bae, and J. Y. Jung, "Tetracycline degradation by ozonation in the aqueous phase: proposed degradation intermediates and pathway," *Journal of Hazardous Materials*, vol. 181, no. 1-3, pp. 659–665, 2010.

[5] S. Dobaradran, R. Nabizadeh, A. H. Mahvi et al., "Survey on degradation rates of trichloroethylene in aqueous solutions by ultrasound," *Iranian Journal of Environmental Health Science and Engineering*, vol. 7, no. 4, pp. 307–312, 2010.

[6] A. Ž. Gotvajn, M. Bistan, T. Tišler, A. J. Englande, and J. Zagorc-Končan, "The relevance of bisphenol A adsorption during Fenton's oxidation," *International Journal of*

Environmental Science and Technology, vol. 10, no. 6, pp. 1141–1148, 2013.

[7] A. Fujishima, K. Hashimoto, and T. Watanabe, "TiO_2 photocatalysis fundamentals and applications," in *A Revolution in Cleaning Technology*, pp. 14–21, 1999.

[8] P. Periyat, S. C. Pillai, D. E. McCormack, J. Colreavy, and S. J. Hinder, "Improved high-temperature stability and sun-light-driven photocatalytic activity of sulfur-doped anatase TiO_2," *The Journal of Physical Chemistry C*, vol. 112, no. 20, pp. 7644–7652, 2008.

[9] M. S. Wong, S. W. Hsu, K. K. Rao, and C. P. Kumar, "Influence of crystallinity and carbon content on visible light photocatalysis of carbon doped titania thin films," *Journal of Molecular Catalysis A: Chemical*, vol. 279, no. 1, pp. 20–26, 2008.

[10] J. C. Yu, J. Yu, W. Ho, Z. Jiang, and L. Zhang, "Effects of F-doping on the photocatalytic activity and microstructures of nanocrystalline TiO_2Powders," *Chemistry of Materials*, vol. 14, no. 9, pp. 3808–3816, 2002.

[11] I.-C. Kang, Q. Zhang, S. Yin, T. Sato, and F. Saito, "Novel method for preparation of high visible active N-doped TiO_2 photocatalyst with its grinding in solvent," *Applied Catalysis B: Environmental*, vol. 84, no. 3-4, pp. 570–576, 2008.

[12] X. Lin, D. Fu, L. Hao, and Z. Ding, "Synthesis and enhanced visible-light responsive of C,N,S-tridoped TiO_2 hollow spheres," *Journal of Environmental Sciences*, vol. 25, no. 10, pp. 2150–2156, 2013.

[13] M. Zhou and J. Yu, "Preparation and enhanced daylight-induced photocatalytic activity of C,N,S-tridoped titanium dioxide powders," *Journal of Hazardous Materials*, vol. 152, no. 3, pp. 1229–1236, 2008.

[14] Y. Ao, J. Xu, D. Fu, and C. Yuan, "Synthesis of C,N,S-tridoped mesoporous titania with enhanced visible light- induced photocatalytic activity," *Microporous and Mesoporous Materials*, vol. 122, no. 1-3, pp. 1–6, 2009.

[15] Y. Wang, Y. Huang, W. Ho, L. Zhang, Z. Zou, and S. Lee, "Biomolecule-controlled hydrothermal synthesis of C-N-S-tridoped TiO_2 nanocrystalline photocatalysts for NO removal under simulated solar light irradiation," *Journal of Hazardous Materials*, vol. 169, no. 1-3, pp. 77–87, 2009.

[16] Z. Li, Z. Wang, and G. Li, "Preparation of nano-titanium dioxide from ilmenite using sulfuric acid- decomposition by liquid phase method," *Powder Technology*, vol. 287, pp. 256–263, 2016.

[17] N. S. Luong, N. V. Tien, and N. V. Hung, "Research and prepare nanometer-sized titanium dioxide from Ha Tinh inmenite concentrate with sulfuric acid," *Chemistry Journal*, vol. 47, no. 2A, pp. 145–149, 2009.

[18] J. Yu, G. Dai, Q. Xiang, and M. Jaroniec, "Fabrication and enhanced visible-light photocatalytic activity of carbon self-doped TiO2sheets with exposed {001} facets," *Journal of Materials Chemistry*, vol. 21, no. 4, pp. 1049–1057, 2011.

[19] H. R. Pouretedal and M. Kiyani, "Photodegradation of 2-nitrophenol catalyzed by CoO, CoS and CoO/CoS nanoparticles," *Journal of the Iranian Chemical Society*, vol. 11, no. 1, pp. 271–277, 2014.

[20] X. Cheng, X. Yu, and Z. Xing, "Synthesis and characterization of C-N-S-tridoped TiO_2 nano-crystalline photocatalyst and its photocatalytic activity for degradation of rhodamine B," *Journal of Physics and Chemistry of Solids*, vol. 74, no. 5, pp. 684–690, 2013.

[21] T. Ohsaka, F. Izumi, and Y. Fujiki, "Raman spectrum of anatase, TiO2," *Journal of Raman Spectroscopy*, vol. 7, no. 6, pp. 321–324, 1978.

[22] V. Kiran and S. Sampath, "Enhanced Raman spectroscopy of molecules adsorbed on carbon-doped TiO_2 obtained from titanium carbide: a visible-light-assisted renewable substrate," *ACS Applied Materials & Interfaces*, vol. 4, no. 8, pp. 3818–3828, 2012.

[23] X. F. Lei, X. X. Xue, H. Yang et al., "Effect of calcination temperature on the structure and visible-light photocatalytic activities of (N, S and C) co-doped TiO_2 nano-materials," *Applied Surface Science*, vol. 332, pp. 172–180, 2015.

[24] J. Lv, T. Sheng, L. Su et al., "N, S co-doped-TiO_2/fly ash beads composite material and visible light photocatalytic activity," *Applied Surface Science*, vol. 284, pp. 229–234, 2013.

[25] N. Yao, C. Wu, L. Jia et al., "Simple synthesis and characterization of mesoporous (N, S)-codoped TiO_2 with enhanced visible-light photocatalytic activity," *Ceramics International*, vol. 38, no. 2, pp. 1671–1675, 2012.

[26] F. Dong, W. Zhao, and Z. Wu, "Characterization and photocatalytic activities of C, N and S co-doped TiO_2 with 1D nanostructure prepared by the nano-confinement effect," *Nanotechnology*, vol. 19, no. 36, p. 365607, 2008.

[27] G. Zhang, Y. C. Zhang, M. Nadagouda et al., "Visible light-sensitized S, N and C co-doped polymorphic TiO_2 for photocatalytic destruction of microcystin-LR," *Applied Catalysis B: Environmental*, vol. 144, pp. 614–621, 2014.

[28] G. Yang, Z. Yan, and T. Xiao, "Low-temperature solvothermal synthesis of visible-light-responsive S-doped TiO2 nanocrystal," *Applied Surface Science*, vol. 258, no. 8, pp. 4016–4022, 2012.

[29] Q. Xiao and L. Ouyang, "Photocatalytic photodegradation of xanthate over C, N, S-tridoped TiO_2 nanotubes under visible light irradiation," *Journal of Physics and Chemistry of Solids*, vol. 72, no. 1, pp. 39–44, 2011.

[30] X. Wang and T. T. Lim, "Solvothermal synthesis of C-N codoped TiO_2 and photocatalytic evaluation for bisphenol A degradation using a visible-light irradiated LED photoreactor," *Applied Catalysis B: Environmental*, vol. 100, no. 1-2, pp. 355–364, 2010.

[31] H. Wang and Y. Hu, "The photocatalytic property of nitrogen-doped TiO_2 nanoball film," *International Journal of Photoenergy*, vol. 2013, Article ID 179427, 6 pages, 2013.

[32] E. Grabowska, M. Marchelek, T. Klimczuk, G. Trykowski, and A. Zaleska-Medynska, "Noble metal modified TiO_2 microspheres: Surface properties and photocatalytic activity under UV-vis and visible light," *Journal of Molecular Catalysis A: Chemical*, vol. 423, pp. 191–206, 2016.

[33] K. S. W. Sing, "Reporting physisorption data for gas/solid systems with special reference to the determination of surface area and porosity (recommendations 1984)," *Pure and Applied Chemistry*, vol. 57, no. 4, pp. 603–619, 1985.

[34] M. D. Donohue and G. L. Aranovich, "A new classification of isotherms for Gibbs adsorption of gases on solids," *Fluid Phase Equilibria*, vol. 158-160, pp. 557–563, 1999.

[35] P. García-Muñoz, G. Pliego, J. A. Zazo, A. Bahamonde, and J. A. Casas, "Ilmenite ($FeTiO_3$) as low cost catalyst for advanced oxidation processes," *Journal of Environmental Chemical Engineering*, vol. 4, no. 1, pp. 542–548, 2016.

[36] D. Kibanova, M. Trejo, H. Destaillats, and J. Cervini-Silva, "Photocatalytic activity of kaolinite," *Catalysis Communications*, vol. 12, no. 8, pp. 698–702, 2011.

[37] J. M. Herrmann, "Heterogeneous photocatalysis: state of the art and present applications In honor of Pr. R.L. Burwell Jr. (1912–2003), Former Head of Ipatieff Laboratories, Northwestern University, Evanston (Ill)," *Topics in Catalysis*, vol. 34, no. 1-4, pp. 49–65, 2005.

[38] S. Kim and D. S. Aga, "Potential ecological and human health impacts of antibiotics and antibiotic-resistant bacteria from wastewater treatment plants," *Journal of Toxicology and Environmental Health, Part B*, vol. 10, no. 8, pp. 559–573, 2007.

[39] M. A. Behnajady, N. Modirshahla, M. Shokri, and B. Rad, "Enhancement of photocatalytic activity of TiO_2 nanoparticles by silver doping: photodeposition versus liquid impregnation methods," *Global NEST Journal*, vol. 10, no. 1, pp. 1–7, 2008.

[40] R. Liu, H. S. Wu, R. Yeh, C. Y. Lee, and Y. Hung, "Synthesis and bactericidal ability of TiO_2 and Ag-TiO_2 prepared by coprecipitation method," *International Journal of Photoenergy*, vol. 2012, Article ID 640487, 7 pages, 2012.

[41] J. C. Yu, W. Ho, J. Yu, H. Yip, P. K. Wong, and J. Zhao, "Efficient visible-light-induced photocatalytic disinfection on sulfur-doped nanocrystalline titania," *Environmental Science & Technology*, vol. 39, no. 4, pp. 1175–1179, 2005.

[42] A. M. Kamel, H. G. Fouda, P. R. Brown, and B. Munson, "Mass spectral characterization of tetracyclines by electrospray ionization, H/D exchange, and multiple stage mass spectrometry," *Journal of the American Society for Mass Spectrometry*, vol. 13, no. 5, pp. 543–557, 2002.

[43] J. Wang, D. Zhi, H. Zhou, X. He, and D. Zhang, "Evaluating tetracycline degradation pathway and intermediate toxicity during the electrochemical oxidation over a Ti/Ti4O7 anode," *Water Research*, vol. 137, pp. 324–334, 2018.

[44] I. Dalmázio, M. O. Almeida, R. Augusti, and T. M. A. Alves, "Monitoring the degradation of tetracycline by ozone in aqueous medium via atmospheric pressure ionization mass spectrometry," *Journal of the American Society for Mass Spectrometry*, vol. 18, no. 4, pp. 679–687, 2007.

[45] Z. Xie, Y. Feng, F. Wang et al., "Construction of carbon dots modified MoO_3/g-C_3N_4 Z-scheme photocatalyst with enhanced visible-light photocatalytic activity for the degradation of tetracycline," *Applied Catalysis B: Environmental*, vol. 229, pp. 96–104, 2018.

[46] D. Debayle, G. Dessalces, and M. F. Grenier-Loustalot, "Multiresidue analysis of traces of pesticides and antibiotics in honey by HPLC-MS-MS," *Analytical and Bioanalytical Chemistry*, vol. 391, no. 3, pp. 1011–1020, 2008.

[47] Y. Wang, H. Zhang, J. Zhang et al., "Degradation of tetracycline in aqueous media by ozonation in an internal loop- lift reactor," *Journal of Hazardous Materials*, vol. 192, no. 1, pp. 35–43, 2011.

[48] D. He, Y. Sun, L. Xin, and J. Feng, "Aqueous tetracycline degradation by non-thermal plasma combined with nano-TiO2," *Chemical Engineering Journal*, vol. 258, pp. 18–25, 2014.

[49] E. O. Oseghe and A. E. Ofomaja, "Study on light emission diode/carbon modified TiO_2 system for tetracycline hydrochloride degradation," *Journal of Photochemistry and Photobiology A: Chemistry*, vol. 360, pp. 242–248, 2018.

[50] X. Tang, Z. Wang, and Y. Wang, "Visible active N-doped TiO_2/reduced graphene oxide for the degradation of tetracycline hydrochloride," *Chemical Physics Letters*, vol. 691, pp. 408–414, 2018.

[51] X. Cao, J. Tao, X. Xiao, and J. Nan, "Hydrothermal-assisted synthesis of the multi-element-doped TiO_2 micro/nanostructures and their photocatalytic reactivity for the degradation of tetracycline hydrochloride under the visible light irradiation," *Journal of Photochemistry and Photobiology A: Chemistry*, vol. 364, pp. 202–207, 2018.

[52] X. Niu, W. Yan, C. Shao, H. Zhao, and J. Yang, "Hydrothermal synthesis of Mo-C co-doped TiO_2 and coupled with fluorine-doped tin oxide (FTO) for high-efficiency photodegradation of methylene blue and tetracycline: effect of donor-acceptor passivated co-doping," *Applied Surface Science*, vol. 466, pp. 882–892, 2019.

[53] H. R. Pouretedal and B. Afshari, "Preparation and characterization of Zr and Sn doped TiO2nanocomposite and photocatalytic activity in degradation of tetracycline," *Desalination and Water Treatment*, vol. 57, no. 23, pp. 10941–10947, 2016.

[54] X. Hu, Z. Sun, J. Song, G. Zhang, C. Li, and S. Zheng, "Synthesis of novel ternary heterogeneous BiOCl/TiO_2/sepiolite composite with enhanced visible-light-induced photocatalytic activity towards tetracycline," *Journal of Colloid and Interface Science*, vol. 533, pp. 238–250, 2019.